International Journal of Antennas and Propagation

Compact Antennas for Modern Communication Systems

Lead Guest Editor: Massimo Donelli
Guest Editors: Sreedevi Menon and Abhinav Kumar

Compact Antennas for Modern Communication Systems

International Journal of Antennas and Propagation

Compact Antennas for Modern Communication Systems

Lead Guest Editor: Massimo Donelli
Guest Editors: Sreedevi Menon and Abhinav Kumar

Contents

Hindawi
International Journal of Antennas and Propagation
Volume 2020, Article ID 6903268, 2 pages
https://doi.org/10.1155/2020/6903268

Editorial

Compact Antennas for Modern Communication Systems

Massimo Donelli,[1] **Sreedevi Menon**,[2] **and Abhinav Kumar**[3]

[1]*Department of Information Engineering and Computer Science, University of Trento, 38100 Trento, Italy*
[2]*Department of Electronics and Communication Engineering, Amrita Vishwa Vidyapeetham, Amritapuri, India*
[3]*Department of Electrical Engineering, Indian Institute of Technology Hyderabad, Telangana 502285, India*

Correspondence should be addressed to Massimo Donelli; massimo.donelli@unitn.it

Received 9 January 2020; Accepted 9 January 2020; Published 10 February 2020

Modern telecommunication systems such as radio links, radars, and mobile devices require antennas able to operate in different complex environments. In particular, new mobile devices such as smartphones, tablets, IoTs, and wireless sensor networks offer different complex services that require high gain beam-forming and steering capabilities in spite of the limited dimensions of the devices. In particular, in addition to usual voice and other services of standard previous systems, 5G generation devices offer ultrabroadband Internet connection, IP telephony, mobile web access, and other interesting multimedia applications. In such a framework, the design of a suitable radiating system could play a key role in the design of new generations of telecommunication systems. Antennas for these devices must be compact, light, cheap, and able to keep their performance at high levels in any kind of environment. In such a framework, the use of compact and multifunction antennas characterized by adaptive properties is mandatory to dramatically improve the performance of a telecommunication system. Moreover, these kinds of antennas can be used in several fields of practical military as well as civil applications. In particular, radars with these characteristics can be very useful for airport surveillance and security, collision avoidance, ground radar, and monitoring and tracking of unmanned aerial vehicles (UAVs). Concerning military applications, the use of smart antennas can be very useful for missile detection and tracking, antiaircraft defense artillery, and identification friend or foe (IFF) systems. The objective of this special issue was to provide an overview of the current research on smart antennas, the potential to adapt their characteristics to different scenarios, and to highlight the latest developments, innovations, challenges, and opportunities of their application.

This special issue collected five papers concerning compact antennas and their system applications. The first paper proposes uniform triangular arrays (UTAs) to construct multipanel 3D arrays for efficient MIMO transmission and present design examples to be used as next-generation base station antenna arrays. The work presents a specific array structure with different number of panels which can be chosen to be used under different given conditions of the transceiver, such as its location, cell size, and the user distribution [1]. In the second paper, a compact wideband printed antenna with deca-band 4G/5G/WLAN for mobile phone devices has been proposed. In particular, the antenna structure is composed of a monopole antenna and a coupling strip, occupying a small C-shape PCB area of about $27 \times 10.8\ \text{mm}^2$ [2]. The antenna gain improvement has been achieved by using a Fabry–Perot cavity, which is constituted by the ground of the antenna and the PCM. Simulated and measured results show that approximately 46.4% of the operating bandwidth is in the range of 7.5–12 GHz (AR < 3 dB), and the gain of the antenna with MPCM is at least 5 dB higher than the reference antenna. Moreover, the monostatic RCS is reduced from 8 to 20 GHz. In the third paper, a novel slot antenna array based on mirror polarization conversion metasurfaces (MPCM) has been proposed [3]. The proposed antenna achieves circular polarization (CP), effectively reduces the radar cross section (RCS), and increases gain in the entire X-band. This antenna design makes use of the mirrored composition of the polarization conversion metasurfaces (PCM) on the top surface of the

substrate. The MPCM covers a 2×2 slot antenna array that is fed with by means of a sequentially rotating network. The CP radiation is realized by the polarization conversion characteristics of the PCM. The reduction of RCS is achieved by 180° ($\pm 30^{\circ}$) reflection phase difference between two adjacent PCMs, and the improvement in gain, also in this case, has been achieved by using a Fabry–Perot cavity, which is constituted by the ground of the antenna and the PCM. Also, the last two papers propose the MIMO antenna [4, 5]; in particular, in the fourth work, a compact planar multiple-input multiple-output (MIMO) antenna array for the 5G band has been proposed. To improve the isolation of the compact microstrip antenna array elements, an electromagnetic resonant ring method has been considered. The proposed antenna can cover both 3.3–3.6 GHz and 4.8–5 GHz bands proposed for the 5G band, and it consists of two symmetrical meandered monopole radiators, a grid structures, and a Y-shape element. The last paper presents a triple-band monopole antenna with a compact overall size for WLAN/WiMAX particularly suitable for multiple-input and multiple-output (MIMO) applications in the laptop computer. It comprises three monopole radiating elements, along with two rectangular open-ended tuning stubs. The proposed is able to excite 2.4/15.2/5.8 GHz WLAN and 2.3/3.3/5.5 GHz WiMAX bands [5].

Conflicts of Interest

The editors declare that they have no conflicts of interest regarding the publication of this special issue.

Acknowledgments

The guest editorial team would like to express their gratitude to all the authors for their interest in selecting this special issue for their publications.

Massimo Donelli
Sreedevi Menon
Abhinav Kumar

References

[1] M. Yang, Y. Sun, and F. Li, "A compact wideband printed antenna for 4G/5G/WLAN wireless applications," *International Journal of Antennas and Propagation*, vol. 2019, Article ID 3209840, 9 pages, 2019.

[2] J. Yang, W. Ryoo, W. Sung, J.-H. Kim, and J. Park, "3D antenna structures using uniform triangular arrays for efficient full-directional multiuser transmission," *International Journal of Antennas and Propagation*, vol. 2019, Article ID 4150378, 12 pages, 2019.

[3] L. Zhang, C. Liu, C. Ni, M. Kong, and X. Wu, "Low-RCS, circular polarization, and high-gain broadband antenna based on mirror polarization conversion metasurfaces," *International Journal of Antennas and Propagation*, vol. 2019, Article ID 6098483, 8 pages, 2019.

[4] Z. Xu, Q. Zhang, and L. Guo, "A compact 5G decoupling MIMO antenna based on split-ring resonators," *International Journal of Antennas and Propagation*, vol. 2019, Article ID 3782528, 10 pages, 2019.

[5] J. Kulkarni, R. Seenivasan, V. Abhaikumar, and D. R. P. Subburaj, "Design of a novel triple band monopole antenna for WLAN/WiMAX MIMO applications in the laptop computer," *International Journal of Antennas and Propagation*, vol. 2019, Article ID 7508705, 11 pages, 2019.

Hindawi
International Journal of Antennas and Propagation
Volume 2019, Article ID 4150378, 12 pages
https://doi.org/10.1155/2019/4150378

Research Article

3D Antenna Structures Using Uniform Triangular Arrays for Efficient Full-Directional Multiuser Transmission

Jiyeong Yang[1], **Wonjae Ryoo**[1], **Wonjin Sung**[1], **Jeong-Ho Kim**[2] and **Jonghyun Park**[3]

[1]*Department of Electronic Engineering, Sogang University, Seoul 04107, Republic of Korea*
[2]*Department of Electronic and Electrical Engineering, Ewha Womans University, Seoul 03760, Republic of Korea*
[3]*Advanced Standard R&D Lab, LG Electronics, Seoul 07336, Republic of Korea*

Correspondence should be addressed to Wonjin Sung; wsung@sogang.ac.kr

Received 11 February 2019; Accepted 30 September 2019; Published 5 November 2019

Guest Editor: Abhinav Kumar

In order to increase the system capacity of the 5G mobile communication system, multiple-input multiple-output (MIMO) transmission techniques using a large-scale array over the millimeter-wave band have attracted a great amount of attention. To cope with various types of receivers expected in 5G communications such as user equipment (UE) in small cells, indoor Internet-of-Things (IoT) devices at diverse locations, and drones performing aerial navigation, newer types of antenna arrays require all-directional transmission capability. Existing antenna structures with typical panel arrays, however, have restrictions on their transmission angles in both horizontal and vertical directions. In this paper, we propose to employ three-dimensional (3D) array structures composed of multiple triangular panels for efficient massive MIMO transmission of the next-generation wireless systems. We analyze beamforming characteristics of a uniform triangular array (UTA) suitable for such 3D array configurations and present a basic codebook applicable to UTAs. Using antenna structures with multiple UTA panels, multiuser transmission performance is evaluated to demonstrate the effectiveness of the proposal.

1. Introduction

Massive multiple-input multiple-output (MIMO) transmission effectively improves the data rate and the system capacity by increasing the spectral efficiency of 5G mobile communication systems [1–3]. By using the millimeter-wave frequency band, spacing between antenna elements is reduced to make the overall array size smaller, while accurate beamforming can be performed using a large number of antenna elements [4–6]. Codebook-based beam training methods have been proposed for transmission over the millimeter-wave [7], and beam management strategies using such training have been adopted for 5G new radio (NR) [8]. Existing codebook designs in the 3GPP standard are based on uniform linear arrays (ULAs) and uniform rectangular arrays (URAs), which utilize beamforming vectors chosen from the discrete Fourier transform (DFT) matrix [9], including the case for the 16-Tx URA in Release 14 specification [10]. Modifications to the conventional DFT-based codevectors have also been proposed to apply the existing codebooks to uniform circular arrays (UCAs) [11, 12].

Many different forms of transceivers need to be wirelessly connected to support machine-type communications (MTC), Internet-of-Things (IoT) devices, and vehicular-to-everything (V2X) communication for 5G NR. As locations of wireless devices become diversified, antenna arrays capable of transmitting and receiving beams over a wider range of directions are desired. While "full-directional" beamforming techniques to generate and track beams in an isotropic fashion become increasingly important, current antenna arrays have definite limitations to perform such beamforming. Three-dimensional (3D) array structures in different shapes can be utilized to overcome the limitations, with a large number of antenna elements to perform accurate beamforming to target directions. Traditional 3-sector models using ULAs or URAs provide limited beamforming angles in both azimuth and zenith directions. Employing UCAs can overcome the drawback of degraded

performance near sector boundaries by uniformly transmitting signals to all azimuth angles from circularly located antenna elements [13–17]. By vertically stacking the UCAs, a cylinder-type array structure can be constructed to add beam-tilting controllability over a certain range of zenith angles [18]. To expand the range of signal transmission over all azimuth and zenith angles, an array in spherical shape can be used for uniform and stable beamforming to all directions [19]. In an effort to construct antenna arrays capable of transmitting signals over the 3D space, geodesic domes have been used for satellite communications by dividing regular polyhedrons [20–23].

Designing 3D antenna array structures requires practical considerations including beamforming methodology, channel feedback signaling strategy, and hardware implementation complexity. Although full digital beamforming enables accurate and flexible beamforming to target directions, it requires the connection of an RF chain to each antenna element, which is not only costly but also limited by the space constraint of the array. To solve this problem, an array composed of subarrays or panels of antenna elements is desired, for which a plurality of antennas are bundled as a panel to be connected to the same RF chain [24–26]. Therefore, it is necessary to determine the basic panel shape for efficient construction of 3D arrays. While the URA is the most widely used type of antenna panels, building 3D arrays composed of URAs only involves design challenges. An alternative way of 3D array construction is to use antenna subarrays in triangular shape with even spacing between adjacent antenna elements, referred to as the uniform triangular array (UTA). Despite some earlier analyses on the physical patch design for UTAs [27, 28], utilization of triangular arrays for 3D beamforming has not been extensively investigated.

In this paper, we propose to utilize UTAs to construct multipanel 3D arrays for efficient MIMO transmission and present design examples to be used as next-generation base station antenna arrays. A specific array structure with a different number of panels can be chosen to be used under the given conditions of the transceiver, such as its location, cell size, and the user distribution. We first analyze the beam pattern produced by a single UTA and present the basic beamforming vectors applicable to the UTA for beam-tilting purposes. These vectors can be combined for coherent transmission to the target user from multiple panels constituting the whole array. They can also be used for multiuser signal transmission by appropriately allocating a set of UTA panels to each user. The arrays and corresponding beamforming vectors are applied to different transmission environments to demonstrate the usefulness of the proposal. The paper is organized as follows. Section 2 explains signal and system models, followed by the measures used for performance evaluation. In Section 3, beam characteristics of the UTA are analyzed, and beamforming vectors for the single UTA as well as for 3D multipanel arrays are presented. Array structures consisting of multiple UTAs are given in Section 4, and performance evaluation results are shown in Section 5. Conclusions are given in Section 6.

2. System Model

The UTA in consideration has the form of the equilateral triangle with constant spacing between the adjacent antenna elements in it. A UTA with 15 antenna elements is shown in Figure 1(a), where the number of elements in 5 antenna rows is 1, 2, 3, 4, and 5, respectively. Generalising this type of antenna placement, the l-th antenna row of the panel includes l antenna elements. For the triangular panel with L antenna rows, the number of antennas in the UTA is $N = L\ (L+1)/2$. If the entire antenna array structure is composed of M UTA panels, the number of total antenna elements becomes $M_T = MN$. To compare the beam patterns, we consider the conventional rectangular array with a similar number of antennas, which is the URA with 16 antenna elements, as shown in Figure 1(b). Parameters α and β shown in Figure 1 represent the horizontal and vertical angles used for visualisation of beam patterns.

An example of the 3D antenna structure and related coordinate parameters are shown in Figure 2, where 20 UTA panels constitute the icosahedron-based antenna array. The centre of the 3D array is called origin and denoted by O. The target user equipment (UE) is denoted by U. Symbol $A_{m,n}$ denotes the location of the n-th antenna element in the m-th UTA panel. The direction of the UE can be represented in polar coordinates using the azimuth angle Φ and zenith angle Θ. Also, the direction of $A_{m,n}$ from the origin is represented by the azimuth angle $\phi_{m,n}$ and zenith angle $\theta_{m,n}$. Denoting the distance from the origin to $A_{m,n}$ by $r_{m,n}$, the location vector for the n-th antenna element in the m-th panel is expressed as

$$A_{m,n} = \left(r_{m,n}\cos\phi_{m,n}\sin\theta_{m,n},\ r_{m,n}\sin\phi_{m,n}\sin\theta_{m,n},\ r_{m,n}\cos\theta_{m,n}\right), \tag{1}$$

similarly, the UE location vector can be written as $U = (\rho\cos\Phi\sin\Theta,\ \rho\sin\Phi\sin\Theta,\ \rho\cos\Theta)$, where ρ is the distance from the origin to the UE.

The signal transmitted from the antenna array with M panels and received by the k-th UE can be written as

$$\mathbf{y}_k = \sum_{m=1}^{M} \mathbf{H}_{k,m}\mathbf{w}_{k,m}s_k + \mathbf{I}_k + \mathbf{n}_k, \tag{2}$$

where $\mathbf{y}_k$ is the received vector, $\mathbf{H}_{k,m}$ is the channel matrix for the m-th panel, $\mathbf{w}_{k,m}$ is the beamforming vector for the m-th panel, and s_k is the data symbol. Intercell interference and complex Gaussian noise vectors are denoted by $\mathbf{I}_k$ and $\mathbf{n}_k$, respectively. The signal model can be extended to the case when beams are formed to multiple target UEs as

$$\begin{aligned}\mathbf{y}_k &= \sum_{m=1}^{M} \mathbf{H}_{k,m}\mathbf{W}_m\mathbf{s} + \mathbf{I}_k + \mathbf{n}_k \\ &= \sum_{m=1}^{M} \mathbf{H}_{k,m}\mathbf{w}_{k,m}s_k + \sum_{u\neq k}\sum_{m=1}^{M} \mathbf{H}_{k,m}\mathbf{w}_{u,m}\mathbf{s}_u + \mathbf{I}_k + \mathbf{n}_k,\end{aligned} \tag{3}$$

where $\mathbf{y}_k$ is again the received vector for the k-th UE and $\mathbf{s} = [s_1, s_2, \ldots, s_K]^T$ is the data vector for K UEs serviced by

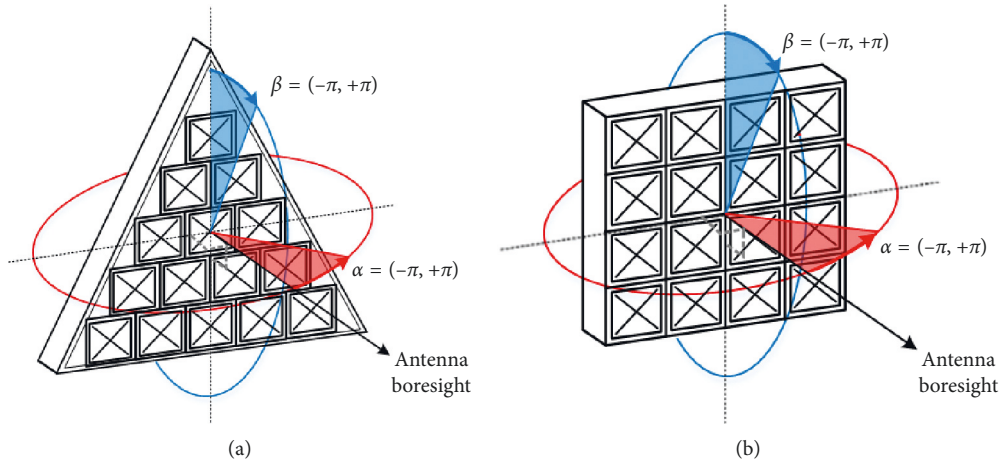

Figure 1: Comparison of antenna arrays. (a) UTA and (b) URA.

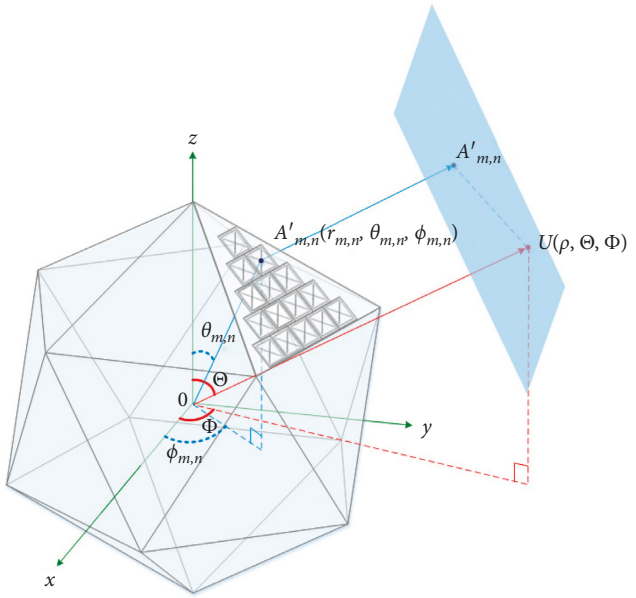

Figure 2: 3D antenna structure composed of UTA panels and coordinate information.

the transmit antenna array. Beamforming matrix $\mathbf{W}_m = [\mathbf{w}_{1,m}, \mathbf{w}_{2,m}, \ldots, \mathbf{w}_{K,m}]$ includes the beamforming vectors for K UEs.

When multiuser data are simultaneously transmitted, the beams intended for the other UEs act as the interference and the corresponding interference signal is represented by the second term in equation (3). Combining the effect of interuser interference, intercell interference, and the noise, the signal-to-interference-plus-noise-ratio (SINR) for the k-th UE becomes

$$\Gamma_k = \frac{\left|\sum_{m=1}^{M} \mathbf{H}_{k,m}\mathbf{w}_{k,m}\right|^2}{\left|\sum_{u\neq k}\sum_{m=1}^{M} \mathbf{H}_{k,m}\mathbf{w}_{u,m}\right|^2 + \left|\mathbf{I}_k\right|^2 + N_0}, \quad (4)$$

where N_0 is the noise power. Summing up the individual data rate $R_k = \log_2(1 + \Gamma_k)$ for K UEs, the sum rate of the system is represented by

$$R = \sum_{k=1}^{K} \log_2(1 + \Gamma_k). \quad (5)$$

The antenna gain pattern applied to each antenna element follows the 3GPP standard model in [29] given as

$$G(\varphi_v, \varphi_h) = -\min\{-[G_v(\varphi_v) + G_h(\varphi_h)], 30\}\,[\text{dB}], \quad (6)$$

where $G_v(\varphi_v) = -\min\left\{(\varphi_v/65^\circ)^2, 30\right\}$ is the vertical gain and $G_h(\varphi_h) = -\min\left\{(\varphi_h/65^\circ)^2, 30\right\}$ is the horizontal gain. Arguments φ_v and φ_h represent the vertical and horizontal deviation angles from the antenna boresight, respectively.

3. Uniform Triangular Array

We generate the beam pattern of the UTA using the array shown in Figure 1(a). We assume no phase shifting is applied to the antenna elements and the beam direction is identical to the boresight of the array. The beam pattern is obtained by calculating the signal power at different values of the horizontal and vertical angles. Figure 3(a) indicates the horizontal beam pattern obtained by changing α for given values of β. Also, Figure 3(b) indicates the vertical beam pattern obtained by changing β for given values of α. For comparison, similar beam patterns are evaluated for the URA using the array shown in Figure 1(b), and the results are plotted in Figure 4. Note that the horizontal and vertical patterns for the URA are of the same shape due to the symmetry of the array. Although the patterns for the UTA and URA are not identical, general beam shapes including the 3 dB beamwidth and the magnitudes of sidelobes are similar.

The beam patterns when the target beam direction deviates from the array boresight are also compared for the two arrays. Figure 5(a) shows the peak power observed at the target direction when the beam direction deviation angle θ increases from 0, assuming the unit power is transmitted from each antenna element. The peak power tends to decrease as θ becomes large due to the decreasing gain of unit antennas described in equation (6). However, very similar peak power values are observed for the two arrays for all

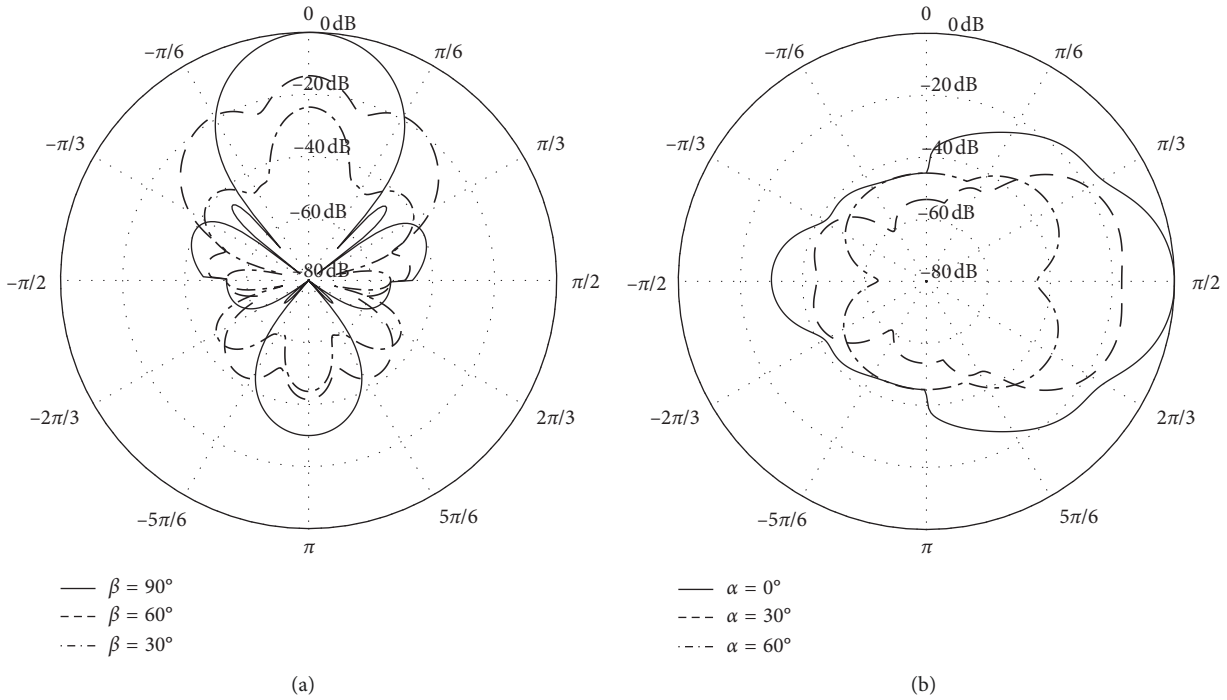

Figure 3: UTA beam pattern. (a) Horizontal pattern: $-\pi \le \alpha \le \pi$; (b) vertical pattern: $-\pi \le \beta \le \pi$.

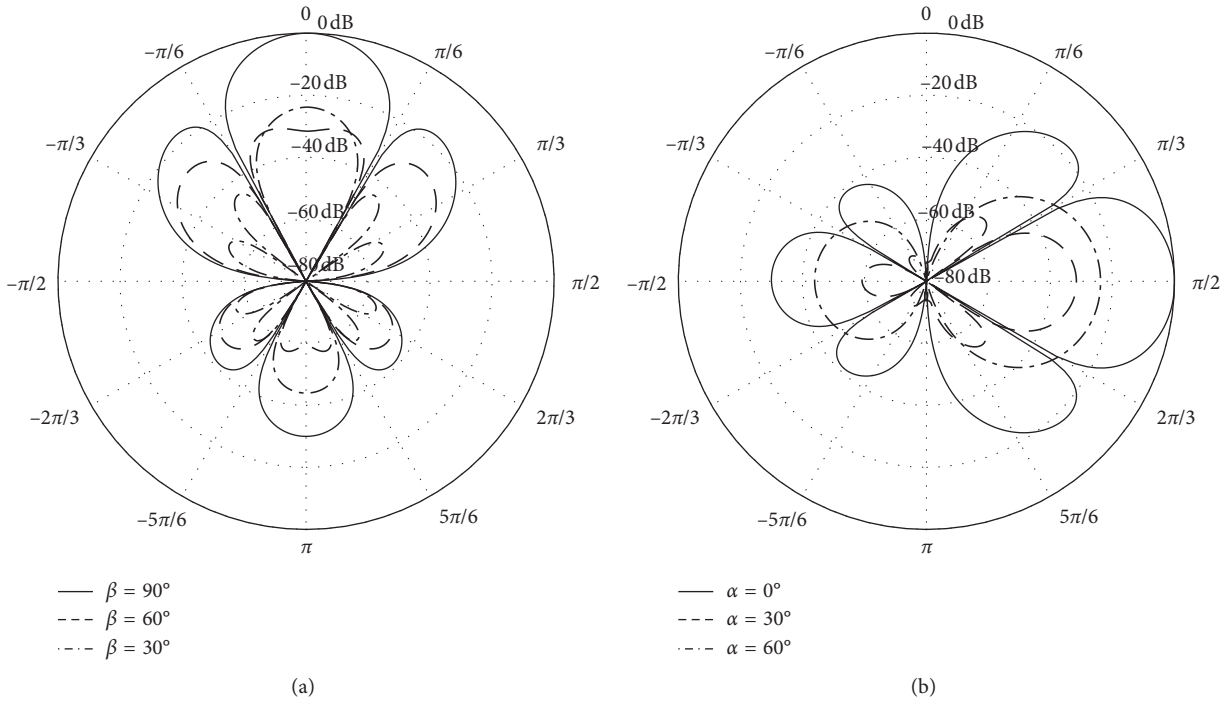

Figure 4: URA beam pattern. (a) Horizontal pattern: $-\pi \le \alpha \le \pi$; (b) vertical pattern: $-\pi \le \beta \le \pi$.

ranges of the deviation angle. The slight difference of the power values corresponds to 16/15, the ratio of antenna numbers. Figure 5(b) is the evaluation result for the 3 dB beamwidth for different values of θ, showing the beamwidth remains relatively constant for all deviation angles.

Despite some detailed differences in their beam patterns, we observe from the comparison results that general beam characteristics for the two arrays are similar. Key features such as the beam peak power and the beamwidth do not depend on the type of the array, but on the number of elements in the array. Thus, the UTA with an appropriate number of elements can be an attractive alternate candidate of the URA to construct 3D antenna structures with expected beamforming characteristics.

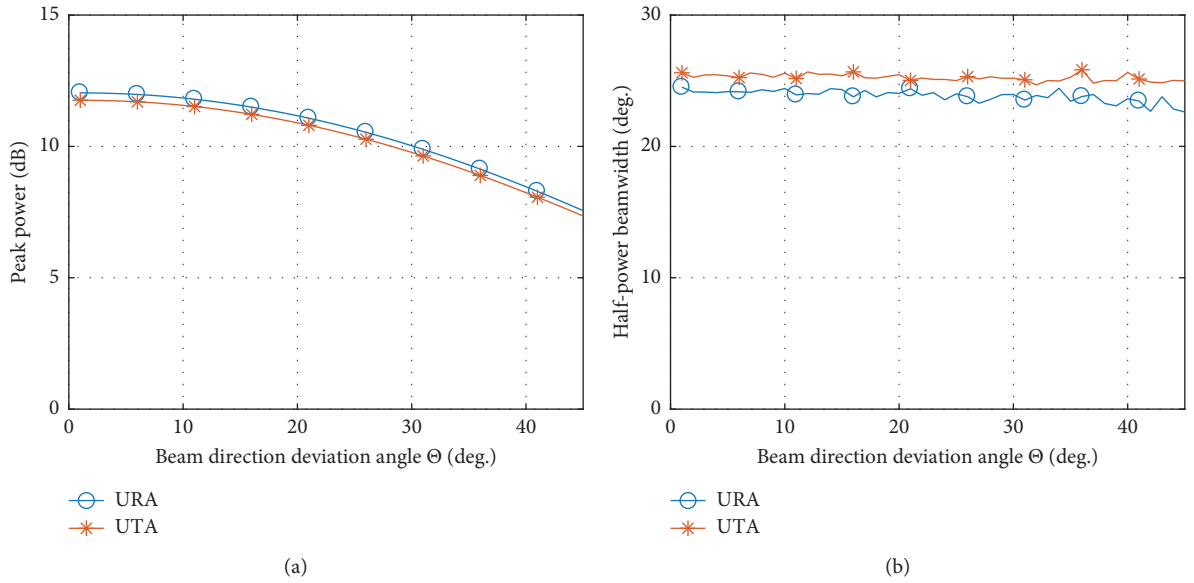

Figure 5: Beam pattern comparison. (a) Peak power and (b) half-power beamwidth.

We determine the set of beamforming vectors using the geometry of the antenna locations, which can be used for tilting transmitted beams from the UTA of an arbitrary size. Similar to the codevector generation for conventional two-dimensional arrays, the determination of the beamforming vectors can be obtained by the Kronecker product of horizontal and vertical beams. Figure 6 shows the location indices for the antenna elements of the UTA. The antenna elements of the UTA exist in the subset of all possible locations within the rectangle produced by L antenna rows and $2L-1$ antenna columns. Let us first define the basic beamforming vectors for vertical beam generation. A vertical beamforming vector of length L takes the form of the discrete Fourier transform (DFT) vector and is represented as

$$\mathbf{a}_p = \left[1 \;\; e^{j2\pi p/P} \;\; e^{j2\pi 2p/P} \;\; \cdots \;\; e^{j2\pi(L-1)p/P}\right]^T \quad \text{for } p = 0, 1, \ldots, P-1, \tag{7}$$

with linearly increasing amount of phase values. Beam index p determines one of the total P angles for vertical beam tilting, and the $L \times P$ matrix

$$\mathbf{A} = \left[\mathbf{a}_0 \;\; \mathbf{a}_1 \;\; \cdots \;\; \mathbf{a}_{P-1}\right], \tag{8}$$

represents the set of P vertical beamforming vectors. Second, the basic beamforming vectors for horizontal beam generation can be denoted by the vector of length $2L-1$ as

$$\mathbf{b}_q = \left[e^{-j2\pi(L-1)q/Q} \;\; \cdots \;\; e^{-j2\pi q/Q} \;\; 1 \;\; e^{j2\pi q/Q} \;\; \cdots \;\; e^{j2\pi(L-1)q/Q}\right]^T \quad \text{for } q = 0, 1, \ldots, Q-1, \tag{9}$$

which has a modified form of the DFT vector with the zero phase element in the centre of the vector. A horizontal beam is generated in one Q tilting angle according to index q. By including all Q beamforming vectors as columns of the $(2L-1) \times Q$ matrix, we obtain

$$\mathbf{B} = \left[\mathbf{b}_0 \;\; \mathbf{b}_1 \;\; \cdots \;\; \mathbf{b}_{Q-1}\right]. \tag{10}$$

To combine the vertical and horizontal beams, we multiply column vector $\mathbf{a}_p$ and row vector $\mathbf{b}_q^T$ to produce $L \times (2L-1)$ codevector matrix in equation (11)

$$\mathbf{C}_{p,q} = \mathbf{a}_p \mathbf{b}_q^T = \begin{bmatrix} e^{-j2\pi(L-1)q/Q} & & e^{-j2\pi q/Q} & 1 & e^{j2\pi q/Q} & & e^{j2\pi(L-1)q/Q} \\ e^{j2\pi p/P} e^{-j2\pi(L-1)q/Q} & & e^{j2\pi p/P} e^{-j2\pi q/Q} & e^{j2\pi p/P} & e^{j2\pi p/P} e^{j2\pi q/Q} & & e^{j2\pi p/P} e^{j2\pi(L-1)q/Q} \\ e^{j2\pi 2p/P} e^{-j2\pi(L-1)q/Q} & \cdots & e^{j2\pi 2p/P} e^{-j2\pi q/Q} & e^{j2\pi 2p/P} & e^{j2\pi 2p/P} e^{j2\pi q/Q} & \cdots & e^{j2\pi 2p/P} e^{j2\pi(L-1)q/Q} \\ \vdots & & \vdots & \vdots & \vdots & & \vdots \\ e^{j2\pi(L-1)p/P} e^{-j2\pi(L-1)q/Q} & & e^{j2\pi(L-1)p/P} e^{-j2\pi q/Q} & e^{j2\pi(L-1)p/P} & e^{j2\pi(L-1)p/P} e^{j2\pi q/Q} & & e^{j2\pi(L-1)p/P} e^{j2\pi(L-1)q/Q} \end{bmatrix}, \tag{11}$$

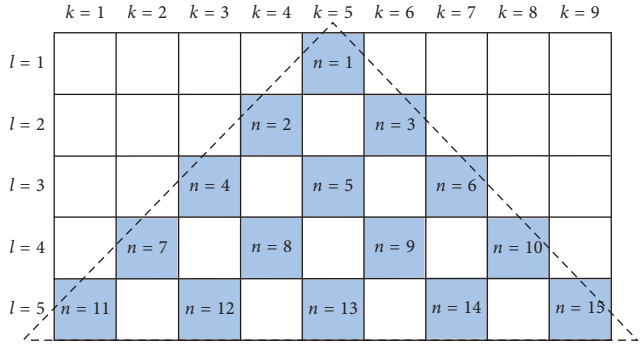

Figure 6: Antenna element indices for the UTA with L rows and $2L-1$ columns ($L=5$).

for $p = 0, 1, \ldots, P-1$ and $q = 0, 1, \ldots, Q-1$. Note that $\mathbf{C}_{p,q}$ includes phase shifting terms for all elements in the rectangular area as shown in Figure 6. Beamforming vectors for the UTA are obtained by selecting the elements in equation (11) which correspond to the shaded elements of the triangular region in Figure 6, which are the UTA antenna elements. To choose N elements out of all L $(2L-1)$ elements in $\mathbf{C}_{p,q}$, we denote the n-th element of the beamforming vector for the UTA by $c_{p,q}^{n}$. This element is obtained by choosing $\mathbf{C}_{p,q}^{(l,k)}$, which is the l-th row and k-th column element in $\mathbf{C}_{p,q}$; i.e., we have the relation $c_{p,q}^{n} = \mathbf{C}_{p,q}^{(l,k)}$. We need to specify how the codevector element index n is related to matrix indices l and k, and the relation is given by the following formulas

$$l = x \quad \text{if } \frac{x(x-1)}{2} < n \le x\frac{(x+1)}{2},$$
$$k = L - l^2 + 2n - 1. \tag{12}$$

Using these formulas, the codevector element index $n = 1, 2, \ldots, N-1$ is translated to the row index l and column index k and then the corresponding elements in equation (11) can be chosen. The codevector for the UTA is obtained by collecting selected elements $c_{p,q}^{n}$ as

$$\mathbf{c}_{p,q} = \left[c_{p,q}^{1} \;\; c_{p,q}^{2} \;\; \cdots \;\; c_{p,q}^{N}\right]^{T}. \tag{13}$$

Since there are P vertical beam directions and Q horizontal beam directions, the total of PQ codevectors of length N can be constructed by combining the beams in both directions. Thus, we include all these codevectors to form the codebook for the UTA as the $N \times (PQ)$ matrix

$$\mathbf{C} = [\,\mathbf{c}_{1,1} \;\; \mathbf{c}_{1,2} \;\; \cdots \;\; \mathbf{c}_{1,Q} \;\; \mathbf{c}_{2,1} \;\; \mathbf{c}_{2,2} \;\; \cdots \;\; \mathbf{c}_{2,Q} \;\; \cdots \;\; \mathbf{c}_{P,1} \;\; \mathbf{c}_{P,2} \;\; \cdots \;\; \mathbf{c}_{P,Q}\,]. \tag{14}$$

Beamforming vectors can be determined by choosing the column in equation (14) with the desired vertical beam index p and horizontal beam index q.

To apply the beamforming vectors described above for coherent data transmission using multipanel arrays, an appropriate adjustment is required. Each UTA panel differs in its position and antenna boresight, and the correction parameter $\varphi_{k,m}$ needs to be multiplied to the chosen codevector to compensate for this difference as

$$\mathbf{w}_{k,m} = \varphi_{k,m}\mathbf{c}_{p,q}, \tag{15}$$

to form the beamforming vector for the m-th panel and the k-th UE. To obtain the correction parameter, the distance from the reference point of each panel to the UE needs to be calculated. Without loss of generality, we let the location of the first element be the reference point for each UTA panel. The relative distance from $A_{m,1}$ to the UE can be determined by taking the inner product of unit vector $\mathbf{u} = \overrightarrow{\mathrm{OU}}/|\overrightarrow{\mathrm{OU}}|$ from the origin to the UE and vector $\overrightarrow{\mathrm{OA}_m}$ in the direction of the reference point from the origin, i.e., $d_m = \mathbf{u} \cdot \overrightarrow{\mathrm{OA}_{m,1}}$. The result of calculation using polar coordinates is given by [30]

$$d_m = \mathbf{u} \cdot \overrightarrow{\mathrm{OA}_{m,1}} = -r_{m,1}\big(\sin\Theta \sin\theta_{m,1} \cos\big(\Phi - \phi_{m,1}\big) + \cos\Theta\cos\theta_{m,1}\big), \tag{16}$$

where $r_{m,1}$ is the distance between the origin and the reference antenna location. Using this information, the channel phase difference for the reference antenna element in each panel can be obtained as

$$\angle\varphi_{k,m} = \frac{2\pi f_c d_m}{c} = -2\pi r_{m,1}\frac{\big(\sin\Theta\sin\theta_{m,1}\cos\big(\Phi - \phi_{m,1}\big) + \cos\Theta\cos\theta_{m,1}\big)}{\lambda}, \tag{17}$$

where f_c is the carrier frequency, c is the propagation speed, and λ is the wavelength. The correction parameter in equation (15) is determined by exponentiating the negative value of equation (17) to compensate for the phase difference as

$$\varphi_{k,m} = e^{-j\angle\varphi_{k,m}}. \tag{18}$$

We can obtain the correction parameter for each panel by using the coordinate information of the reference antenna and the target UE from equation (18) and apply it to transmit beams from the given multipanel array structure.

4. Multipanel UTAs

Multiple UTAs can be combined together to construct 3D arrays of various shapes. All UTAs are of the same equilateral triangular shape, and they can be used as the basic building blocks for more complex and versatile antenna structures. For example, the UTAs can be put together to form a multifaceted pyramid which can be either wall-mounted or attached to the ceiling. As more small cells are being deployed for 5G NR, such ceiling type of antenna arrays fit well for indoor small cell applications. Figure 7 is an illustrative example of using multiple UTAs to form the pyramid shaped 3D array, mounted to the indoor ceiling for efficient signal transmission to the receivers within the cell. Parameters Θ_1, Θ_2, etc. are the beam deviation angles from their respective panel boresight. The signal to the target UE can

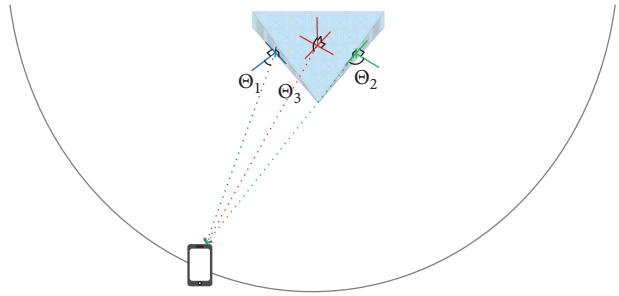

Figure 7: Antenna array for indoor small cell transmission.

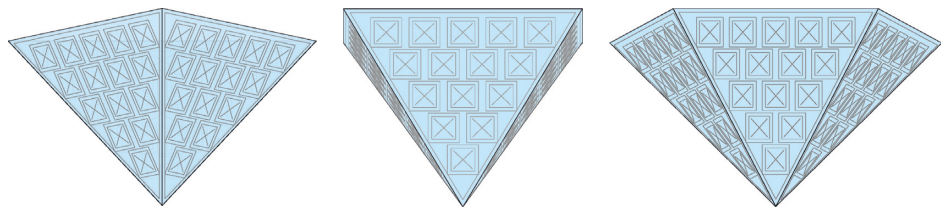

Figure 8: Ceiling-type 3D antenna arrays. (a) $M = 3$; (b) $M = 4$; (c) $M = 5$.

be transmitted from the panel with the smallest deviation angle only or from multiple panels using the beam vectors for coherent signal combining. Adding more UTA panels results in 3D array structures in different shapes. Figure 8 shows ceiling-type arrays for the number of panels $M = 3$, 4, and 5. For these arrays, the angle between the boresight of the UTA panels and the direction perpendicular to the ceiling surface is 70.5°, 54.7°, and 37.4°, respectively. When the number of panels increases to $M = 6$, the array lies flat to the ceiling surface and the panel boresight is the direct downward direction. Depending on the room geometry and the typical UE distribution, a particular type of 3D array can be chosen for enhanced transmission performance.

The ceiling-type arrays introduced in Figure 8 have the limitation of covering only one hemisphere of the entire 3D space. To overcome this limitation, we can construct array structures based on regular polyhedrons and their variations to include more UTA panels covering the whole space. Figure 9 shows such array structures using $M = 8$, 20, 60, and 80 panels. The first two arrays in Figures 9(a) and 9(b) are constructed by attaching a UTA panel to each face of the octahedron and icosahedron, respectively. Dodecahedron with 12 faces cannot be directly used to construct an array with UTAs since its faces are pentagons. Instead, we apply 5 UTAs to cover each face of the dodecahedron as shown in Figure 9(c) and obtain the 3D structure with 60 UTA panels. Also, each triangular face of the icosahedron can be further divided to include four equilateral triangles in a smaller size, providing the installation space for 80 UTA panels as illustrated in Figure 9(d). The total number of antenna elements is determined as $M_T = MN$, where N is the number of antennas in each panel. Using $N = 15$ elements for the UTA, the number of total antennas in the array structure with $M = 60$ panels amounts to $M_T = 900$. Hence, massive arrays in various shapes and sizes can be built by multiple UTAs by changing the design parameters. As the demand for 3D antenna arrays increases, the mass production of UTAs provided at a reduced cost can be used for the array construction.

5. Performance Evaluation

We evaluate the performance of the 3D arrays for several different transmission scenarios. Here, we are interested in judging the applicability of the candidate arrays to the UEs in the 3D space when the direct line-of-sight (LoS) beam is the dominating component of transmission. Thus, only the normalized received power of the LoS beam is measured based on the deviation angle from each panel to the UE, ignoring the effects of the path loss or the multipath signals. The normalized received power has the unit value when an antenna element is directly pointed to the target UE with the zero deviation angle. For the UTA with M elements, the received signal is combined to exhibit the normalized received power of $10\log_{10} M$ dB for the UE with the zero deviation angle. The received power decreases as the deviation angle becomes larger, and the exact amount of the decrease is determined by the gain pattern described in equation (6). When M panels are collaboratively transmitting the beam to the UE in a given location, we measure the deviation angle of all panels and arrange them in ascending order as $\Theta_1 < \Theta_2 < \cdots < \Theta_M$. The corresponding normalized received power can be then listed in descending order $P_1 > P_2 > \cdots > P_M$. The subscript index k in variables Θ_k and P_k indicates the order of contribution for the respective panel. For example, $k = 2$ suggests that Θ_2 is the second smallest deviation angle among all panels,

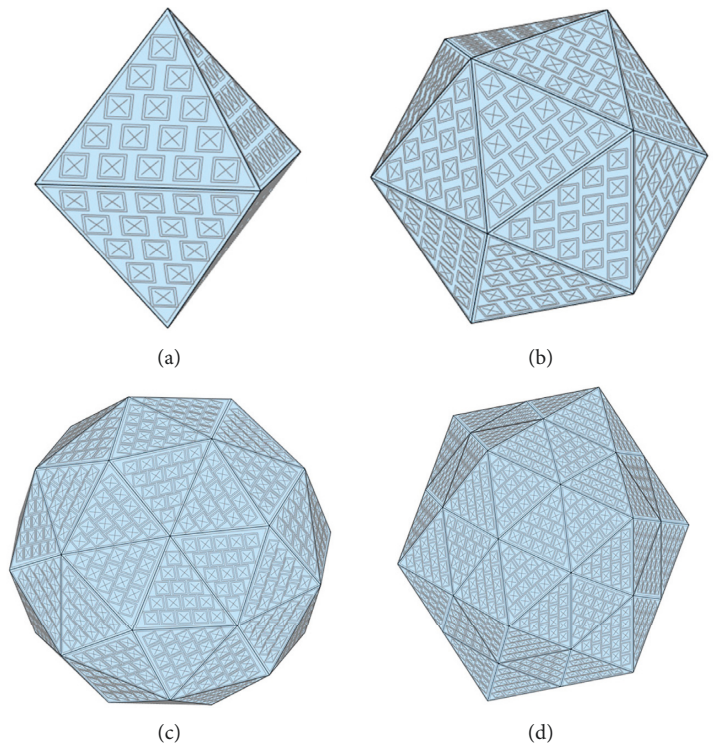

Figure 9: Polyhedron-type 3D antenna arrays. (a) $M = 8$; (b) $M = 20$; (c) $M = 60$; (d) $M = 80$.

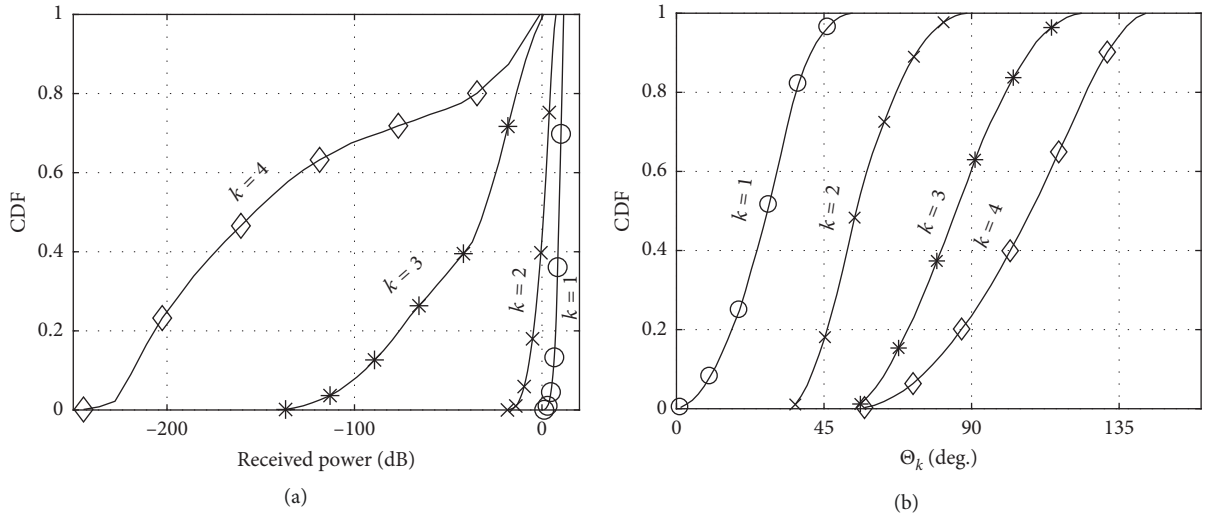

Figure 10: Transmission characteristics for the ceiling-type 3D array using $M = 4$ UTAs. (a) Received power and (b) deviation angle.

providing the second largest normalized received power P_2 to the UE.

Figure 10 shows the transmission characteristics of the ceiling-type 3D array described in Figure 7 with $M = 4$ panels, to the UE which is assumed to be located uniformly over the hemisphere. In Figure 10(a), the cumulative distribution function (CDF) of the normalized received power is shown for beams from four panels. The distribution of the largest received power P_1 is indicated by $k = 1$ in the figure, with the average value of 8.9 dB. The average values of P_2, P_3, and P_4 are respectively 0.3, −15.1, and −16.6 dB, suggesting the amount of received power rapidly decreases for panels with larger deviation angles. For $k > 2$, the amount of power contribution is significantly smaller than the first two panels. Therefore, using up to two panels for collaborative transmission seems to suffice in this scenario. Figure 10(b) shows the CDF of Θ_k, indicating larger deviation angle distributions as k increases. The average values of Θ_k are 28.1, 57.5, 87.0, and 107.8° for $k = 1$, 2, 3, and 4. The average values for Θ_3 and Θ_4 far exceed the 3 dB beamwidth of the gain pattern in equation (6), providing a negligible power contribution to the target UE.

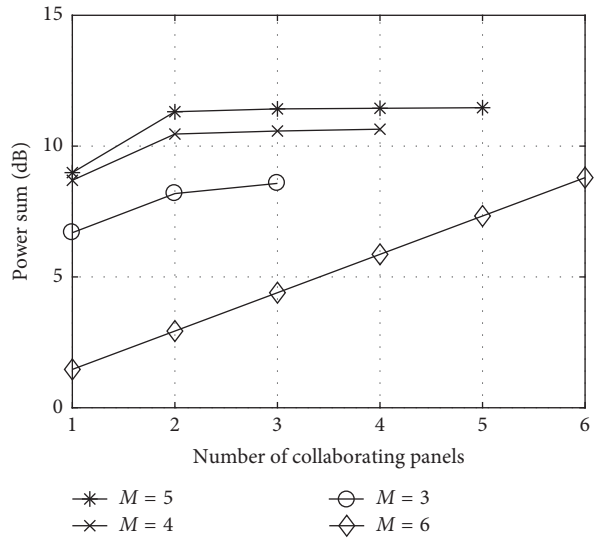

Figure 11: Received power versus the number of collaborating panels for the ceiling-type 3D arrays.

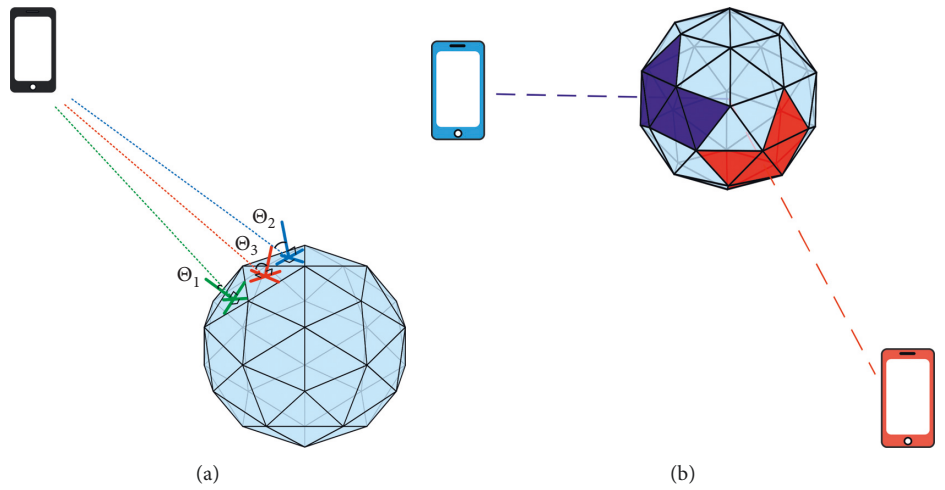

Figure 12: Transmission using the 3D array. (a) Single-user transmission and (b) multiuser transmission.

We apply the ceiling-type arrays with $M = 3$, 4, 5, and 6 UTA panels to determine the sum of normalized received power for the UE in a random location over the hemisphere. In Figure 11, the power sum is shown for the increasing number of collaborating panels M' performing coherent signal combining. It can be observed in the figure that the power becomes saturated for $M' = 2$, and using more panels does not provide additional power gain. Only exception to this is the array with $M = 6$ UTA panels, for which all panel surfaces lie flat to the same surface. In this case, the deviation angle for all panels to the UE is identical and the received power increases linearly as M' increases. It is also observed from the figure that the array with $M = 5$ UTA panels provides the largest normalized power, suggesting its structural advantage of efficiently covering the space in terms of the panel boresight to random UEs.

Next, the normalized received power using the polyhedron-based 3D array with $M = 60$ panels shown in Figure 9(c) is considered. For this case, we assume beamforming is performed to random UEs located over the spherical model with the array in the centre, covering the whole space. We first evaluate the normalized received power for the single-user transmission scenario depicted in Figure 12(a), and then extend the result to examine the sum rate for the multiuser transmission scenario indicated in Figure 12(b).

Figure 13 shows the CDFs for the normalized received power and the deviation angle. Although as many as 60 panels can be collaboratively used for the single-user transmission, up to approximately 5 panels contribute to the most of the received power. In Figure 13(a), the power distribution is plotted for $k = 1$ to 5, for which the average values are 11.3, 10.9, 10.0, 9.4, and 8.7 dB in descending order. Unlike the ceiling-type arrays, the power decrease is less severe for increasing values of k. This can also be observed in the distribution of the deviation angles shown in

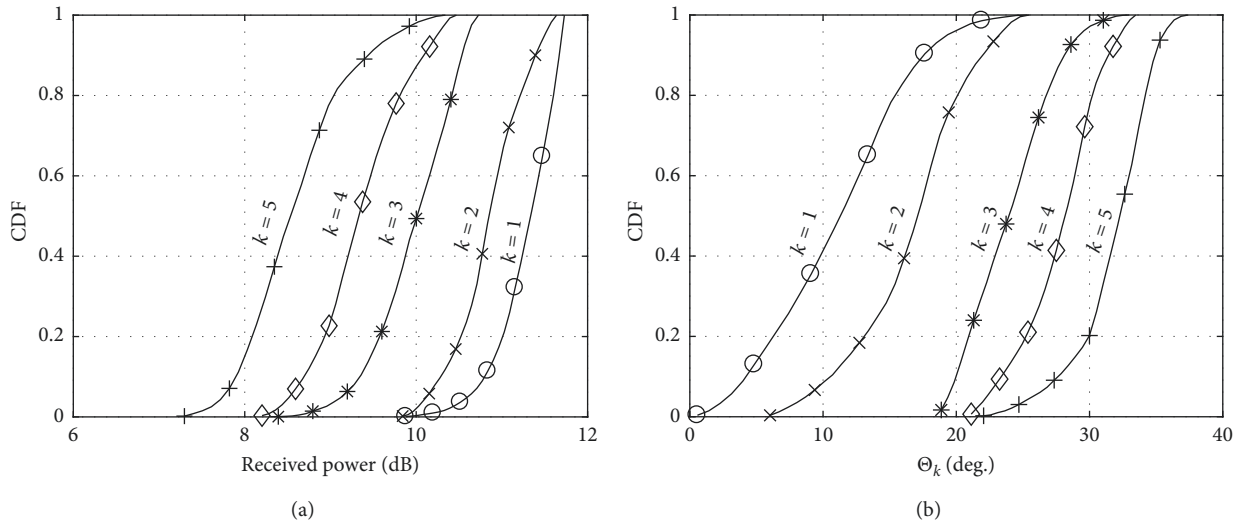

Figure 13: Transmission characteristics for the polyhedron-type 3D array using $M = 60$ UTAs. (a) Received power; (b) deviation angle.

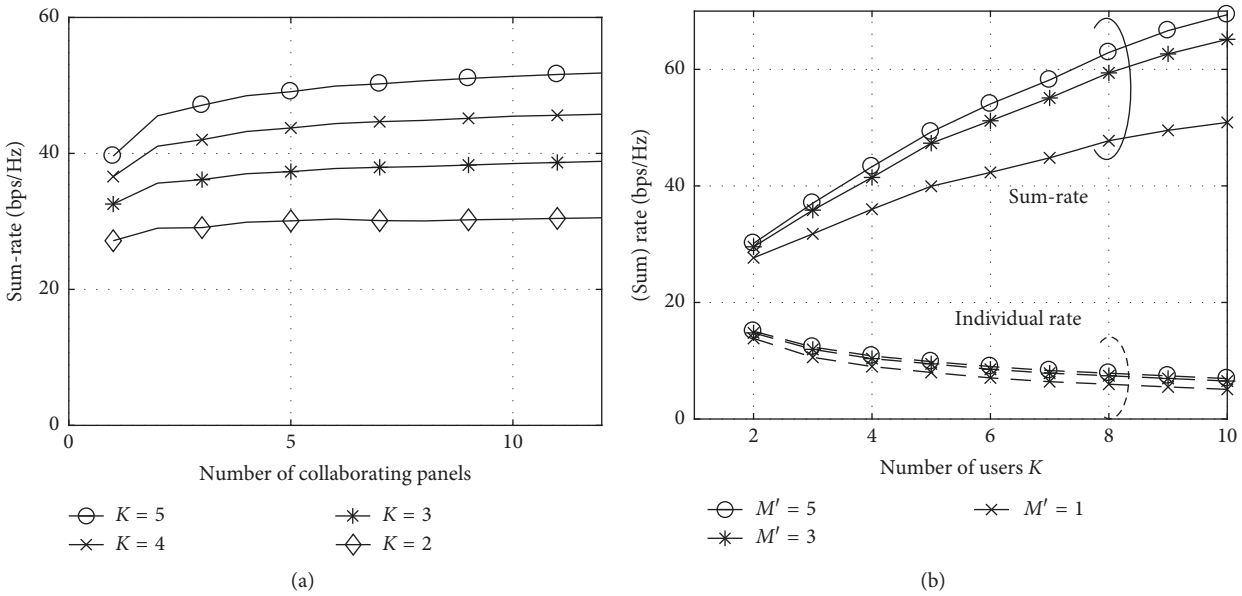

Figure 14: Performance of multiuser transmission for the polyhedron-type 3D array using $M = 60$ UTAs. (a) Sum rate vs. number of collaborating panels; (b) rate vs. number of users.

Figure 13(b), with the average vales of 11.5, 16.9, 24.2, 28.0, and 32.0°. For the spherical-shaped array with a large number of panels, more panels with reasonably small deviation from the boresight contribute in transmitting signals to the target UE.

The array provides the beam transmission capability to all isotropic UE locations in the 3D space, and only the limited number of panels is sufficient for beamforming to a single user. Therefore, multiuser transmission to geometrically separated UEs is desired for enhanced utilization of the array resource to increase the system throughput. We randomly locate K UEs over the space and assign a set of panels for beamforming to a given UE. Figure 10(b) is an illustration of multiuser transmission to $K = 2$ UEs, where the panels assigned for the UE in the left are indicated in blue colour and the panels for the UE in the downward direction are marked in red. The panel allocation strategy is to assign panels to UEs in a round-robin fashion, with the panel having the boresight closest to the direction of the UE assigned in turns. If the panel with such a condition is already assigned to some other UE, the panel with the next smallest deviation angle is assigned. The procedure continues until all UEs are assigned with M' panels for their data transmission, where M' is the predetermined number of panels used for collaborative beamforming to each user.

We apply this panel allocation process to K multiple UEs using the polyhedron-based array with 60 UTA panels to evaluate the sum-rate performance. The sum rate is determined by adding the individual rate of the UEs as

described in equation (5). The individual rate is obtained by the capacity formula, where the signal-to-interference ratio is computed by the received power from the panels assigned to the UE and the interference power from the panels for the other UEs. In Figure 14(a), the sum rate is evaluated from repeated simulations of randomly located UEs when the number of simultaneously present UEs for beam transmission is $K = 2$, 3, 4, and 5. An increasing value of the sum rate is shown as K becomes large, showing the multiuser transmission capability of the array. It is shown in the figure that the saturation does not occur until $M' = 10$ collaborating panels, suggesting 10 or more panels can be assigned for each UE. However, the additional gain after using $M' = 5$ panels becomes limited, and using more panels will incur increased operation complexity and power consumption. In Figure 14(b), we evaluate the rates when the number of UEs increases, while using 5 or less panels for each UE. Although the individual rate tends to exhibit a slow decrease for more UEs, the sum rate keeps increasing up to 10 UEs, confirming the applicability of the array to multiuser beamforming.

6. Conclusions

Antenna arrays in diverse forms and structures are desired for enhanced beamforming functionalities, and the utilization of triangular panels and their combinations to construct 3D arrays has been suggested. The UTAs provide the geometrical advantage over the rectangular counterpart to build various 3D array structures, with possible collaboration of multiple panels for the increased signal strength to the target user. The beam-tilting capability via phase shifting from each panel can also be provided by the proposed codebook for the limited feedback channels. Transmission using the 3D arrays is especially effective for the multiuser scenario, where a large number of users can be simultaneously supported with the improved system throughput.

Data Availability

The simulation data used to support the findings of this study are available from the corresponding author upon request.

Conflicts of Interest

The authors declare that they have no conflicts of interest.

Acknowledgments

This work was supported by the National Research Foundation (NRF) of Korea, MSIP (NRF-2017R1A2B4002367), and by LG Electronics.

References

[1] X. Ge, S. Tu, G. Mao, C. Wang, and T. Han, "5G ultra-dense cellular networks," *IEEE Wireless Communications*, vol. 23, no. 1, pp. 72–79, 2016.

[2] V. Raghavan, A. Partyka, A. Sampath et al., "Millimeter-wave MIMO prototype: measurements and experimental results," *IEEE Communications Magazine*, vol. 56, no. 1, pp. 202–209, 2018.

[3] H. Tullberg, P. Popovski, Z. Li et al., "The METIS 5G system concept: meeting the 5G requirements," *IEEE Communications Magazine*, vol. 54, no. 12, pp. 132–139, 2016.

[4] M. Xiao, S. Mumtaz, Y. Huang et al., "Millimeter wave communications for future mobile networks," *IEEE Journal on Selected Areas in Communications*, vol. 35, no. 9, pp. 1909–1935, 2017.

[5] J. Zhang, X. Ge, Q. Li, M. Guizani, and Y. Zhang, "5G millimeter-wave antenna array: design and challenges," *IEEE Wireless Communications*, vol. 24, no. 2, pp. 106–112, 2017.

[6] J. G. Andrews, T. Bai, M. N. Kulkarni, A. Alkhateeb, A. K. Gupta, and R. W. Heath Jr., "Modeling and analyzing millimeter wave cellular systems," *IEEE Transactions on Communications*, vol. 65, no. 1, pp. 403–430, 2017.

[7] L. Zhou and Y. Ohashi, "Fast codebook-based beamforming training for mmWave MIMO systems with subarray structures," in *Proceedings of the Vehicular Technology Conference (VTC2015-Fall)*, pp. 1–5, Boston, MA, USA, September 2015.

[8] E. Onggoanusi, M. S. Rahman, L. Guo et al., "Modular and high-resolution channel state information and beam management for 5G new radio," *IEEE Communications Magazine*, vol. 56, no. 3, pp. 48–55, 2018.

[9] 3GPP TS 36.211 V10.0.0, "Evolved universal terrestrial radio access (E-UTRA)," *Physical Channels and Modulation*, 2010.

[10] 3GPP TS 36.213 V14.1.0, "Evolved universal terrestrial radio access (E-UTRA)," *Physical Layer Procedures*, 2016.

[11] T. Thomas and F. Vook, "Improving the performance of the UCA when using LTE codebook feedback," in *Proceedings of IEEE Wireless Communications and Networking Conference (WCNC)*, pp. 847–851, Shanghai, China, April 2012.

[12] L. Wu, H. Yang, and D. Wang, "Hadamard transform based codebook design for uniform circular arrays in mobile radio communications," in *Proceedings of IEEE Vehicular Technology Conference (VTC Fall)*, pp. 1–5, Quebec City, Canada, September 2012.

[13] W. M. Dorsey, R. Mital, and D. P. Scholnik, "Phase-only synthesis of omnidirectional patterns with multiple nulls from a uniform circular array," in *Proceedings of IEEE International Symposium on Antennas and Propagation (APSURSI)*, pp. 765-766, Fajardo, Puerto Rico, July 2016.

[14] Q. Nadeem, A. Kammoun, M. Debbah, and M. Alouini, "Spatial correlation characterization of a uniform circular array in 3D MIMO systems," in *Proceedings of the IEEE International Workshop on Signal Processing Advances in Wireless Communications SPAWC'16*, pp. 1–6, Edinburgh, UK, July 2016.

[15] H. Jiacai, S. Yaowu, and T. Jianwu, "Joint estimation of DOA, frequency, and polarization based on cumulants and UCA," *Journal of Systems Engineering and Electronics*, vol. 18, no. 4, pp. 704–709, 2007.

[16] R. Chen, W. Yang, H. Xu, and J. Li, "A 2-D FFT-based transceiver architecture for OAM-OFDM systems with UCA antennas," *IEEE Transactions on Vehicular Technology*, vol. 67, no. 6, pp. 5481–5485, 2018.

[17] L. Zuo, J. Pan, and Z. Shen, "Analytical algorithm for 3-D localization of a single source with uniform circular array," *IEEE Antennas and Wireless Propagation Letters*, vol. 17, no. 2, pp. 323–326, 2018.

[18] S. Zhu, Y. Yang, Y. Wang, Z. He, and Q. Yang, "Beamforming with a line array mounted on an infinite rigid cylindrical baffle," in *Proceedings of the IEEE International Conference on*

Signal Processing, Communications and Computing (ICSPCC), pp. 1–5, Xiamen, China, January 2017.

[19] S. M. Razavizadeh, M. Ahn, and I. Lee, "Three-dimensional beamforming: a new enabling technology for 5G wireless networks," *IEEE Signal Processing Magazine*, vol. 31, no. 6, pp. 94–101, 2014.

[20] H. Ahn, B. Tomasic, and S. Liu, "Digital beamforming in a large conformal phased array antenna for satellite operations support—architecture, design, and development," in *Proceedings of the IEEE International Symposium on Phased Array Systems and Technology*, pp. 423–431, Waltham, MA, USA, October 2010.

[21] M. Henderson, M. B. Davis, and M. Huisjen, "GDPAA advanced technology demonstration overview and results," in *Proceedings of the International Symposium on Phased Array Systems and Technology*, pp. 140–143, Waltham, MA, USA, October 2010.

[22] E. Guangxi and H. Yang, "Design and test of geodesic dome phased array system for multi-target TT& C and communication," in *Proceedings of the International Conference on Optical Communications and Networks (ICOCN)*, pp. 1–3, Hangzhou, China, September 2016.

[23] M. A. Salas-Natera, R. M. Rodriguez-Osorio, and L. de Haro, "Procedure for measurement, characterization, and calibration of active antenna arrays," *IEEE Transactions on Instrumentation and Measurement*, vol. 62, no. 2, pp. 377–391, 2013.

[24] D. Zhu, B. Li, and P. Liang, "A novel hybrid beamforming algorithm with unified analog beamforming by subspace construction based on partial CSI for massive MIMO-OFDM systems," *IEEE Transactions on Communications*, vol. 65, no. 2, pp. 594–607, 2017.

[25] F. Sohrabi and W. Yu, "Hybrid digital and analog beamforming design for large-scale antenna arrays," *IEEE Journal of Selected Topics in Signal Processing*, vol. 10, no. 3, pp. 501–513, 2016.

[26] J.-S. Sheu, "Hybrid digital and analogue beamforming design for millimeter wave relaying systems," *Journal of Communications and Networks*, vol. 19, no. 5, pp. 461–469, 2017.

[27] K. A. R. G. Chandra Mouli, M. S. Anuradha, D. Kuppili, and D. Gopi, "Analysis of rectangular and triangular microstrip antenna arrays using HFSS," in *Proceedings of the International Conference on Electromagnetic Interference and Compatibility (INCEMIC)*, pp. 25–31, Visakhapatnam, India, July 2015.

[28] Y. S. H. Khraisat and M. M. Olaimat, "Comparison between rectangular and triangular patch antennas array," in *Proceedings of the International Conference on Telecommunications (ICT)*, pp. 1–5, Jounieh, Lebanon, April 2012.

[29] 3GPP TR 36.873 V12.2.0, *Study on 3D Channel Model for LTE*, 2015.

[30] C. B. Dietrich, "Diversity antenna configurations for handheld wireless communication terminals," Ph.D. Dissertation, Virginia Polytechnic Institute and State University, Blacksburg, VA, USA, 2000.

Hindawi
International Journal of Antennas and Propagation
Volume 2019, Article ID 3209840, 9 pages
https://doi.org/10.1155/2019/3209840

Research Article

A Compact Wideband Printed Antenna for 4G/5G/WLAN Wireless Applications

Ming Yang,[1,2] Yufa Sun ,[1] and Fan Li[1]

[1]*Key Lab of Intelligent Computing and Signal Processing, Ministry of Education, Anhui University, No. 111, Jiulong Road, Jingkai District, Hefei 230601, China*
[2]*Electronics and Information Engineering Department, Bozhou University, No. 2266, Tangwang Road, Jingkai District, Bozhou 236800, China*

Correspondence should be addressed to Yufa Sun; yfsun_ahu@sina.com

Received 26 January 2019; Revised 3 July 2019; Accepted 17 July 2019; Published 10 September 2019

Guest Editor: Abhinav Kumar

A compact wideband printed antenna with deca-band 4G/5G/WLAN for mobile phone devices is proposed in this paper. The complete structure is composed of a monopole antenna and a coupling strip, occupying a small C-shape PCB area of $27 \times 10.8\ mm^2$. This antenna, which is printed on FR4 substrate with 0.8 mm thickness and fed by a coaxial cable, can provide three wide operating bandwidths that cover 685–1012 MHz, 1596–2837 MHz, and 3288–3613 MHz for 4G/5G/WLAN communication systems. The gains and total radiation efficiencies of the antenna in the low, middle, and high bands are 1.4 dBi–2.5 dBi and 38%–47%, respectively. Besides, the measured results are in good agreement with the simulated results. Further experiments demonstrate that the proposed antenna exhibits a good performance for mobile phones.

1. Introduction

Rapid development of the wireless communication systems, especially the wide use of 2G/3G/4G devices and mobile phone antennas with small sizes and wide operating bands, are more attractive for practical applications. As a particular case, a compact wideband printed mobile phone antenna, covering the LTE (Long-Term Evolution) 700, GSM (Global System for Mobile Communications) 850, GSM900, DCS (Digital Cellular System) 1800, PCS (Personal Communications Service) 1900, UMTS (Universal Mobile Telecommunications System) 2100, LTE2300, LTE2500, and 5G (3300–3600 MHz), is of interest. As is well known, these mobile phone antennas need to be able to operate at a wider scope of different frequencies and work in a very limited space.

Recently, various techniques have been proposed for the design of the multiband or broadband antenna. Several printed wideband antennas for mobile phones have been proposed in the literature [1–6]. However, in order to cover the LTE/WWAN (Wireless Wide Area Network) operation in the 700 MHz band, the radiating board in the printed monopole occupies a large volume, which may be folded to achieve a compact size in the mobile phone. Several techniques have been reported to widen the bandwidth and reduce the occupied space, including the multiple branches technique [7, 8], the reconfigurable method [9, 10], and the lumped-element matching method [11–14]. Another popular technique is the coupled-fed method [15, 16], which provides a convenient matching tuning mechanism. However, these methods cannot simultaneously meet both requirements of wideband operation and compact size. Therefore, it is an interesting challenge to design a wideband and compact mobile phone antenna.

In this paper, a deca-band printed antenna for 4G/5G/WLAN mobile phones with the size of $27 \times 10.8 \times 0.8\ mm^3$ is proposed. A C-shaped ground plane is introduced in this paper to enhance the operating bandwidth of the antenna that is disposed on the C-shaped system circuit board, and the C-shaped ground plane is easier to adjust bandwidth than the antenna that is disposed on the conventional simple system circuit board. The proposed antenna is composed of a monopole antenna and a staircase-shape coupled ground strip. Owing to the coupling interactions, the feeding strip and the parasitic elements may generate multiple resonant modes with the help of the system ground plane. The antenna presents a

measured S_{11} of lower than −6 dB inside the operation bandwidths of LTE700 (704–787 MHz), GSM850 (824–894 MHz), GSM900 (890–960 MHz), DCS (1710–1880 MHz), PCS (1850–1990 MHz), UMTS2100 (1920–2170 MHz), LTE2300 (2305–2400 MHz), and LTE2500 (2500–2690 MHz), meanwhile lower than −10 dB inside the operation bandwidths of WLAN (2400–2484 MHz) and 5G (3300–3600 MHz).

2. Antenna Geometry

The configuration of the proposed antenna is illustrated in Figure 1. Figure 1(a) shows the structure of the proposed antenna fabricated on a C-shaped FR4 substrate with a size of $120 \times 60\ \text{mm}^2$, a relative permittivity of 4.4, a thickness of 0.8 mm, and a loss tangent of 0.02. The dimensions of the proposed antenna are $27 \times 10.8\ \text{mm}^2$, located at the lower left edge of the substrate. The selected dimensions of the overall circuit board and the antenna are reasonable for practical mobile phones. The proposed antenna consists of a monopole antenna, a staircase-shaped coupled ground strip, and a 6.8 nH inductor, as shown in Figure 1(b). The driven strip, coupled ground strip, and ground plane are printed on the front side of the substrate. In the proposed antenna, the driven strip is connected (point A) to the ground plane by a 50 Ω coaxial cable, and the coupled strip is connected directly to the ground plane (point B) on the same side.

The driven strip is composed of four branches, strips 1, 2, 3, and 4, as shown in Figure 1(b), which contributes the resonant modes at lower and higher frequency bands. By adding the staircase-shaped coupled ground strip, the interaction between the driven strip and the coupled strip may generate another resonant mode around 2260 MHz, thereby improving the impedance matching and widening the middle bandwidth. To enhance the bandwidth of the middle and high band, an inductor is introduced to create two resonant frequencies around 2740 MHz and 3450 MHz. The proposed antenna is studied and discussed in detail in next section.

3. Antenna Design and Analysis

3.1. Antenna Design. In order to meet the requirements of the modern mobile phone with the deca-band 4G/5G/WLAN operation, the proposed antenna must provide multiple resonances. For convenient explanation, comparison of the simulated S_{11} of various geometric structures of the antenna is shown in Figure 2. First, antenna #1 is a monopole antenna, which generates a resonant mode only at a frequency of 1390 MHz. Next, strip 2 is added to the antenna #1, which forms antenna #2. Note that three resonant modes are excited at 672 MHz, 986 MHz, and 3752 MHz, and the impedance matching is good in the resonant modes. The antenna #3 is composed of a staircase-shaped coupled ground strip and antenna #2, which excites another resonant mode and enhances the bandwidth as 1610–2580 MHz. The antenna #4 is formed by inserting strip 3 in antenna #3. The two resonances of the lower band are shifted to the left, while the resonance of the higher band is shifted to the right. However, the corresponding bandwidths for these resonances are not wide enough to cover the whole frequency bands for LTE/WWAN/WLAN/5G.

Next, as antenna #5, an inductor is introduced in antenna #4 to enhance the bandwidth. Two resonant modes are excited at 2740 MHz and 3450 MHz with a good impedance matching. The middle and high bands cover DCS/PCS/UMTS/LTE2300/2500 and 5G (3300–3600 MHz). The lower bands LTE700/GSM850 can also be covered by optimizing the inductance.

To achieve a wide coverage in the 900 MHz band, a meander line (strip 4) is inserted into antenna #5, that is, the proposed antenna. The resonant frequency in the low band is split into three modes. Consequently, the proposed antenna may cover the LTE700, GSM850, and GSM900.

Here, we employ HFSS (high-frequency structure simulator) full-wave simulator to optimize the antenna configuration and achieve its surface current and gain. The optimized design parameters have been determined and listed in Table 1.

3.2. Parametric Analysis. In the design of this antenna, the value of the inductor L and the length of $H6$ are changed, respectively, and their effects on each resonant mode are shown in Figures 3 and 4. It can be seen in Figure 3 that the antenna's bandwidths are affected when a smaller or bigger value of L is selected, especially for the antenna's middle and high bands. In Figure 4, the results of the simulated S_{11} for the length $H6$ varying from 12.7 to 16.7 mm are presented. Relatively remarkable effects on the resonant modes in the low and middle bands are observed. Other resonant modes are generally insensitive to the length of $H6$.

4. Simulation and Measurement

Figure 5 shows the fabricated prototype of the proposed antenna, which is fed by a 50 Ω coaxial cable. S_{11} of the antenna is measured by using an Agilent N5247A vector network analyzer. The simulated and measured S_{11} are plotted in Figure 6. It may be observed that the simulated and measured results in lower and higher bands are in good agreement, while there is a small discrepancy between the simulation and measurement results in the middle band, which may be mainly due to the fabrication inaccuracy of the antenna prototype. According to −6 dB reflection coefficients, the measured impedance bandwidths of the antenna for lower and middle bands were 685–1012 MHz and 1596–2837 MHz, respectively. Meanwhile, the measured impedance bandwidths lower than −10 dB for WLAN and 5G (3300–3600 MHz) were 2146–2568 MHz and 3288–3613 MHz. Thus, the proposed antenna provides all ten operating bands, i.e., LTE700/2300/2500, GSM850/900/1800/1900/UMTS2100/WLAN, and 5G (3300–3600 MHz).

To further comprehend the resonant mechanisms of the proposed antenna, the surface current distributions are simulated in Figure 7. As shown in Figure 7(a), the surface current at 740 MHz is distributed along the longer strip (E-F-G-H) and the staircase-shaped coupled ground strip (E-C), which can provide a 0.25-wavelength resonant mode (for M_1). By observing Figure 7(b), the surface current distributes

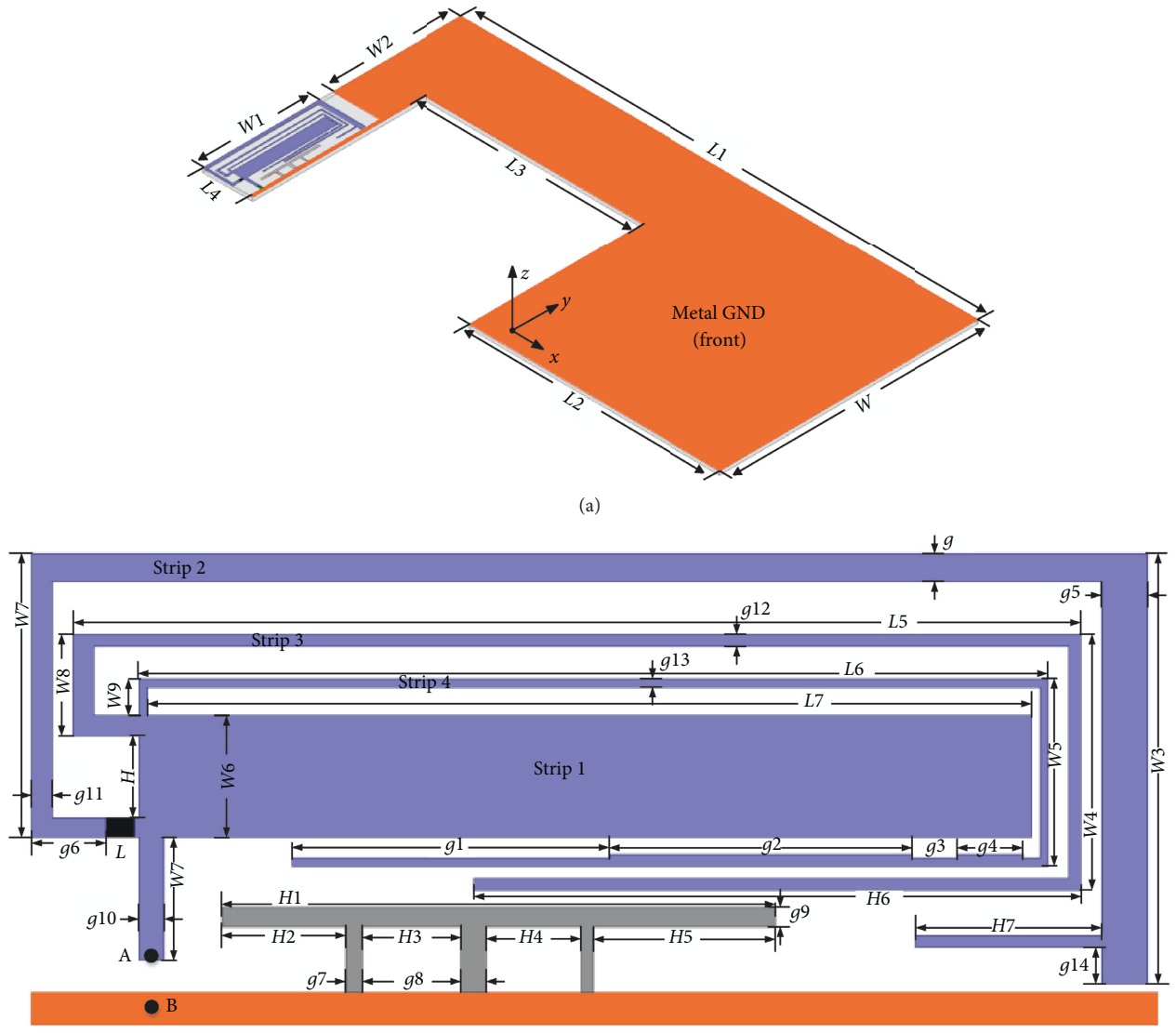

Figure 1: Geometry of the proposed antenna. (a) The overall structure of the proposed antenna and (b) the important part structure of the proposed antenna.

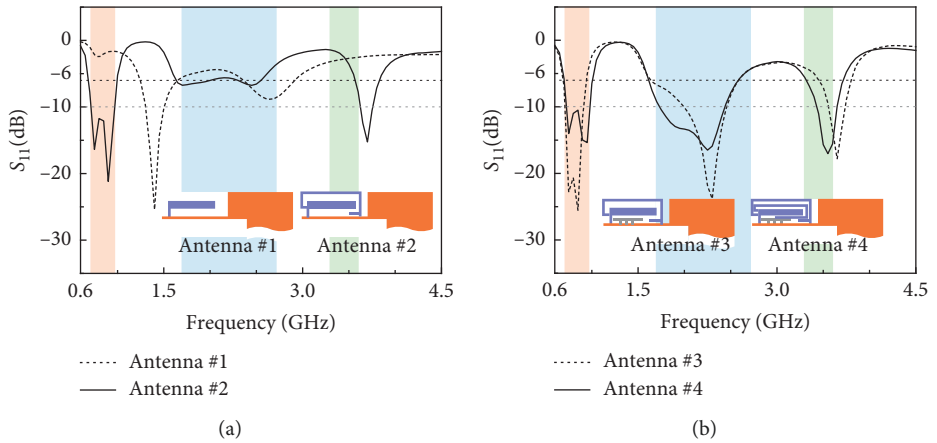

Figure 2: Continued.

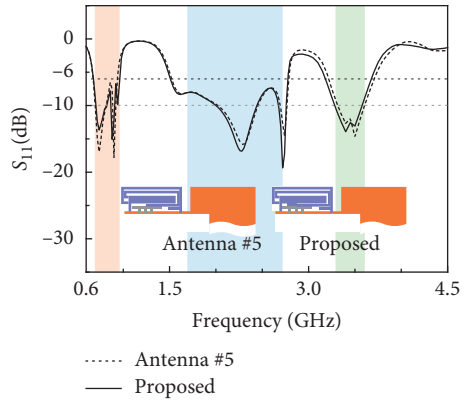

(c)

Figure 2: Simulation results of the S_{11} for the different antennas.

Table 1: Geometric parameters for the proposed antenna (unit: mm).

Parameter	Value
W	60.0
$W1$	27.0
$W2$	30.0
$L1$	120.0
$L2$	58.0
$L3$	50.4
$L4$	10.8
$W3$	10.6
$W4$	6.3
$W5$	4.6
g	0.7
$g3$	1.1
$g4$	1.6
$g2$	7.3
$H7$	4.5
$H6$	14.7
$L5$	24.4
$L6$	22.0
$L7$	21.4
$H1$	13.4
$H2$	3.0
$H3$	2.4
$H4$	2.3
$H5$	4.4
$g1$	7.7
$g6$	1.8
$g7$	0.4
$g8$	0.6
$g5$	1.1
$g9$	0.5
$W6$	3.0
$W7$	7.0
$W8$	2.5
$W9$	0.9
H	2.0
$g10$	0.6
$g11$	0.5
$g12$	0.3
$g13$	0.2
$g14$	0.9

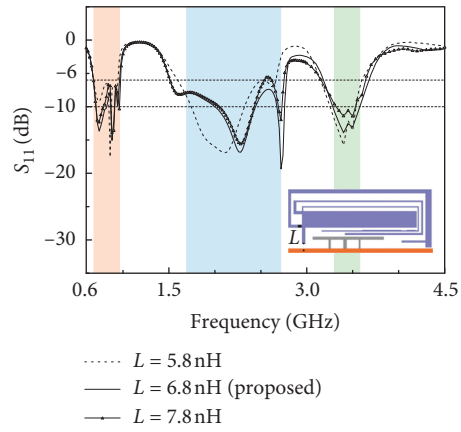

Figure 3: Simulated S_{11} as a function of the value inductor L for the proposed antenna.

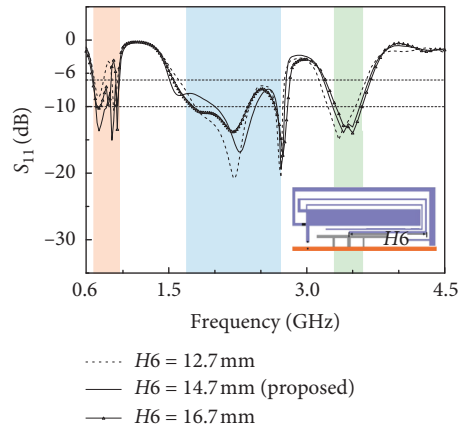

Figure 4: Simulated S_{11} as a function of the length $H6$ for the proposed antenna.

along the shorter strip (E-F-N), which can provide a 0.25-wavelength resonant mode at 2300 MHz (for M_2).

The simulated surface current distribution at 2730 MHz for the antenna is plotted in Figure 7(c), in which intense current

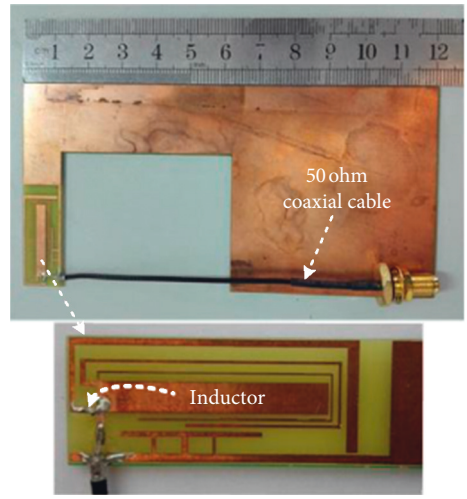

Figure 5: Photograph of the antenna.

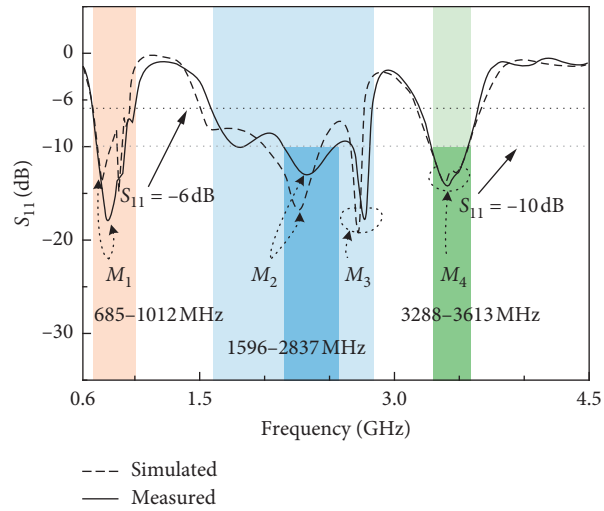

Figure 6: Simulated and measured S_{11} of the proposed antenna.

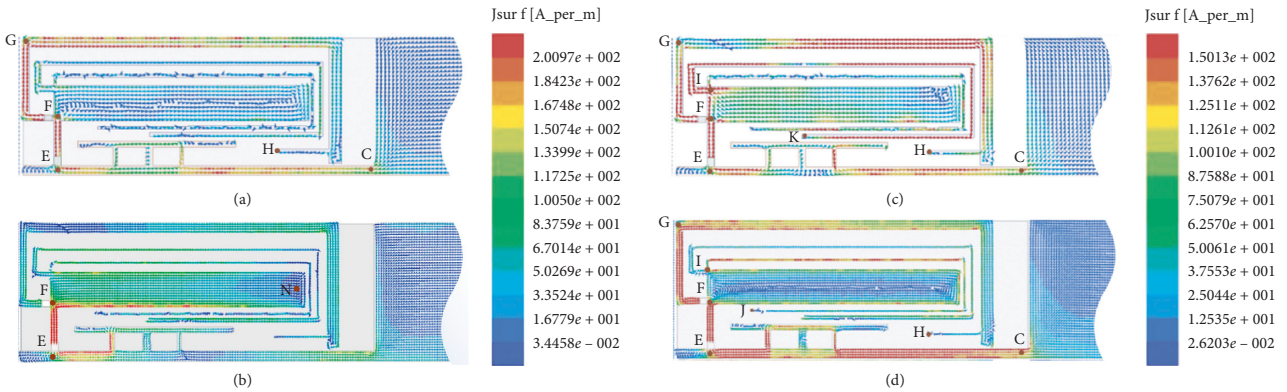

Figure 7: Simulated current distributions on metallic radiators of the proposed antenna at (a) 740 MHz, (b) 2300 MHz, (c) 2730 MHz, and (d) 3450 MHz.

distributions can be observed around the paths E-F-G-H, E-F-I-K, and E-C. That occurs because the paths E-F-G-H, E-F-I-K, and E-C operate at 0.25-wavelength mode (for M_3).

Moreover, Figure 7(d) shows that the fundamental mode is excited at 3450 MHz with maximum strength along the meandered arm (E-F-G-H and E-I-J) and the

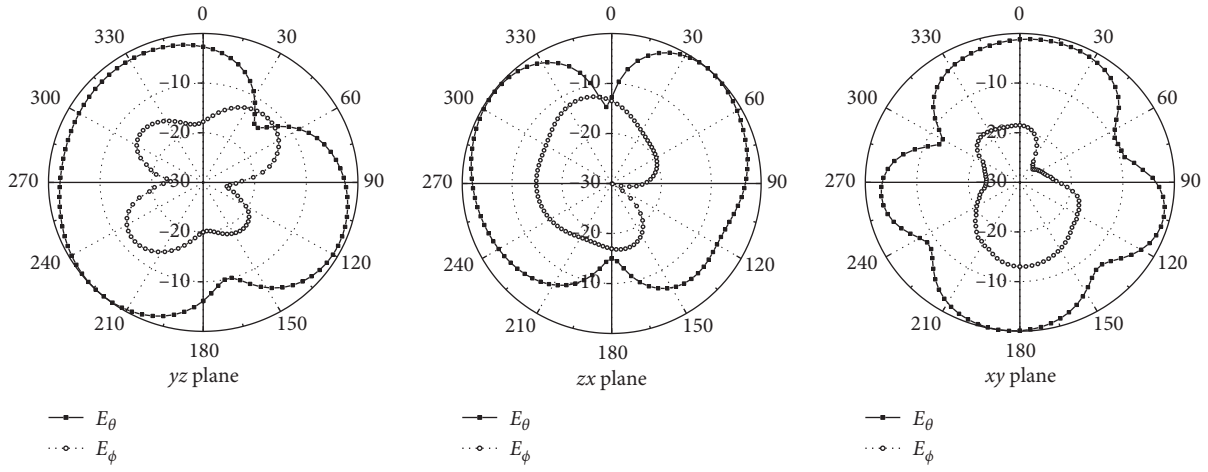

(a)

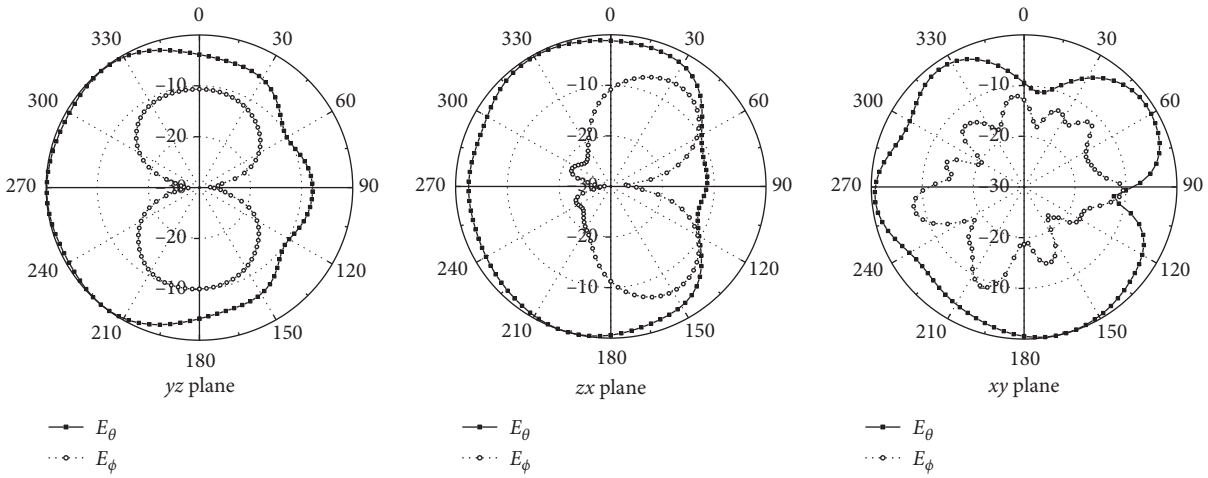

(b)

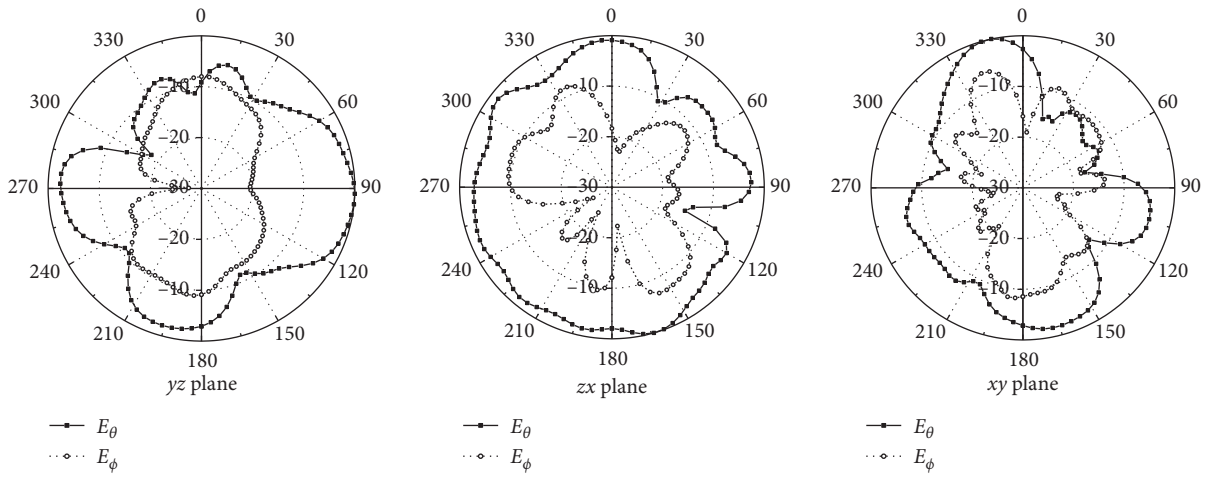

(c)

Figure 8: Continued.

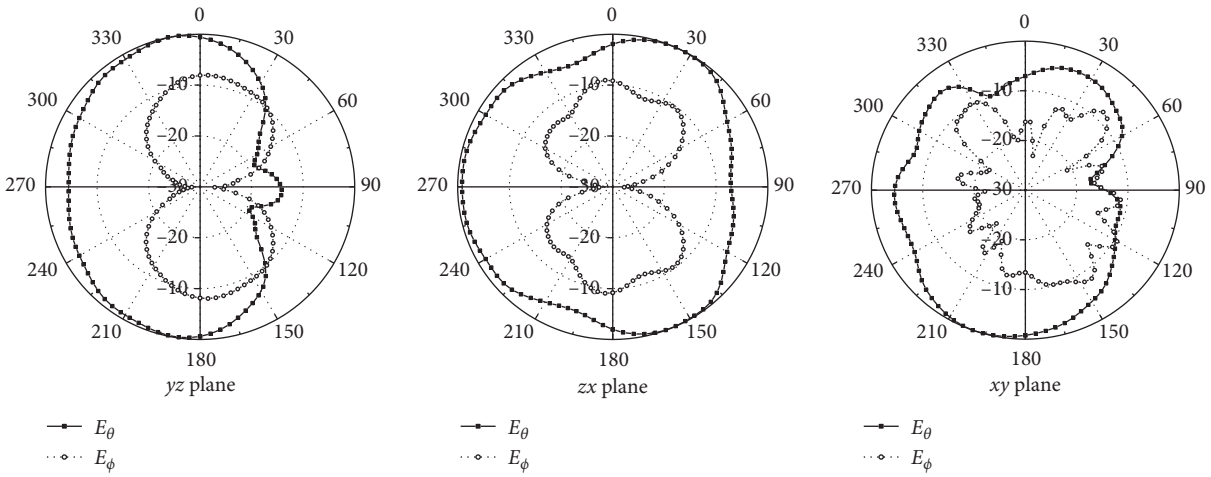

Figure 8: Measured radiation patterns of the proposed antenna at (a) 750 MHz, (b) 1800 MHz, (c) 2500 MHz, and (d) 3450 MHz.

staircase-shaped coupled ground strip (E-C), which works at the 0.25-wavelength mode of the strip section at 3450 MHz (for M_4).

Figure 8 shows the measured radiation patterns of the proposed antenna at 750, 1800, 2500, and 3450 MHz. Based on the direction of the antenna placement in Figure 1, the copol (E_θ) and crosspol (E_ϕ) in the *yoz*, *zox*, and *xoy* planes are measured. As can be seen from Figure 8, E_θ varies smoothly in *yoz* and *zox* planes which presented omnidirectional radiation. At 750 MHz, the E_θ radiation pattern appears as a figure-8 shape and is stronger than the E_ϕ radiation pattern. More variations can be observed in the radiation patterns at the *xoy* plane, but this radiation has little influence on the proposed antenna's overall characteristics. By comparing E_θ and E_ϕ in the analysis table, the proposed antenna exhibits remarkable characteristics of directivity and polarization which can meet the requirement of antenna directionality.

The measured antenna gain and radiation efficiency of the fabricated antenna are shown in Figure 9. Within the desired LTE700/GSM850/900 bands, i.e., 704–960 MHz, the measured antenna gain is about 1.4–1.9 dBi, and the corresponding radiation efficiency varies from 38% to 43%. Besides, for the middle operation band for DCS1800/PCS1900/UMTS2100 and LTE2300/2500 bands (1710–2690 MHz), the measured antenna gain is about 1.7–2.2 dBi, and the corresponding total radiation efficiency is larger than 40%. In the high band for 5G (3300–3600 MHz), the measured gain of the antenna varies from 2.2 to 2.5 dBi, and the radiation efficiency is from 45% to 47%. As a result, the measured efficiency and gain of the proposed antenna meet the requirement of the mobile phone systems.

Performances of the proposed antenna are compared with that of some typical mobile phones in terms of their frequency bands, dimensions, structures, and bandwidth in Table 2. In this table, we can find that the antennas in [9, 10]

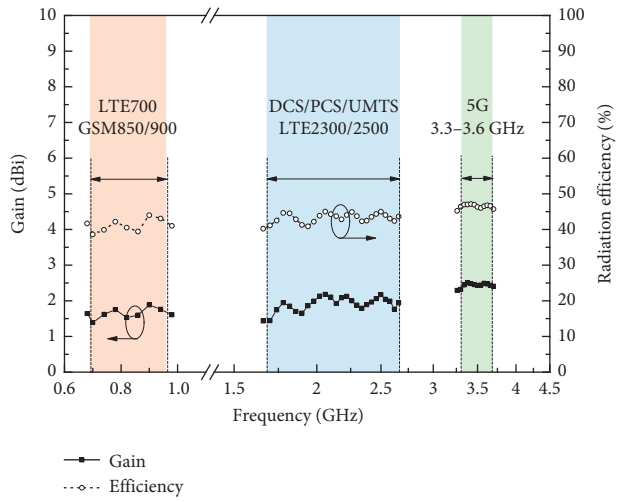

Figure 9: Measurement results for the gain and efficiency of the proposed antenna.

have a thin antenna thickness using the lumped elements, while the size of which is larger than that of the proposed antenna. The antennas in [4, 5] also have a thin antenna thickness, but they use double PCBs (printed circuit boards). The antennas in [1, 16] do not use any lumped elements, while suffering from a thickness of greater than 5 mm. The areas of antennas in [8, 15] are larger than that of the proposed antenna, and they do not cover the LTE700 band, which is the most difficult to be covered and crucial for LTE/WLAN (Wireless Local Area Networks) mobile phones. However, the proposed antenna can cover three frequency bands (685–1012 MHz, 1596–2837 MHz, and 3288–3613 MHz), furthermore S_{11} lower than −10 dB inside the operation bandwidths of WLAN (2400–2484 MHz) and 5G (3300–3600 MHz). This antenna has smaller size and single-layer structure than other multiple resonance antennas in literatures.

Table 2: Comparison of the proposed antenna and reference antennas.

Reference	Frequency band[a]	Dimension (mm^3)	Structure	Bandwidth (MHz)	S_{11} (dB)
[1]	Octa-band	$80 \times 6 \times 5.8$	Multilayer	670–1020/1650–2920	−6
[4]	Octa-band	$60 \times 15 \times 0.8$	Double layer	740–965/1380–2703	−6
[5]	Nona-band	$60 \times 10 \times 0.8$	Double layer	698–960/1710–2170	−6
[8]	Hepta-band	$70 \times 8 \times 5$	Multilayer	824–960/1710–2690	−6
[9]	Octa-band	$36.5 \times 10 \times 1.6$	Single layer	790–1030/1710–2230	−6
[10]	Hepta-band	$28 \times 15 \times 4$	Multilayer	808–965/1696–3000	−6
[15]	Hepta-band	$60 \times 5 \times 5$	Multilayer	760–960/1510–2720	−6
[16]	Octa-band	$70 \times 8 \times 5.8$	Multilayer	690–970/1680–2740	−6
Proposed	Deca-band	$27 \times 10.8 \times 0.8$	Single layer	685-1012/1596-2837/3288-3613	−6 and −10

[a]Hepta-band: GSM850/900/DCS/PCS/UMTS/LTE2300/2500. Octa-band: LTE/WWAN. Nona-band: LTE/WWAN/WLAN. Deca-band: LTE/WWAN/WLAN/5G (3300–3600 MHz).

5. Conclusion

A compact wideband printed antenna for deca-band operation is proposed. The antenna is formed by merging four strips, a staircase-shaped coupled ground strip and an inductor which can provide three wide bandwidths of 685–1012 MHz, 1596–2837 MHz, and 3288–3613 MHz. These bands can cover the standard LTE700/2300/2500, GSM850/900, DCS, PCS, UMTS, 2.4 GHz WLAN, and 5G (3300–3600 MHz). Furthermore, good efficiency of more than 38% and peak gains from 1.4 dBi to 2.5 dBi are achieved across the three bands. The measured results indicate that the proposed antenna is suitable for the applications in mobile phones for LTE/4G/5G/WLAN operations.

Data Availability

The data used to support the findings of this study are available from the corresponding author upon request.

Conflicts of Interest

The authors declare that they have no conflicts of interest.

Acknowledgments

This work was supported by the National Natural Science Foundation of China under Grant no. 61172020 and the Key Program in the Youth Elite Support Plan in Universities of Anhui Province under Grant no. gxyqZD2016521.

References

[1] D. Huang, Z. Du, and Y. Wang, "An octa-band monopole antenna with a small non-ground portion height for LTE/WLAN mobile phones," *IEEE Transactions on Antennas and Propagation*, vol. 65, no. 2, pp. 878–882, 2017.

[2] P. Wang, Y. Shao, D. Huang, and M. A. Basit, "A compact coupled-fed loop antenna for mobile LTE smartphones," *International Journal of Antennas and Propagation*, vol. 2018, Article ID 8426574, 8 pages, 2018.

[3] H. Xu, H. Wang, S. Gao et al., "A compact and low-profile loop antenna with six resonant modes for LTE smartphone," *IEEE Transactions on Antennas and Propagation*, vol. 64, no. 9, pp. 3743–3751, 2016.

[4] J. Dong, X. Yu, and L. Deng, "A decoupled multiband dual-antenna system for WWAN/LTE smartphone applications," *IEEE Antennas and Wireless Propagation Letters*, vol. 16, pp. 1528–1532, 2017.

[5] Y. Liu, P. Q. Liu, Z. J. Meng, L. F. Wang, and Y. Li, "A planar printed nona-band loop-monopole reconfigurable antenna for mobile handsets," *IEEE Antennas and Wireless Propagation Letters*, vol. 17, no. 7, pp. 1575–1579, 2018.

[6] Z. Yu, J. Yu, X. Ran, and C. Zhu, "A novel Koch and Sierpinski combined fractal antenna for 2G/3G/4G/5G/WLAN/navigation applications/4G/5G/WLAN/navigation applications," *Microwave and Optical Technology Letters*, vol. 59, no. 9, pp. 2147–2155, 2017.

[7] Y.-L. Ban, Y.-F. Qiang, G. Wu, H. Wang, and K.-L. Wong, "Reconfigurable narrow-frame antenna for LTE/WWAN metal-rimmed smartphone applications," *IET Microwaves, Antennas & Propagation*, vol. 10, no. 10, pp. 1092–1100, 2016.

[8] Y. Liu, Y.-M. Zhou, G.-F. Liu, and S.-X. Gong, "Heptaband inverted-F antenna for metal-rimmed mobile phone applications," *IEEE Antennas and Wireless Propagation Letters*, vol. 15, pp. 996–999, 2016.

[9] S. W. Lee and Y. Sung, "Compact frequency reconfigurable antenna for LTE/WWAN mobile handset applications," *IEEE Transactions on Antennas and Propagation*, vol. 63, no. 10, pp. 4572–4577, 2015.

[10] Y. Xu, Y.-W. Liang, and H.-M. Zhou, "Small-size reconfigurable antenna for WWAN/LTE/GNSS smartphone applications," *IET Microwaves, Antennas & Propagation*, vol. 11, no. 6, pp. 923–928, 2017.

[11] D. Huang and Z. Du, "Eight-band antenna with a small ground clearance for LTE metal-frame mobile phone applications," *IEEE Antennas and Wireless Propagation Letters*, vol. 17, no. 1, pp. 34–37, 2018.

[12] H. Chen and A. Zhao, "LTE antenna design for mobile phone with metal frame," *IEEE Antennas and Wireless Propagation Letters*, vol. 15, pp. 1462–1465, 2016.

[13] L.-W. Zhang, Y.-L. Ban, C.-Y.-D. Sim, J. Guo, and Z.-F. Yu, "Parallel dual-loop antenna for WWAN/LTE metal-rimmed smartphone," *IEEE Transactions on Antennas and Propagation*, vol. 66, no. 3, pp. 1217–1226, 2018.

[14] K.-L. Wong and C.-Y. Tsai, "IFA-based metal-frame antenna without ground clearance for the LTE/WWAN operation in the metal-casing tablet computer," *IEEE Transactions on Antennas and Propagation*, vol. 64, no. 1, pp. 53–60, 2016.

[15] Y. Yang, Z. Zhao, W. Yang, Z. Nie, and Q.-H. Liu, "Compact multimode monopole antenna for metal-rimmed mobile phones," *IEEE Transactions on Antennas and Propagation*, vol. 65, no. 5, pp. 2297–2304, 2017.

[16] R. Tang and Z. Du, "Wideband monopole without lumped elements for octa-band narrow-frame LTE smartphone," *IEEE Antennas and Wireless Propagation Letters*, vol. 16, pp. 720–723, 2017.

Hindawi
International Journal of Antennas and Propagation
Volume 2019, Article ID 6098483, 8 pages
https://doi.org/10.1155/2019/6098483

Research Article

Low-RCS, Circular Polarization, and High-Gain Broadband Antenna Based on Mirror Polarization Conversion Metasurfaces

Liang Zhang,[1,2] **Changqing Liu**,[1] **Chun Ni**,[2] **Meng Kong**,[2] **and Xianliang Wu**[1]

[1]*Key Lab of Intelligent Computing & Signal Processing, Ministry of Education, Anhui University, Hefei 230601, China*
[2]*Key Laboratory of Simulation and Design for Electronic Information System of Anhui Province, Hefei 230601, China*

Correspondence should be addressed to Liang Zhang; liangzh@hfnu.edu.cn

Received 22 February 2019; Revised 28 June 2019; Accepted 24 July 2019; Published 6 August 2019

Guest Editor: Massimo Donelli

In this paper, a novel slot antenna array that is based on mirror polarization conversion metasurfaces (MPCM) is proposed. It achieves circular polarization (CP) and effectively reduces the radar cross section (RCS) and increases gain in the entire x-band. This design uses the mirrored composition of the polarization conversion metasurfaces (PCM) on the top surface of the substrate. The MPCM covers a 2×2 slot antenna array that is fed with by a sequentially rotating network. The CP radiation is realized by the polarization conversion characteristics of the PCM. At the same time, the reduction of RCS is achieved by 180° ($\pm 30^{\circ}$) reflection phase difference between two adjacent PCMs. The improvement in gain is achieved by using a Fabry–Perot cavity, which is constituted by the ground of the antenna and the PCM. Simulated and measured results show that approximately 46.4% of the operating bandwidth is in the range of 7.5–12 GHz (AR < 3 dB) and the gain of the antenna with MPCM is at least 5 dB higher than the reference antenna. Moreover, the monostatic RCS is reduced from 8 to 20 GHz.

1. Introduction

With the rapid development of modern radio technology, great breakthroughs have been made in wireless communication systems, radar navigation, carrier stealth, and other related fields. A multifunction antenna based on electromagnetic metasurfaces can adequately satisfy the requirements of complex systems and concurrent tasks. Therefore, developing a high-gain antenna with a low radar cross section (RCS) that produces circular polarization (CP) is an important subject among experts and scientists [1–8].

A metasurface (MS) is a two-dimensional metamaterial structure with a low profile, low loss, and a simple design. MS has many significant advantages in polarization control, and it has been used in low-RCS antenna as well as RCS reduction design [6–14]. Recently, Akgol et al. proposed a metasurface that uses a polarization converter to convert linear polarization signals to circular polarization signals while having a 3 dB axial ratio bandwidth of 800 MHz [3–5]. In [6–8], the idea of using a partial reflector to achieve a low RCS and high gain was proposed. By adding a resistor to the structure, the energy of the incoming electromagnetic wave can be absorbed to reduce the backward RCS. However, due to the need to weld a large number of resistors, it is difficult to manufacture the antenna in practice. In [10], a new metamaterial surface antenna based on the chessboard polarization conversion metasurface (CPCM) was proposed. Using this approach, a broadband antenna with low RCS, CP, and high gain could be realized by placing a 12 mm MS above the feed antenna. However, the antenna requires a large volume and the axial ratio (AR) bandwidth is narrow. In [11], an MS-based antenna array was proposed, which could realize both circular polarization and RCS reduction, providing a good method for RCS reduction; however, the antenna structure is complex and the impedance bandwidth is narrow. Although the method proposed above has made significant progress, the application of MS experiences considerable shortcomings. In the state-of-the-art designs, low-profile antennas that simultaneously achieve wideband RCS reduction and wideband CP remain a challenge.

To further realize the integration of multiple performances on one antenna, this paper proposes a broadband low-RCS, low-profile CP, high-gain antenna based on mirror supersurface. The AR bandwidth is expanded by means of sequential

rotation feeding [15, 16]. Circular polarization, RCS reduction, and gain enhancement can be realized in the entire x-band. The antenna array achieves a larger RCS reduction and AR bandwidth than the CP slot antenna that is described in published literature. Compared with the low-RCS Fabry–Perot resonant cavity that is based on MS, the proposed antenna has an important advantage. It is low profile and without air gap, which means that it can be applied in many fields.

2. Design of the Mirror Polarization Conversion Metamaterials

2.1. Structure of the Antenna. Figures 1(a)–1(c) illustrate the structure of the antenna, which is composed of an MPCM and a slot antenna array (as the source antenna). The MPMS consists of four parts: Part I is an MPCM, parts II and IV are its mirror images, and part III is the mirror image of part II. Figure 2(a) shows an enlarged view of the PCM with a linear polarization (LP) slot antenna source. The PCM is composed of 4×4 square cells with different corners truncated on both sides. In order to expand the AR bandwidth, the feed antenna is supplied data from the network as it rotates in sequence. The phase distribution is 0°, 90°, 180°, and 270°, as shown in Figure 1(c). The substrate utilized is Rogers RO4003C with $\varepsilon_r = 3.55$ and a loss tangent of $\delta = 0.0027$. The optimized widths are as follows: $w1 = 0.18$ mm, $w2 = 0.47$ mm, $w3 = 0.16$ mm, $w4 = 0.31$ mm, $w5 = 0.47$ mm, $w6 = 0.13$ mm, $w7 = 0.47$ mm, $w8 = 0.9$ mm, and $wf = 1.13$ mm and $r = 3.5$ mm.

Each PCM performs three functions. First, when an LP wave passes through the PCM, it is converted into CP wave. Second, the PCM can achieve reflective wave wideband polarization conversion. Third, an increase in the gain is realized by the Fabry–Perot cavity that is formed by the slot array antenna and the PCM. Obviously, it is very difficult to adjust these three functions at the same time. Therefore, the objective of this research is to balance these features. The general procedure for the design of the PCM can be summarized as follows:

(1) The unit cell PCM, covering the operation band (8–12 GHz) of the antenna, is designed to obtain the initial parameters

(2) The copolarization and cross-polarization transmission coefficients are modified by optimizing the diagonal corner truncated on both sides of the unit cell. This will convert the LP wave into the CP wave

(3) Optimize the x-component and y-component of the reflection coefficient to meet the Fabry–Perot resonance condition of CP

(4) Optimize the polarization conversion unit cell with flooring (Figure 3) to realize broadband polarization conversion

(5) Repeat steps 2–4 until the process is complete

Following the design steps above, the final parameters of the unit cell are as follows: $a = 4.6$ mm, $d1 = 1.2$ mm, $d2 = 2.8$ mm, $c = 0.4$ mm, $b = 25$ mm, $Ws = 2.2$, $Ls = 14.4$ mm, $L1 = 3.9$ mm, $h0 = 0.508$ mm, and $h1 = 2$ mm.

2.2. Analysis of the Circular Polarization. One way to describe an array antenna is that it consists of four PCM-based CP antennas, which are arranged in 90° rotations. An equivalent circuit can be used to explain the formation of CP. In Figure 2(a), the structure within the area enclosed by the red square can be considered a new unit. When the PCM is placed on the slot antenna, which is LP along the y-axis, an E-field is generated along the y-axis. The E-field is broken down into orthogonal components $\vec{E}_1$ and $\vec{E}_2$, as shown in Figure 2(c). If the diagonal of the unit is not truncated, due to the symmetry of the structure, as shown in Figure 2(b), the orthogonal components $\vec{E}_1$ and $\vec{E}_2$ constitute an RLC circuit with an impedance given by [17]

$$Z = 2R + j\omega(2L) + \frac{1}{j\omega C} = R' + jX', \tag{1}$$

where L and R are the inductance and resistance of the patch and C is the capacitance generated by the gap between nearby and related units. When the diagonal corners are truncated as shown in Figure 2(c), the perpendicular E-field components that are broken down by the PCM will cause two different impedances, $Z_1$and Z_2. The expression for the two impedances is shown in the following equations:

$$Z_1 = R_1' + jX_1', \tag{2}$$

$$Z_2 = R_2' + jX_2'. \tag{3}$$

The truncation corner increases the gaps between nearby and related patches, thereby increasing the value of X_1' and decreasing the value of X_2'. Thus, the phase difference between Z_1 and Z_2 can be changed by modifying the value of the truncated corners on both sides. If the PCM is designed such that $|Z_1| = |Z_1|$ and $\angle Z_2 - \angle Z_1 = 90°$, then $|\vec{E}_1| = |\vec{E}_2|$ and $\angle \vec{E}_2 - \angle \vec{E}_1 = 90°$.

Figure 4(a) presents a comparison of the reflection coefficients for slot antennas both with and without PCM. As shown in Figure 4(b), the axial ratio (AR < 3 dB) bandwidth of the slot antenna with PCM ranges from 9.2 to 10 GHz. The results show that PCM can have the ability to transform the LP wave into a CP wave. In addition, the gain has been improved. The reasons for this improvement are explained in the following section.

2.3. Mechanism of High-Gain Performance. A metamaterial surface (MS) is essentially the surface distribution of a small electrical scatterer [18]. Due to its planar structure, it can be easily combined with a planar antenna to form a resonant cavity. As shown in Figure 2(a), when the spacing between the reflective floor and the MS meets the resonance condition, the electromagnetic wave is constantly reflected back and forth in the resonant cavity. Also, the electromagnetic wave transmitted through the MS can be superimposed with the phase each time. Thus, the gain and beam width of the antenna are improved, and the radiation energy can be directed by adjusting the height between the two plates. According to the analysis in the literature [19], two resonant modes (TM_{10} mode and antiphase TM_{20} mode) are simultaneously excited to load the metamaterial

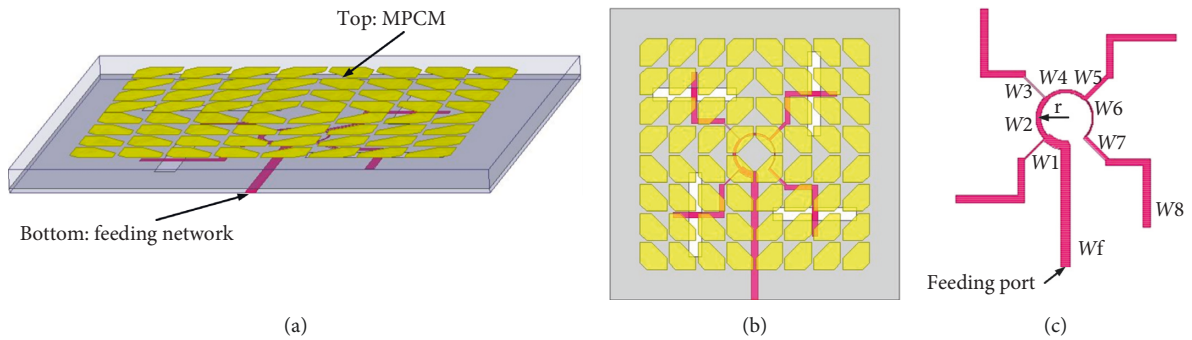

Figure 1: (a) The schematic view of the array. (b) The top view of the array. (c) The feeding network.

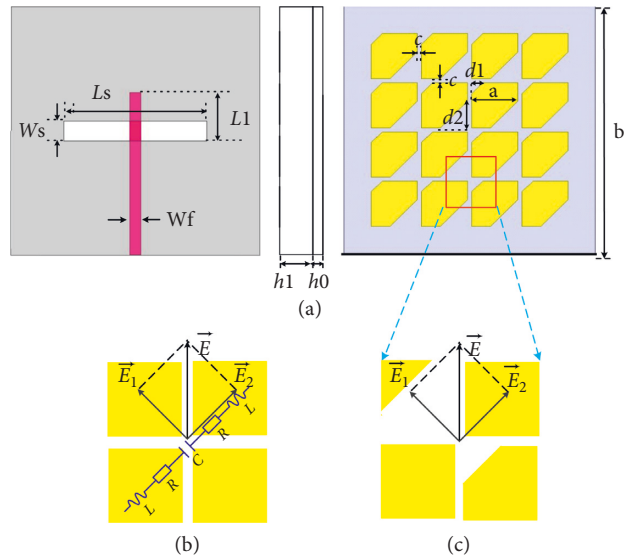

Figure 2: (a) CP antenna. (b) New unit cell without truncation. (c) New unit cell with diagonal.

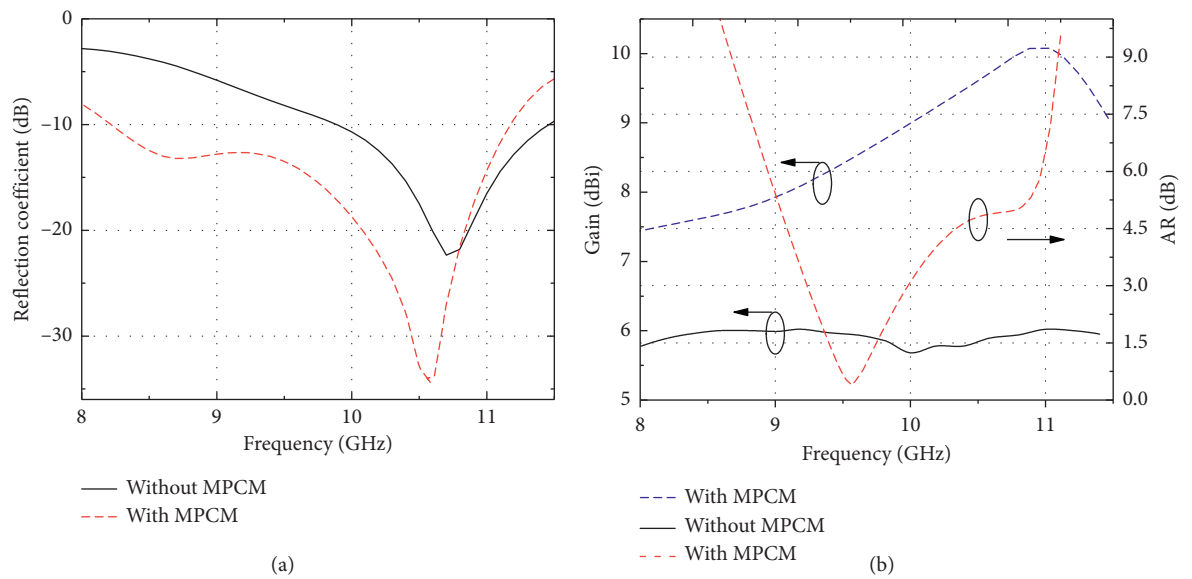

Figure 3: Simulated (a) reflection coefficients and (b) boresight gain and AR versus frequency of the slot antenna with and without PCM.

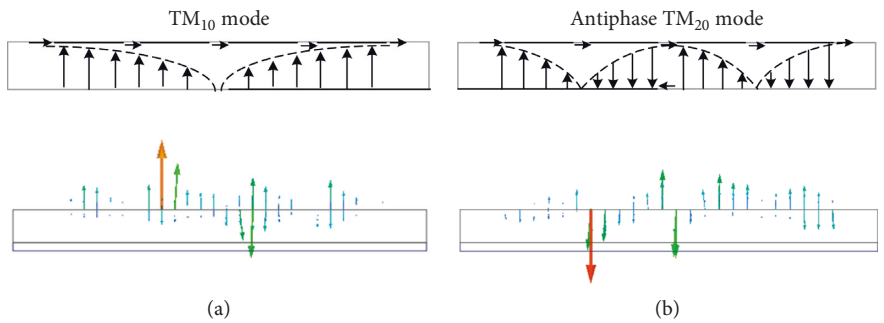

Figure 4: Two resonant modes of the proposed antenna. (a) 8.6 GHz and (b) 10.5 GHz.

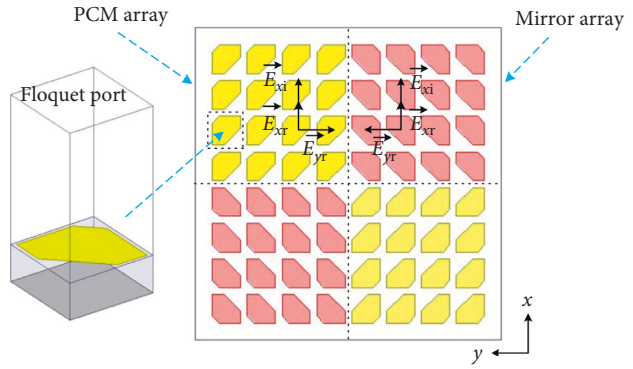

Figure 5: The PCM unit cell and top view of a mirror composed of four parts.

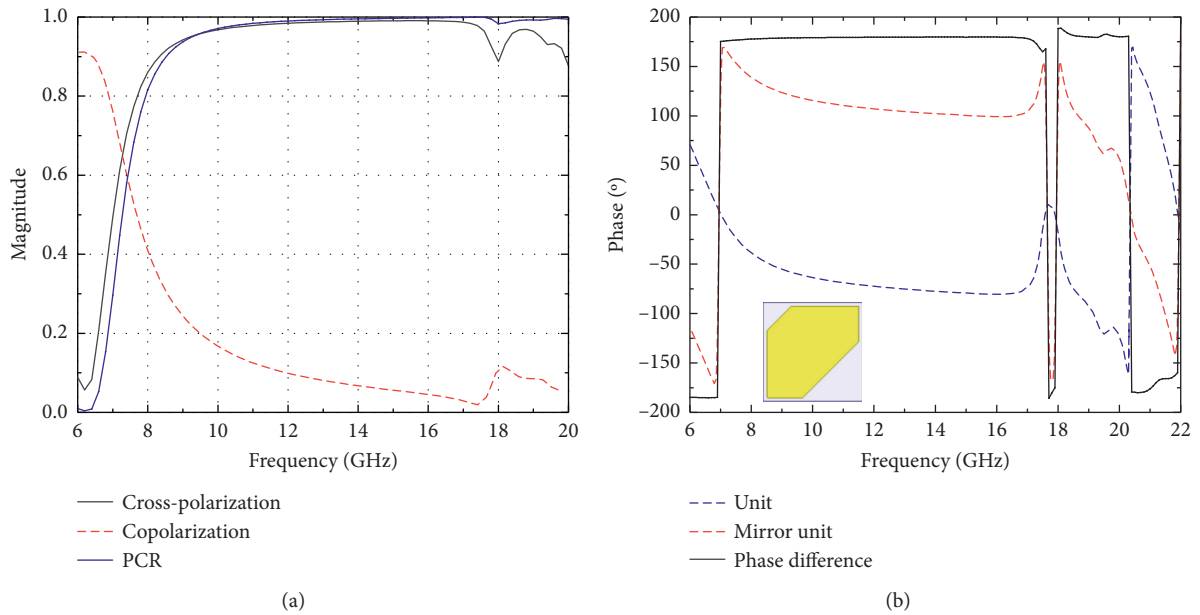

Figure 6: (a) Reflection coefficients of copolarization, cross-polarization, and PCR. (b) The cross-polarized reflection phase difference between the infinite periodic unit cell and its mirror.

element of the slot antenna. This in turn leads to the low-profile wideband LP antenna. Due to the distribution of the truncated diagonal corner, the impedance matching bandwidth is improved. However, the gain is less affected. Figures 5(a) and 5(b) show the electric field distribution at two distinct frequencies (8.6 and 10.5 GHz), verifying its two resonant modes: TM_{10} mode and TM_{20} inversion mode.

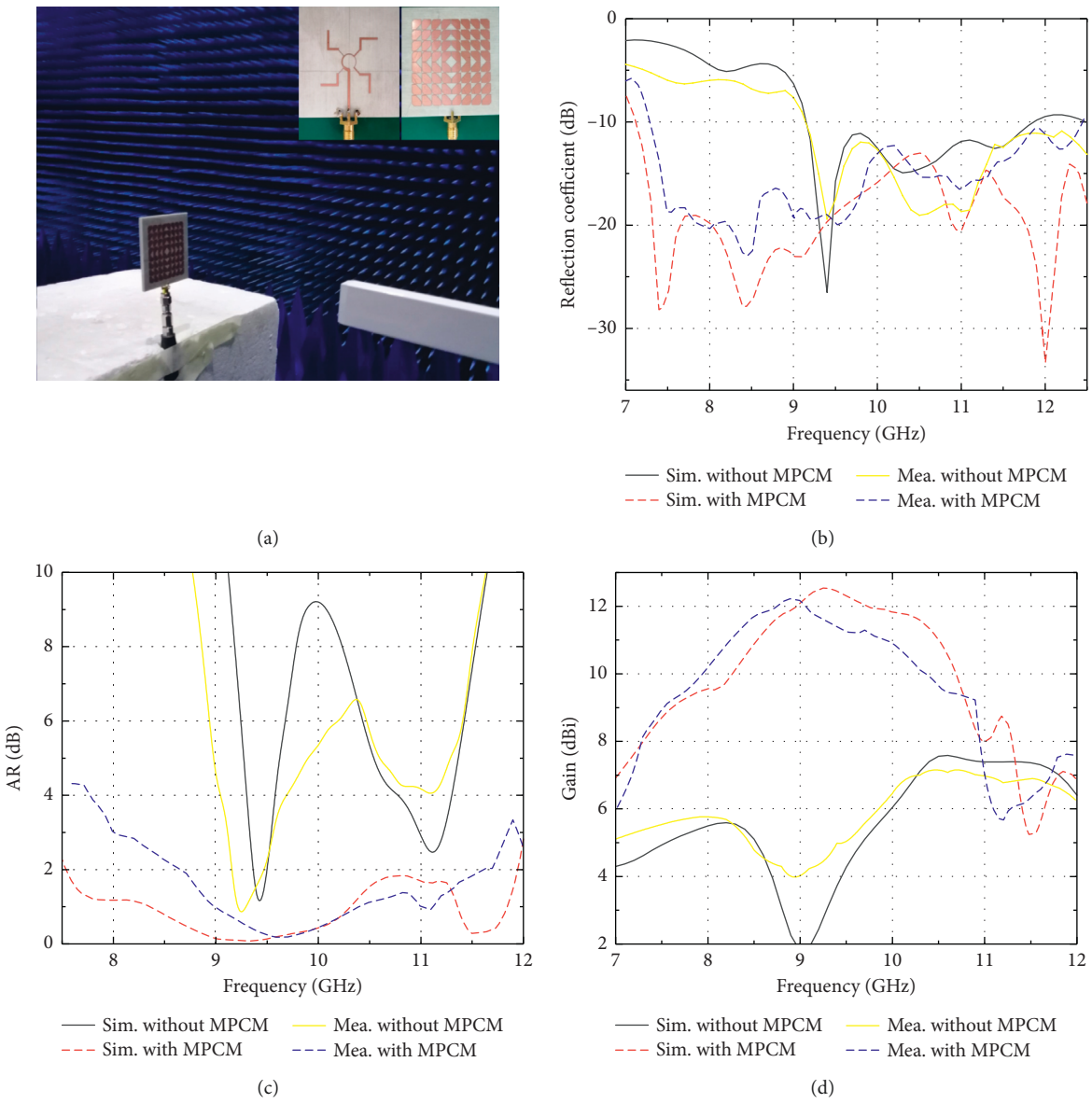

Figure 7: (a) The photograph of fabricated and measured. Simulated and measured (b) reflection coefficients, (c) AR, and (d) gain versus frequency of both antennas.

2.4. Analysis of RCS Reduction. As shown in Figure 3, the MPCM patch can be regarded as a checkerboard surface that consists of a PCM array and mirror PCM array. A phase difference of 180° is created between each part, so that the reflected waves for each will cancel each other out. Consequently, the total RCS is significantly reduced. In order to study the RCS reduction characteristics of the array antenna, the polarization conversion characteristics of the PCM element need to be studied. When the incident wave impinges along the z-direction, the unit cell can be considered a reflective polarization converter. As shown in Figure 3, using the linear x-polarized normal-impinging wave $\vec{E}^{\mathrm{i}}_x$ as an example, the reflected electric fields $\vec{E}^{\mathrm{r}}_x$ and $\vec{E}^{\mathrm{r}}_y$ along the x-axis and the y-axis are generated. Definitions $r_{xx} = |\vec{E}^{\mathrm{r}}_x / \vec{E}^{\mathrm{i}}_x|$ (copolarization) and $r_{yx} = |\vec{E}^{\mathrm{r}}_y / \vec{E}^{\mathrm{i}}_x|$ (cross-polarization) represent the reflection ratio in the x-x and x-y directions, respectively. The polarization conversion ratio (PCR) is defined as PCR $= r^2_{yx} / (r^2_{yx} + r^2_{xx})$, representing the polarization conversion characteristics for the PCM cell. The PCM unit cell has been simulated in the software Ansys HFSS v13.0, using the Floquet port and master/slave boundary conditions. The results presented in Figure 6(a) show that the copolarization of the reflection coefficient loses its dominant position within 8–20 GHz, whereas the cross-polarization becomes the dominant component. The PCR value is greater than 0.7 between 8 and 20 GHz, which means that most of the energy is redirected in the orthogonal direction. Figure 6(b) presents the cross-polarization reflection phase difference between the PCM infinite period unit and its mirror. In the working frequency band, the reflected wave of PCM has the same amplitude as that of the corresponding

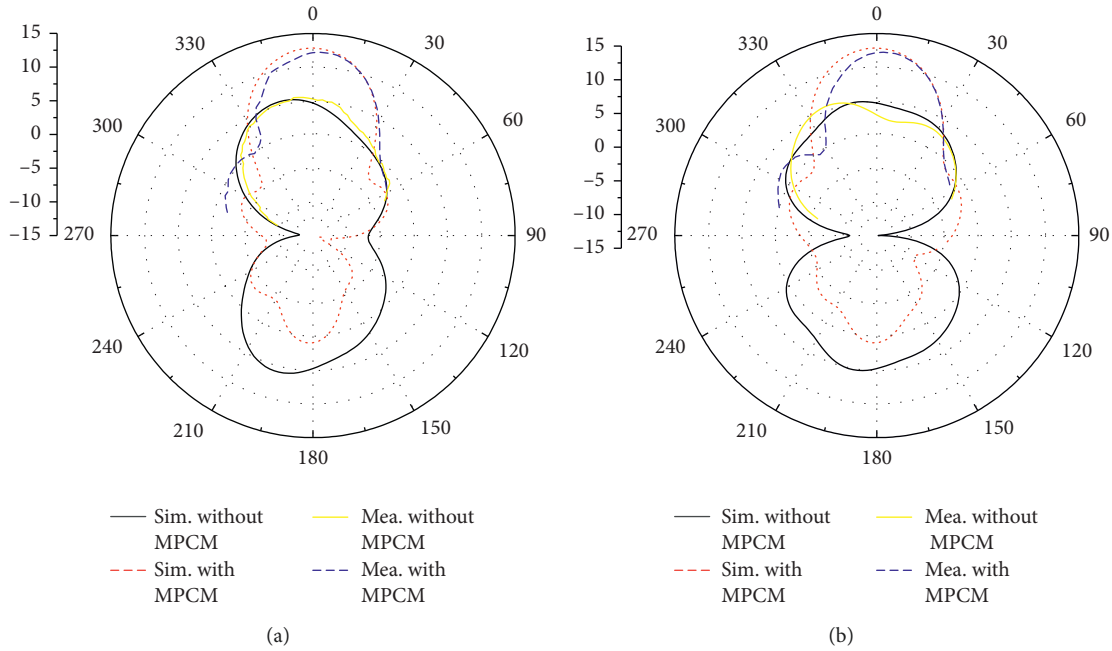

Figure 8: The simulated normalized radiation pattern of both antennas at 10 GHz. (a) *xoz*-plane and (b) *yoz*-plane.

mirror image, with a phase difference of 180°. The reflected waves from each part cancel each other out, decreasing the RCS. Due to the symmetrical structure of the MPCM, the reduction in RCS of the y-polarized incident wave is similar. As a result, the mirror chessboard PCM structure is chosen due to its broadband, low-RCS features.

Considering the arrangement of MPCM, the corresponding slot antennas under each PCM should not be configured such that they are in the same direction, and they should not be excited by the same phase. Therefore, a CP slot array antenna based on a sequential rotational feed network is selected as the source antenna. Because the reference antenna also utilizes circular polarization radiation, it may seem unnecessary to use MPCM for the same purpose. However, antennas using MPCM have a wider AR bandwidth because a superior polarization purity can be obtained by replacing four LP components with four CP components. In addition, gain can be increased at operating frequencies, so the radiation performance and scattering characteristics are balanced by the combination of the arrangement of the MPCM and the radiation source.

3. Simulation and Measurement Comparison of Both Antennas

In order to verify the correctness of simulation and analysis, an array sample with a size of $50 \times 50 \times 2.5\ \text{mm}^2$ was created and measured. The spacing of each slot is 20.7 mm, approximately 0.6 λ_0 (relative to the operating frequency of 10 GHz). The radiation patterns of the antenna are measured in a microwave chamber without reflection, as shown in Figure 7(a). The reflection coefficient of the antenna was measured using an Agilent N5247A vector network analyzer.

Figure 7(b) shows the reflection coefficient results, both with and without the MCPM antenna simulation and measurement. Although there exists some deviation, the overall results are consistent. The measurement and simulation AR bandwidth for the two antennas are shown in Figure 7(c). The measured CP operating bandwidth is 8–12 GHz (40%), whereas the simulated CP operating bandwidth is 7.5–12 GHz (46.1%). The results indicate that the AR bandwidth can be extended by using the MPCM. Figure 7(d) shows the gain versus frequency plot for the simulation and measurement of the antenna. The gain of an antenna with MPCM is higher from 7–11.2 GHz, compared to that of an antenna without MPCM. The measured 3 db gain is in the 7.7–10.5 GHz band (30.7%), whereas the simulated one is in the 7.9–10.8 GHz band (31%). The main cause for the offset in frequency is attributed to both manufacturing error and error in measurement. Figures 8(a) and 8(b) depict the measurement and simulation patterns of the two antennas at 9.3 GHz. The difference between simulation and measurement is due to the measurement environment, manufacturing tolerances, and assembly errors. The test and simulation results in Figures 7 and 8 show good consistency overall, verifying that the use of MPCM improves the radiation performance.

The 3D bistatic scattering field at 10 GHz under normal incidence, both with and without the MPCM antenna, is shown in Figures 9(b) and 9(c). The normal directional energy of the scattered wave is redistributed in four directions $(\varphi, \theta) = (45^\circ, 46^\circ)$, $(135^\circ, 46^\circ)$, $(225^\circ, 46^\circ)$, and $(315^\circ, 46^\circ)$. The frequency response of the measured and simulated monostatic RCS in the x-polarized normal-impinging plane wave can be seen in Figure 9(a). The implemented RCS reduced frequency bandwidth is from 8

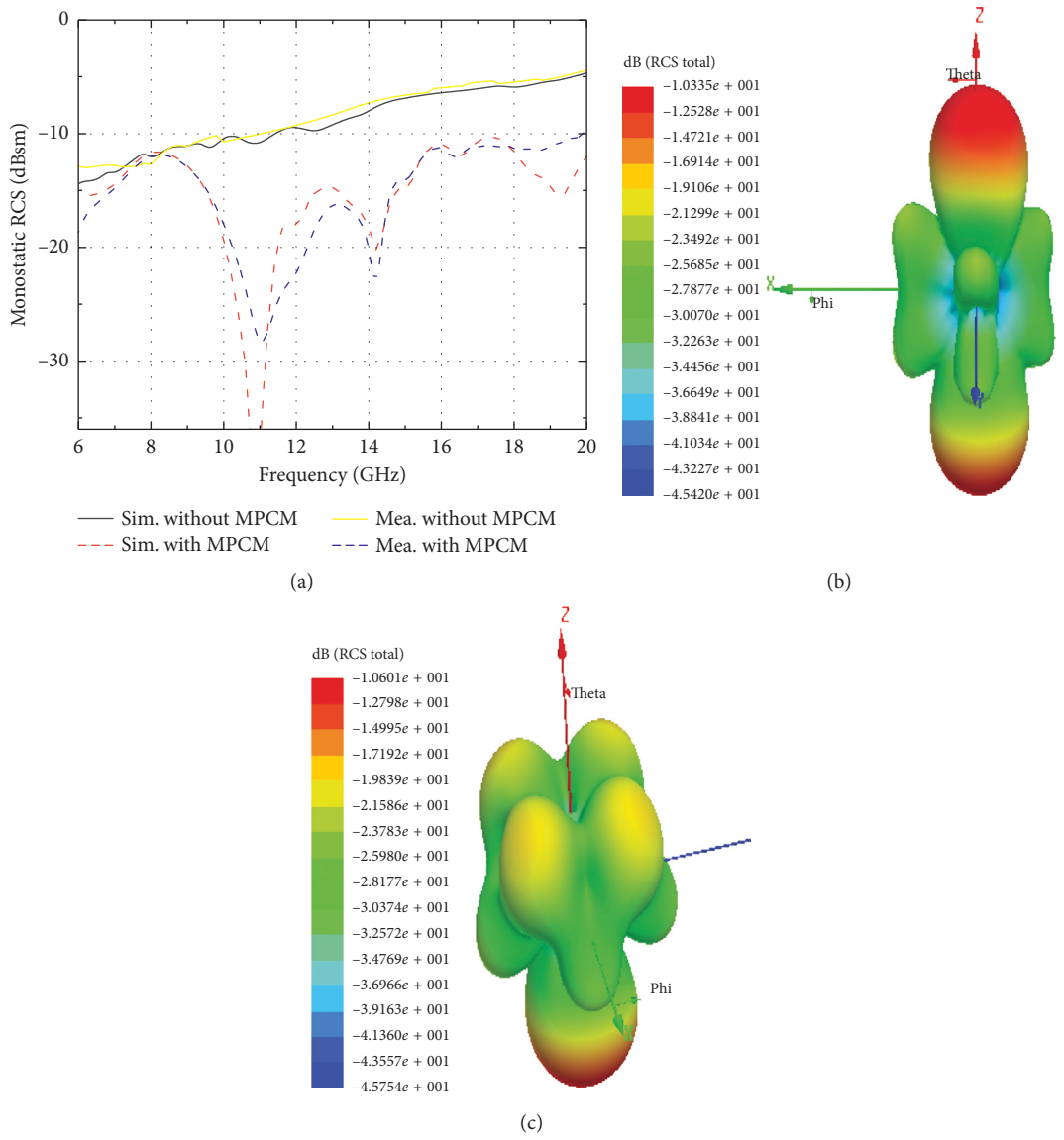

Figure 9: (a) Simulated and measured RCS of both antennas as a function of frequency for normal-impinging plane wave with x-polarization; 3D bistatic scattered field at 10 GHz under normal incidence for (b) antenna with CPCM and (c) antenna without CPCM.

to 20 GHz, and the RCS reduced band is consistent with the frequency band for PCR values greater than 0.7. In addition, the maximum RCS reduction value is at least 14 dB. Since the MPCM structure is symmetrical, the same effect is produced by a normal-impinging plane wave with y-polarization. Some differences can be observed between the simulation and the measurement; this occurs primarily because of tolerance during fabrication, measurement deviations, and environmental factors, all affecting the measured RCS results.

4. Conclusions

In this paper, a novel antenna is proposed. It features a broadband CP, high gain, and low RCS using MPCM. The RCS range is between 8 and 20 GHz and is lower than the reference antenna. Furthermore, the gain is increased in the operating bandwidth and the AR bandwidth is also broadened. The simulated and measured results show that there is an improvement in the scattering and radiation characteristics of the MPCM antenna. Therefore, the design presented in this research provides a new approach for implementing broadband CP, high-gain, and low-RCS antennas. This has potential for use in several applications, most notably in stealth platforms.

Data Availability

The data used to support the findings of this study are included within the article.

Conflicts of Interest

The authors declare that there are no conflicts of interest regarding the publication of this paper.

Acknowledgments

This research was partially supported by the Major Project of Provincial Natural Science Research of the University of Anhui Province of China (Grant nos. KJ2018ZD046 and 2017sxzx40), the Science and Technology Project of Anhui Province (Grant no. 1708085QF150), and the National Natural Science Foundation of China (Grant nos. 61801163 and 61871001).

References

[1] Y. Liu, K. Li, Y. Jia, Y. Hao, S. Gong, and Y. J. Guo, "Wideband RCS reduction of a slot array antenna using polarization conversion metasurfaces," *IEEE Transactions on Antennas and Propagation*, vol. 64, no. 1, pp. 326–331, 2016.

[2] L. Zhang and T. Dong, "Low RCS and high-gain CP microstrip antenna using SA-MS," *Electronics Letters*, vol. 53, no. 6, pp. 375-376, 2017.

[3] O. Altintas, E. Unal, O. Akgol, M. Karaaslan, F. Karadag, and C. Sabah, "Design of a wide band metasurface as a linear to circular polarization converter," *Modern Physics Letters B*, vol. 31, no. 30, article 1750274, 2017.

[4] O. Akgol, E. Unal, O. Altintas, M. Karaaslan, F. Karadag, and C. Sabah, "Design of metasurface polarization converter from linearly polarized signal to circularly polarized signal," *Optik*, vol. 161, pp. 12–19, 2018.

[5] O. Akgol, O. Altintas, E. Unal, M. Karaaslan, and F. Karadag, "Linear to left- and right-hand circular polarization conversion by using a metasurface structure," *International Journal of Microwave and Wireless Technologies*, vol. 10, no. 1, pp. 133–138, 2018.

[6] W. Pan, C. Huang, P. Chen, X. Ma, C. Hu, and X. Luo, "A low-RCS and high-gain partially reflecting surface antenna," *IEEE Transactions on Antennas and Propagation*, vol. 62, no. 2, pp. 945–949, 2014.

[7] C. Huang, W. Pan, X. Ma, and X. Luo, "A frequency reconfigurable directive antenna with wideband low-RCS property," *IEEE Transactions on Antennas and Propagation*, vol. 64, no. 3, pp. 1173–1178, 2016.

[8] Y.-j. Zheng, J. Gao, X.-y. Cao, S.-j. Li, and W.-q. Li, "Wideband RCS reduction and gain enhancement microstrip antenna using chessboard configuration superstrate," *Microwave and Optical Technology Letters*, vol. 57, no. 7, pp. 1738–1741, 2015.

[9] J. Hu, G. Q. Luo, and Z.-C. Hao, "A wideband quad-polarization reconfigurable metasurface antenna," *IEEE Access*, vol. 6, pp. 6130–6137, 2018.

[10] K. Li, Y. Liu, Y. Jia, and Y. J. Guo, "A circularly polarized high-gain antenna with low RCS over a wideband using chessboard polarization conversion metasurfaces," *IEEE Transactions on Antennas and Propagation*, vol. 65, no. 8, pp. 4289–4292, 2017.

[11] Y. Zhao, X. Cao, J. Gao, L. Xu, X. Liu, and L. Cong, "Broadband low-RCS circularly polarized array using metasurface-based element," *IEEE Antennas and Wireless Propagation Letters*, vol. 16, pp. 1836–1839, 2017.

[12] J. Han, X. Cao, J. Gao et al., "Broadband radar cross section reduction using dual-circular polarization diffusion metasurface," *IEEE Antennas and Wireless Propagation Letters*, vol. 17, no. 6, pp. 969–973, 2018.

[13] Y. Zhao, X. Cao, J. Gao, X. Yao, and X. Liu, "A low-RCS and high-gain slot antenna using broadband metasurface," *IEEE Antennas and Wireless Propagation Letters*, vol. 15, pp. 290–293, 2016.

[14] J. Wu, Z. Zhang, X. Ren, Z. Huang, and X. Wu, "A broadband electronically mode-reconfigurable orbital angular momentum metasurface antenna," *IEEE Antennas and Wireless Propagation Letters*, vol. 18, no. 7, pp. 1482–1486, 2019.

[15] H. Evans, P. Gale, B. Aljibouri, E. G. Lim, E. Korolkeiwicz, and A. Sambell, "Application of simulated annealing to design of serial feed sequentially rotated 2 X 2 antenna array," *Electronics Letters*, vol. 36, no. 24, pp. 1987-1988, 2000.

[16] K. K. Pang, H. Y. Lo, K. W. Leung, K. M. Luk, and E. K. N. Yung, "Circularly polarized dielectric resonator antenna subarrays," *Microwave and Optical Technology Letters*, vol. 27, no. 6, pp. 377–379, 2000.

[17] H. L. Zhu, S. W. Cheung, X. H. Liu, and T. I. Yuk, "Design of polarization reconfigurable antenna using metasurface," *IEEE Transactions on Antennas and Propagation*, vol. 62, no. 6, pp. 2891–2898, 2014.

[18] C. L. Holloway, E. F. Kuester, J. A. Gordon, J. O'Hara, J. Booth, and D. R. Smith, "An overview of the theory and applications of metasurfaces:The two-dimensional equivalents of metamaterials," *IEEE Antennas and Propagation Magazine*, vol. 54, no. 2, pp. 10–35, 2012.

[19] W. Liu, Z. N. Chen, and X. Qing, "Metamaterial-based low-profile broadband aperture-coupled grid-slotted patch antenna," *IEEE Transactions on Antennas and Propagation*, vol. 63, no. 7, pp. 3325–3329, 2015.

Hindawi
International Journal of Antennas and Propagation
Volume 2019, Article ID 3782528, 10 pages
https://doi.org/10.1155/2019/3782528

Research Article

A Compact 5G Decoupling MIMO Antenna Based on Split-Ring Resonators

Ziyu Xu, Qisheng Zhang, and Linyan Guo

School of Geophysics and Information Technology, China University of Geosciences, Beijing, China

Correspondence should be addressed to Linyan Guo; guoly@cugb.edu.cn

Received 28 February 2019; Revised 18 April 2019; Accepted 28 April 2019; Published 2 June 2019

Guest Editor: Sreedevi Menon

A compact planar multiple-input multiple-output (MIMO) antenna array for 5G band is proposed in this paper. To improve the isolation of compact microstrip antenna array, this paper mainly presents an electromagnetic resonant ring method for MIMO antenna array. The proposed antenna can cover both the 3.3-3.6 GHz and 4.8-5 GHz bands proposed for the 5G band. The antenna proposed in this paper consists of two symmetrical meandered monopole radiators, grid structures, and a Y-shape element. Two different sizes of split-ring resonators (SRRs) are used to suppress the interference of the coupled signal to the antenna system; thereby it can reduce the mutual coupling effect. The experimental results show that the mutual coupling between the two elements is below -25 dB in both of the bands after adding the SRRs. And this antenna is only 23×19 mm^2. Its compact size and structure can be used as a mobile terminal antenna.

1. Introduction

With the rapid development of wireless communication technology, mobile communication has been integrated into all aspects of life. Nowadays, fifth generation is becoming a hot spot in the field of global research because of its faster transmission rate and higher performance [1]. At present, the fifth generation of mobile communications (5G) of the band is identified as two frequency bands in 3.3-3.6 GHz and 4.8-5 GHz. Total of 500 MHz bandwidth of these frequencies can be reached. And in communication systems, multiple-input multiple-output (MIMO) techniques can significantly improve spectrum utilization and channel capacity without increasing transmit power and adding additional transmission bandwidth [2, 3]. However, as the miniaturization and portability of wireless devices become mainstream, the available space for antennas is more limited. Therefore, it is very necessary to design a compact MIMO antenna. In order to adapt to the commonly used wireless devices, printing MIMO antennas is a necessary choice. However, there is strong mutual coupling when the distance between MIMO antenna elements is very close. It is contrary to the desire for higher isolation and lower envelope correlation coefficients. Hence, it is indispensable to reduce the mutual coupling between the antenna elements.

From the existing literatures, the researchers have done a lot of work in reducing coupling and have proposed various solutions. In order to suppress the propagation of surface waves and reduce the coupling, a parasitic branching method [4] can usually be used. There are also many methods for improving the electromagnetic wave propagation in a certain frequency band by using an electromagnetic band gap structure [5, 6]; they can form a frequency band gap and a phase band gap characteristic to improve isolation. Changing the current propagation path to restrain coupling multiple often chooses neutralization line techniques [7, 8]. Besides, it is also common to use a defective ground structure [9–11] as a band-stop filter to achieve decoupling. In addition to the traditional methods, the method of using the special properties of metamaterials to achieve the desired effect is also mentioned in [12–14]. But the above-mentioned methods are having insufficient space on a compact MIMO antenna and are difficult to function. Therefore, this paper proposes to reduce the coupling by using two different sizes of split-ring resonators (SRRs).

This paper presents a compact binary array printed MIMO antenna. The antenna can cover the 5G band recently proposed by the Ministry of Industry and Information Technology of China. The proposed antenna has a symmetrical structure. And it uses microstrip feed line. In this paper,

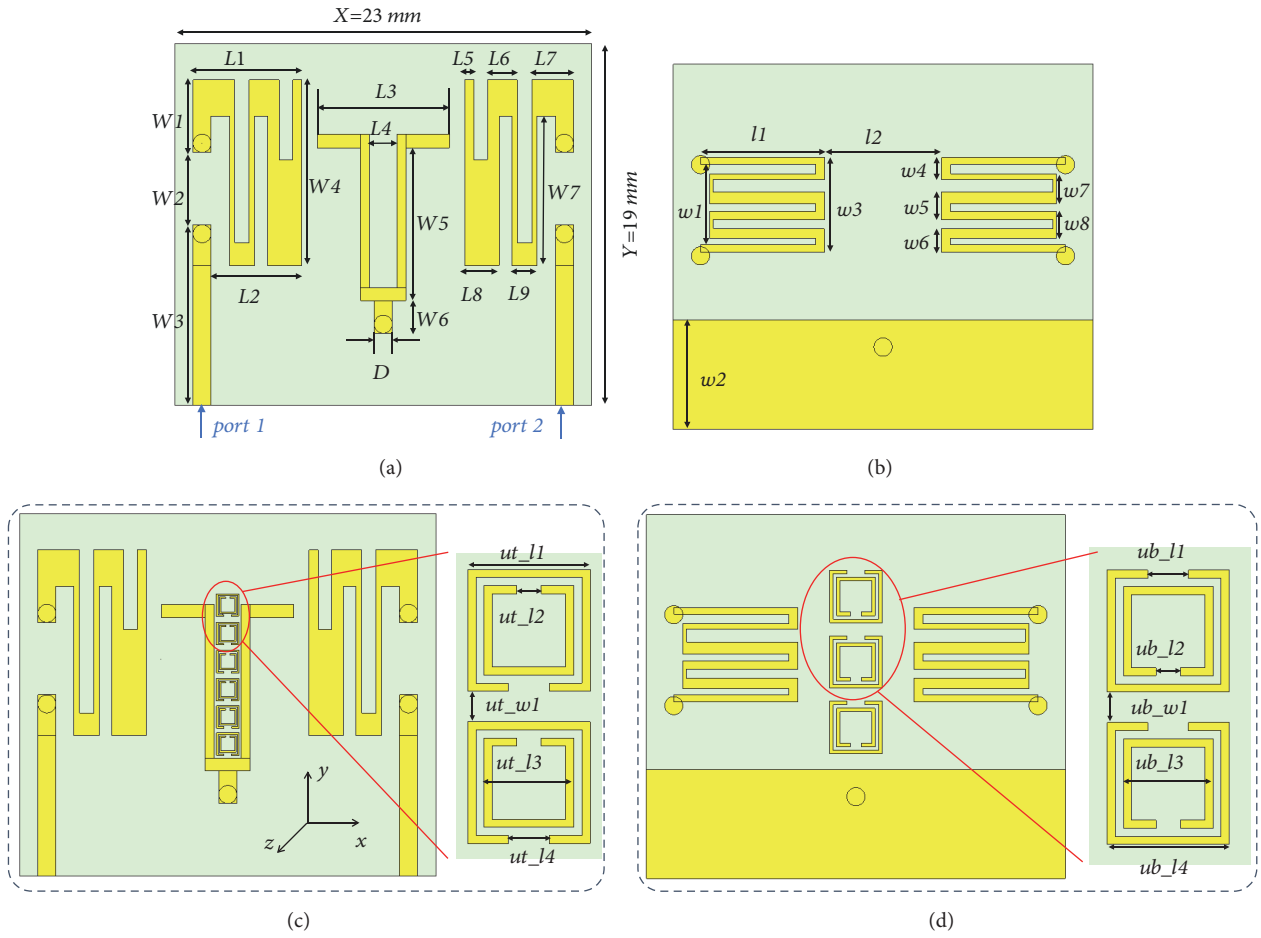

FIGURE 1: (a) The top of the antenna without SRRs. (b) The bottom of the antenna without SRRs. (c) The top of the antenna with SRRs. (d) The bottom of the antenna with SRRs.

electromagnetic waves resonate when they arrive at the SRRs, thereby effectively impeding the propagation of the electromagnetic wave and reducing the mutual coupling between the two antenna elements. The second part introduces the specific structure and size of the antenna. The third part gives the detail of simulated and measured results of the antenna. At the same time, the performance of the antenna and decoupling structure are analyzed and discussed in this section. Finally, the proposed MIMO antenna is summarized.

2. Antenna Design

The proposed antenna is printed on the Rogers 4003C substrate of thickness 0.406 mm with a dielectric constant of 3.38 and loss tangent of 0.0027. The size is only 23×19 mm^2, which is considered compact enough. The metal here is a 0.035 mm thickness copper with a conductivity of 5.8 × 10^7 S/m. The simulated model of the proposed MIMO antenna is shown in Figure 1. This antenna uses the microstrip feed line method. It can be seen from the front view (shows in the Figure 1(a)) that the proposed MIMO antenna is consisted of two monopole radiators and a Y-shape connected to the ground through metal via hole. And the bottom of the antenna constitutes ground and two meandered lines strips connected to the respective radiators, which are connected to the radiators through metal via holes as shown in the Figure 1(b).

In the MIMO antenna model proposed in this paper, the resonant frequency and the resonant intensity are mainly determined by the parameters of each structure. Different structures and shapes can form different electrical lengths, resulting in different resonant frequencies. The right side of the monopole radiation element at the top of the dielectric slab and the corresponding bend line at the back mainly affect the frequency of 4.9 GHz. The length of the short side of the Y-shaped structure plays a major role at the resonant frequency of 3.52 GHz. By analyzing the structure that affects the resonant frequency, the size of the structure can be adjusted to achieve the change of the resonant frequency.

Although the coverage of the required frequency band can be achieved, the antenna distance is very close, only $0.18\lambda_{5G}$; the two array elements have highly coupled. It is a common problem in MIMO applications. Therefore, in order to reduce the mutual coupling between the antenna elements and improve the isolation, the decoupling structures shown in Figures 1(c) and 1(d) are added. Figure 1(c) illustrates that six smaller SRRs are added to the front of the antenna. In Figure 1(d), three larger SRRs are added to the bottom

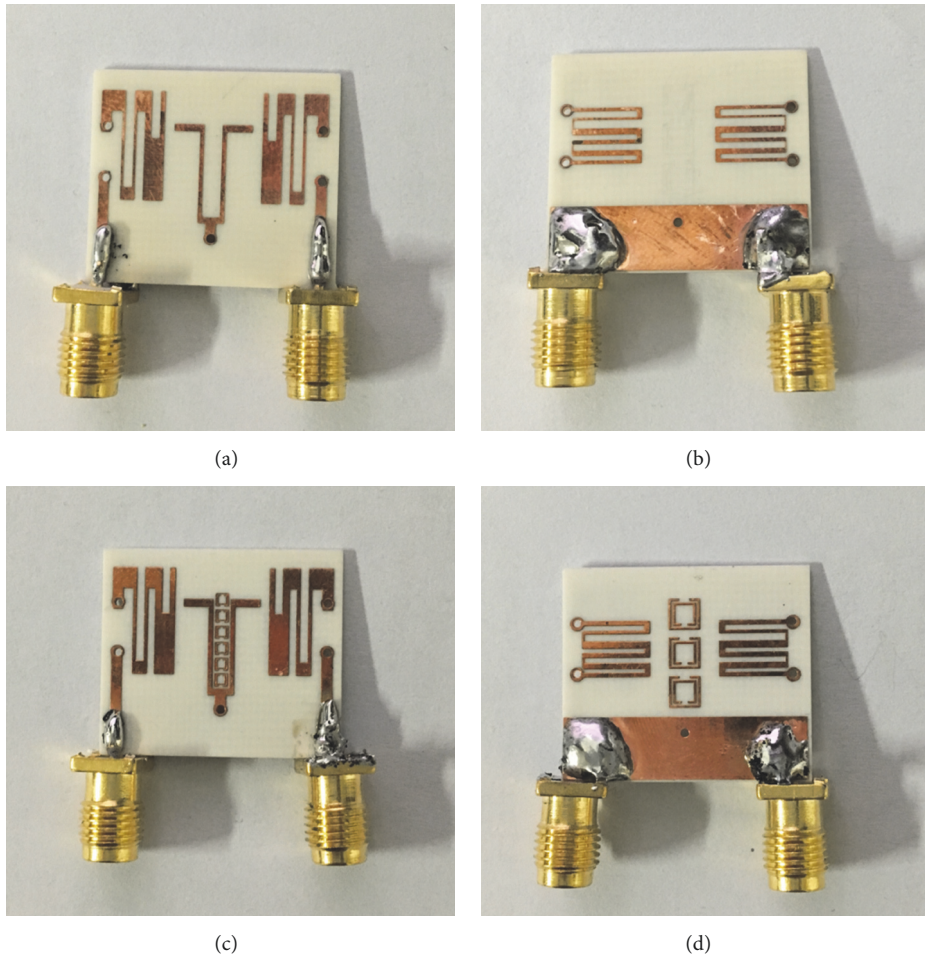

Figure 2: Fabricated prototype of the MIMO antennas. (a) The top of original antenna, (b) the bottom of original antenna, (c) the top of the decoupling antenna, and (d) the bottom of the decoupling antenna.

of the antenna. Considering several situations, we finally chose to place SRRs on both sides. The combination of these decoupling structures can well restrain the mutual coupling at the bands of 3.52 GHz and 4.9 GHz.

The specific size and distance of each structure are finally determined by electromagnetic simulation software CST Microwave Studio, as shown in Table 1. In order to have a good impedance matching with a 50-Ω standard SMA connector, the width of the feed line is designed to be 1 mm.

3. Simulation and Experimental Results

In this section, we will discuss the antennas' simulated and measured results. To verify the simulation, a prototype of the proposed antenna is constructed and measured based on the design and dimensions thereof described in Figure 1. Due to limitations of the manufacture technology, the metal via hole embedded into the dielectric are fabricated as electroplated with a channel diameter of 0.05 mm. The experimental test in this paper uses a vector network analyzer (Agilent E8362B). In experimental measurements, the proposed MIMO antenna is fabricated on a 0.406 mm thick Rogers 4003C substrate. The deposited copper thickness was 0.035 mm. The photograph of the fabricated antenna prototype is shown in Figure 2. The top and the bottom of original antenna are given in Figures 2(a) and 2(b), and Figures 2(c) and 2(d) show the top and bottom of decoupling antenna, respectively. It can be intuitively seen that this MIMO antenna is compact from the fabricated antenna.

3.1. S-Parameters. The simulated and measured S-parameters of the proposed MIMO antenna are sketched in Figures 3(a) and 3(b), respectively. During the test, the two ports of the antenna are, respectively, connected to the two ports of the vector network analyzer Agilent E8362B. Comparing Figures 3(a) and 3(b); the overall trend of the measured results is consistent with the simulated results, but there is a slight deviation. That is, the resonance points obtained by the test are all biased to the high frequency. It may be due to the frequency limit of the SMA connectors and the printed circuit board manufacture tolerance.

It can be noted from the S-parameters shown in Figure 3 that the proposed antenna has a good effect in the above-mentioned frequency bands. Each antenna can cover two frequency bands of 5G, and its return loss S11 can basically reach below -10 dB. With the addition of SRRs, the isolation

Table 1: The specific parameters of MIMO antenna.

parameters	mm	parameters	mm	parameters	mm
L1	6	*W5*	8.45	*w8*	1.5
L2	5	*W6*	2.5	*ut_l1*	1.244
L3	7.3	*W7*	8.25	*ut_l2*	0.249
L4	1.5	*D*	1	*ut_l3*	0.912
L5	0.5	*l1*	6.8	*ut_l4*	0.415
L6	1.65	*l2*	6.4	*ut_w1*	0.311
L7	2.3	*w1*	4.8	*ub_l1*	0.96
L8	1.9	*w2*	6	*ub_l2*	0.576
L9	1.4	*w3*	5.2	*ub_l3*	2.112
W1	4	*w4*	1.2	*ub_l4*	2.88
W2	4	*w5*	1.5	*ub_w1*	0.72
W3	10	*w6*	1.3		
W4	10.25	*w7*	1.65		

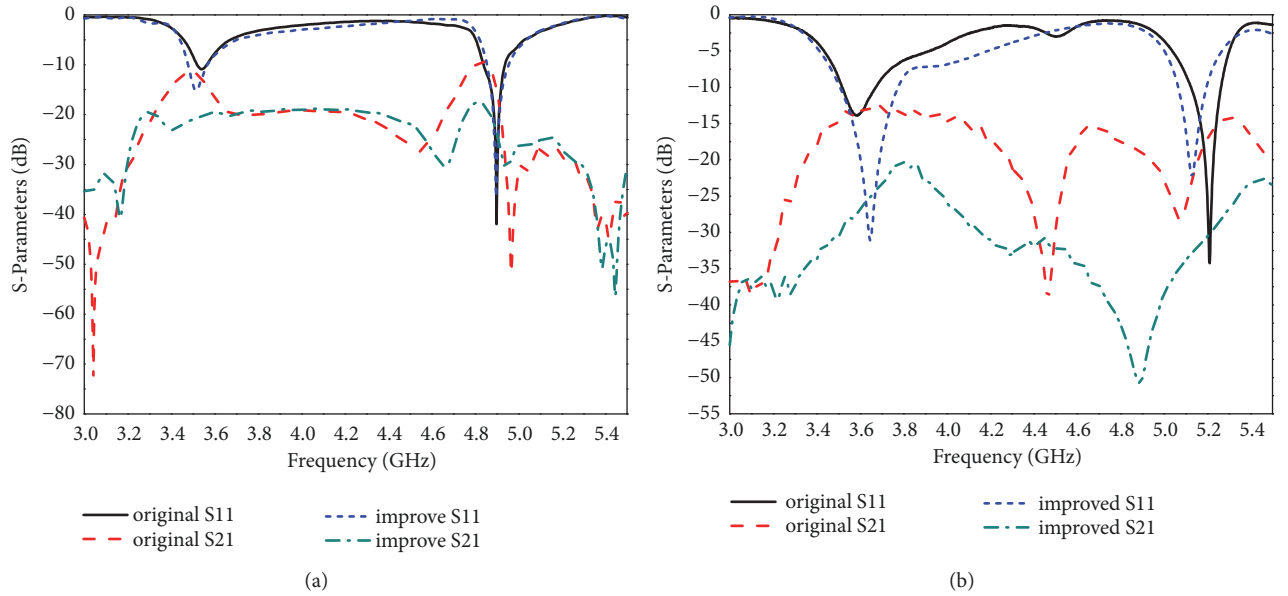

Figure 3: (a) Simulated S-parameters. (b) Measured S-parameters.

of all corresponding bands is better than 25 dB, improving about 10 dB. At the same time, the resonant frequency of the antenna is substantially not offset. The return loss at 3.52 GHz is also slightly better than the original antenna. It can be noticed from the return loss and isolation that the MIMO antenna proposed in this paper performs well. In the measured results, the centre frequency is slightly shifted to the high frequency due to factors such as dielectric plate loss and test feeder loss. There are some errors between the measured results and the simulated results. This may be the reason for the compact size of the antenna and the workmanship is imprecise. However, after adding the SRRs, the overall performance of the antenna is better than the original one.

The original antenna we designed in this paper has a Y-shape structure in the middle of the two radiation elements. The Y-shape structure in this design mainly serves to enhance the radiation effect of the resonant point. When there is no Y-shape structure, although S21 is lower than S11 at the resonance point, it is apparent that S11 at the resonance frequency is less than -10 dB, as shown in Figure 4. S11 with/without Y-shape structure is plotted in Figure 4(a). And Figure 4(b) shows the curves of S21 with/without Y-shape structure. Comparing the red solid line and the black dash line in Figure 4(a), the resonance of antenna is significantly enhanced in the desired frequency bands after adding the Y-shape structure, and the design requirements are met.

Normally, the ground plane will also participate in the radiation of the antenna, so its size will also affect the S-parameters. Using the control variable method, the other parts remain the same size, only the width of the ground plane is changed (the size of *w2*), as shown in Figure 5. It can be known from the figure that the resonant frequency will shift to the high frequency as the width of the ground plane increases, both in the low frequency and in the high frequency bands. When *w2*=5 mm, the performance of S11 is best in the 3.3-3.6 GHz band, but the S11 in the

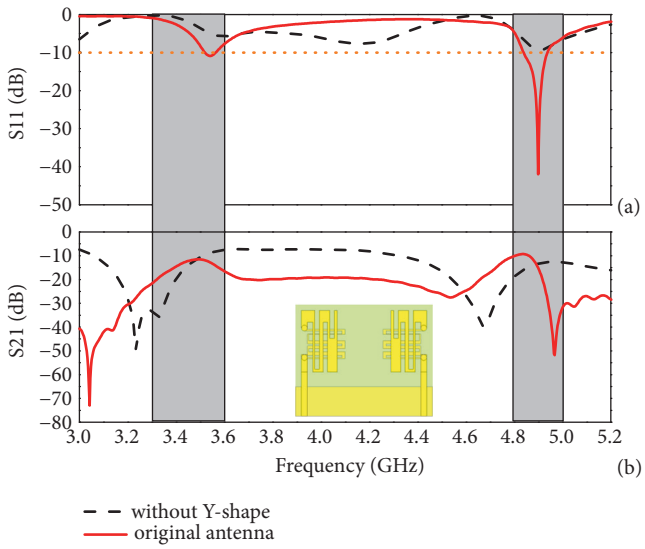

Figure 4: S-parameters with/without Y-shape structure: (a) S11 and (b) S21. Inset: Model of antenna without Y-shape structure.

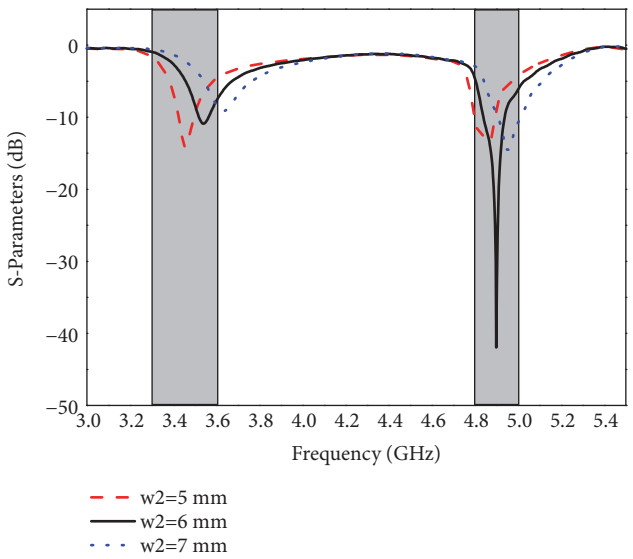

Figure 5: S-parameters of ground plane with different widths.

4.8-5 GHz band is slightly smaller and more biased towards low frequencies. When *w2*=7 mm, it has a slightly higher frequency in the 4.8-5 GHz band and S11 is slightly smaller, but its resonant frequency is already higher than 3.6 GHz in the band of 3.3-3.6 GHz and does not meet the < -10 dB requirement. Therefore, considering the comprehensive consideration, it is finally determined that the width of the ground plane is 6 mm.

Since the SRR can be equivalent to an *LC* series resonant circuit, its resonant frequency can be obtained substantially by $f_0 = 1/2\pi\sqrt{LC}$. L is the full inductance of the SRR. When calculating the SRR's inductance, it can be equivalent to a full-closed loop inductance. The split of the two rings can be equivalent to the capacitance C, which is the full capacitance of the SRR. The initial size of the SRR is obtained

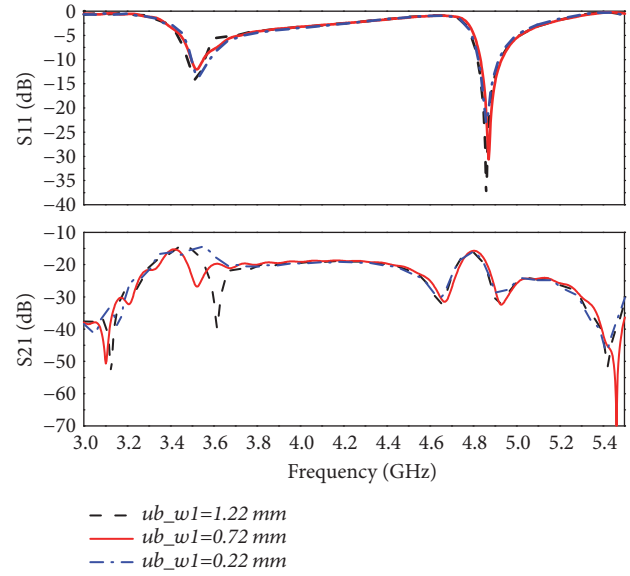

Figure 6: S-parameters of different distance between larger SRRs.

according to the formula mention above and then optimized by using CST Microwave Studio to obtain the final size. Take the distance between the larger SRRs on the bottom of antenna (the size of *ub_w1*) as an example for discussion. The S-parameter when *ub_w1* is changed can be seen from Figure 6. The change of *ub_w1* has little effect on S11, but it has a significant impact on S21. When *ub_w1*=1.22 mm, the frequency of coupling reduction at 3.52 GHz shifts to higher frequency. When *ub_w1*=0.22 mm, the decoupling effect is not significant at 3.52 GHz. Therefore, *ub_w1*=0.72 mm is the most ideal choice.

3.2. Radiation Patterns. To further validate the influence of the SRRs in the MIMO antenna, simulated and measured radiation patterns are plotted in Figures 7 and 8, respectively. Due to the symmetry of the antenna design, the antenna pattern shows good complementarity and orthogonality (the antenna's maximum radiating area is complementary and the main lobe is orthogonal). Therefore, only given the case when port 1 is fed, and port 2 is symmetric with it, the E planes (*yOz*) and H planes (*xOz*) at the two resonance points when port 1 is excited are shown in the figures. Among these, Figures 7(a) and 7(b) show the simulated E planes and H planes at 3.52 GHz. Figures 8(a) and 8(b) are the measured results at 3.52 GHz. And the E planes of the simulated and measured at 4.9 GHz are drawn in Figures 7(c) and 8(c). Figures 7(d) and 8(d) describe the simulated and measured results of the H plane at 4.9 GHz. In these figures, original antenna is drawn with black solid lines, and the improved antenna is drawn with red dashed lines. During the measurement, one port is excited and the other port is connected to the 50-Ω load. From the given results, the radiation omnidirectionality of the antenna is well. The observed radiation patterns show a good agreement with the simulated results and the measured results. Some differences here are possibly due to the factor that the test environment is nonanechoic chamber. It is evident from the

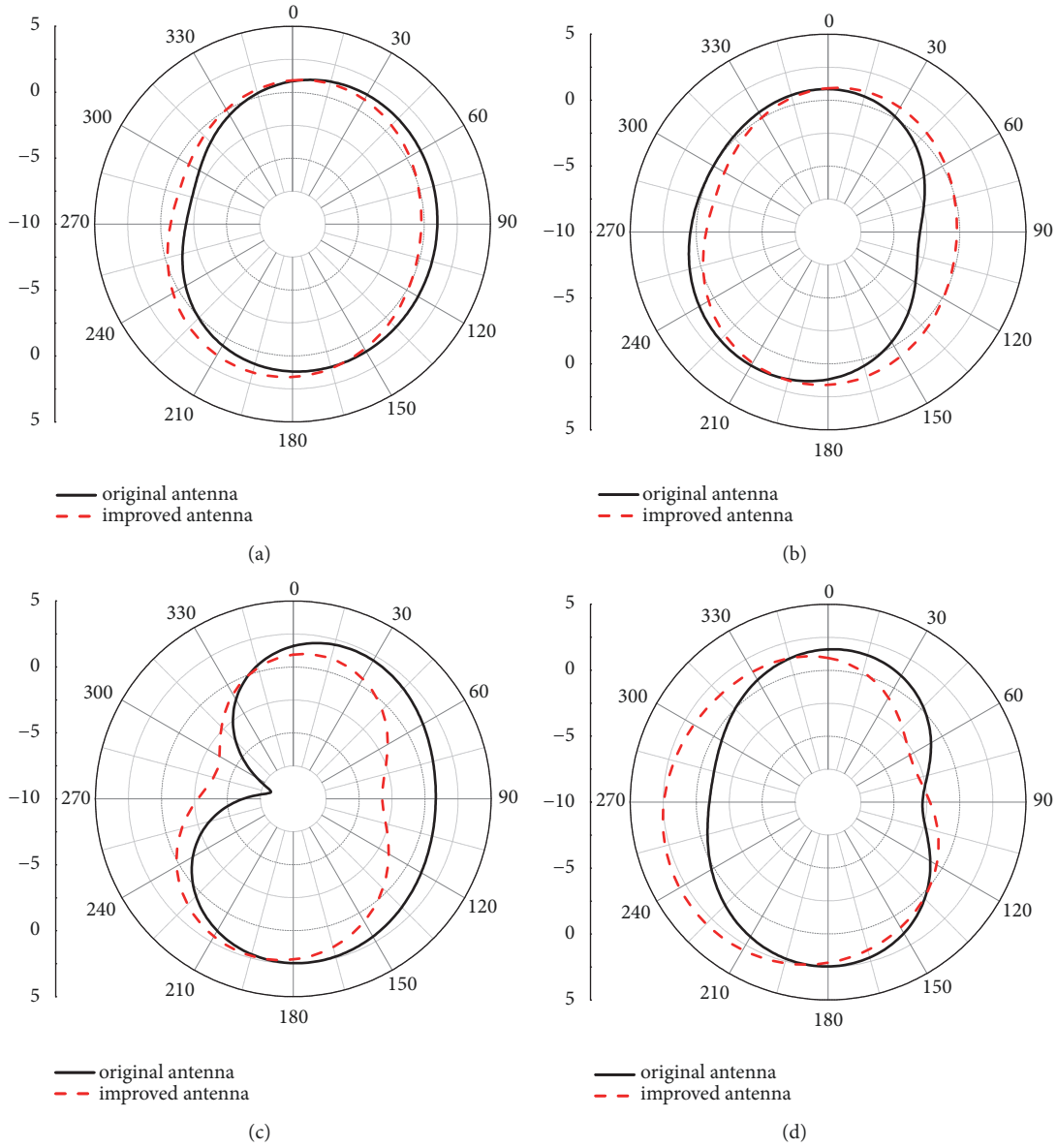

Figure 7: Simulated radiation pattern. (a) E plane and (b) H plane at 3.52 GHz; (c) E plane and (d) H plane at 4.9 GHz.

figures that loading the SRRs has little notable effect on radiation performance of the antenna. A slight inconsistency did not worsen the radiation performance of the antenna. The overall radiation performances of the antenna, such as gain and efficiency, are consistent with the original one.

3.3. Surface Current. In order to study the mutual coupling between the two antenna elements more intuitively and analyze the working mechanism of the SRRs at great length, the simulated results of CST are used to observe the surface current distribution of the antenna. Through these results, the influence of the SRRs on the MIMO antenna is discussed. In this paper, the decoupling structure is mainly composed of two different sizes of SRRs on the front and back sides. The surface current distribution of the antenna with or without SRRs at the excitation of port 1 at 3.52 GHz and 4.9 GHz is displayed in Figure 9. By comparing Figures 9(a) and 9(b), it can be seen that after SRRs are added, most of the current is concentrated to the SRRs on the back side, so that less current can reach the side of port 2, thus effectively reducing the mutual coupling. From the comparison of Figures 9(c) and 9(d), it can be concluded that the original antenna is without SRRs; the current can flow unimpeded to the side of port 2, and thus it has a high coupling. After loading the SRRs; the current propagation is limited, and the port 2 and the radiation of the right side cannot be reached directly, so the mutual coupling is suppressed. Therefore, introducing SRRs can reduce the coupling current of the nonexcited antenna elements. This is because when the coupling current passes through the metal resonant ring, it can effectively restrain the current radiated to the nonexcited antenna element, thereby improving the mutual coupling. For achieving the optimal decoupling effect, the size and position of the SRRs are determined through multiple simulations and optimizations.

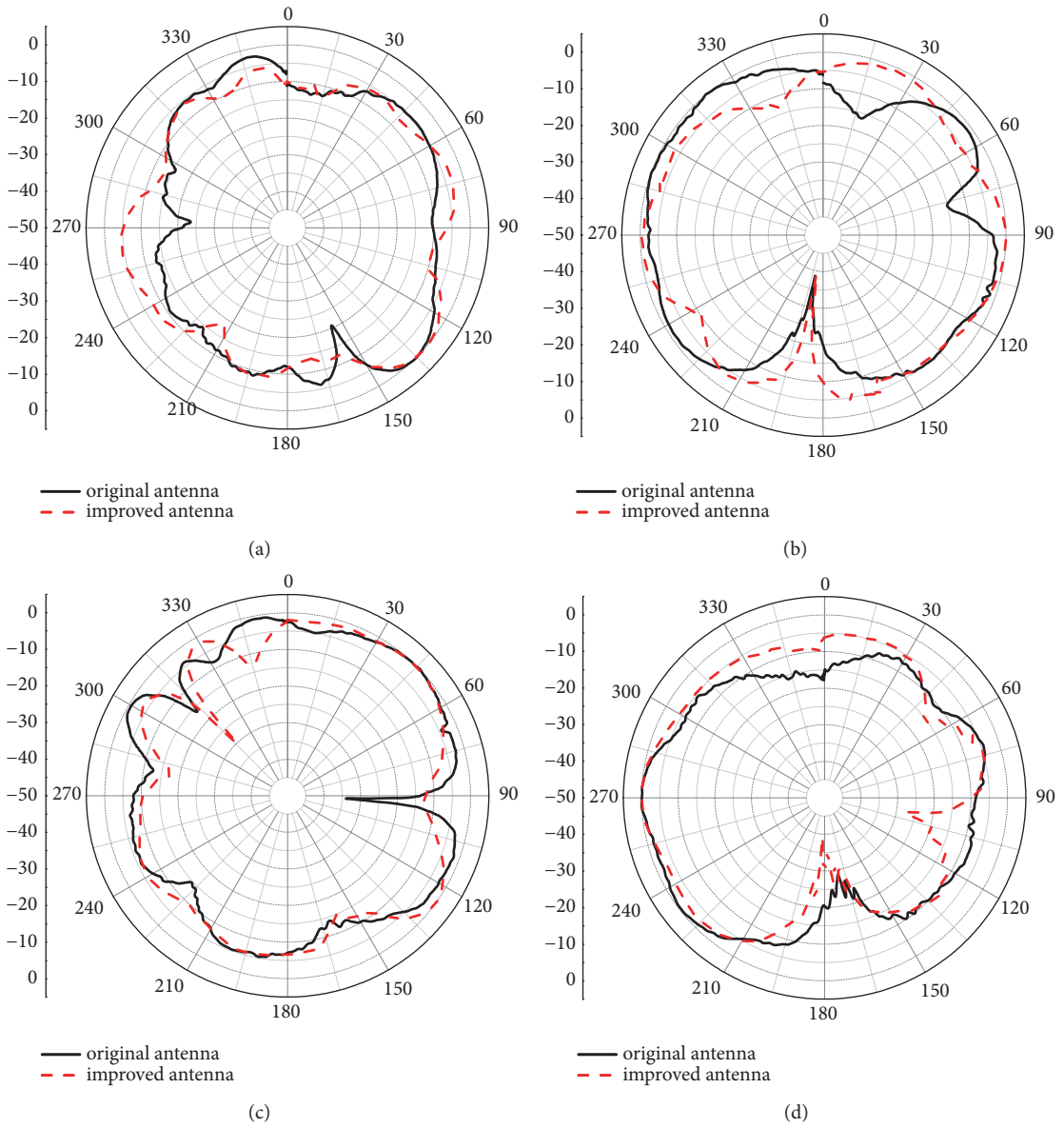

Figure 8: Measured radiation pattern. (a) E plane and (b) H plane at 3.52 GHz; (c) E plane and (d) H plane at 4.9 GHz.

From the simulated results and the measured results, the proposed decoupling structure has a good effect, which provides a thought for MIMO antenna decoupling and has a certain prospect.

3.4. ECC. The envelop correlation coefficient (ECC) is an important figure of merit for any MIMO enabled antenna systems. It can be calculated from the S-parameters of the antenna [15], as formula (1). In formula (1), S_{11}^* and S_{21}^* represent the conjugates of S11 and S21, respectively. The calculated ECC less than 0.5 is the most basic requirement for MIMO antenna. A comparison of ECC computed from S-parameters for MIMO antenna with and without SRRs is exhibited in Figure 10. It is clear that after adding the SRRs, ECC of the antenna is significantly reduced and is less than 0.3 in the required operating frequency band. That means the antenna with SRRs ensures good diversity performance.

$$\rho = \frac{\left|S_{11}^* S_{12} + S_{21}^* S_{22}\right|^2}{\left(1 - \left(\left|S_{11}\right|^2 + \left|S_{21}\right|^2\right)\right)\left(1 - \left(\left|S_{22}\right|^2 + \left|S_{12}\right|^2\right)\right)} \quad (1)$$

Furthermore, in order to distinguish our results from other existing equivalent antennas, the properties of the geometrical dimensions, the relationship between wavelength and size, type of substrate, the decoupling method, and other properties are compared in Table 2. In Table 2, λ represents the dielectric wavelength at the high frequency resonance point of the antenna. The maximum size of the antenna can be obtained by the relationship between λ and size. It is evidently illustrated from the table that the proposed MIMO antenna

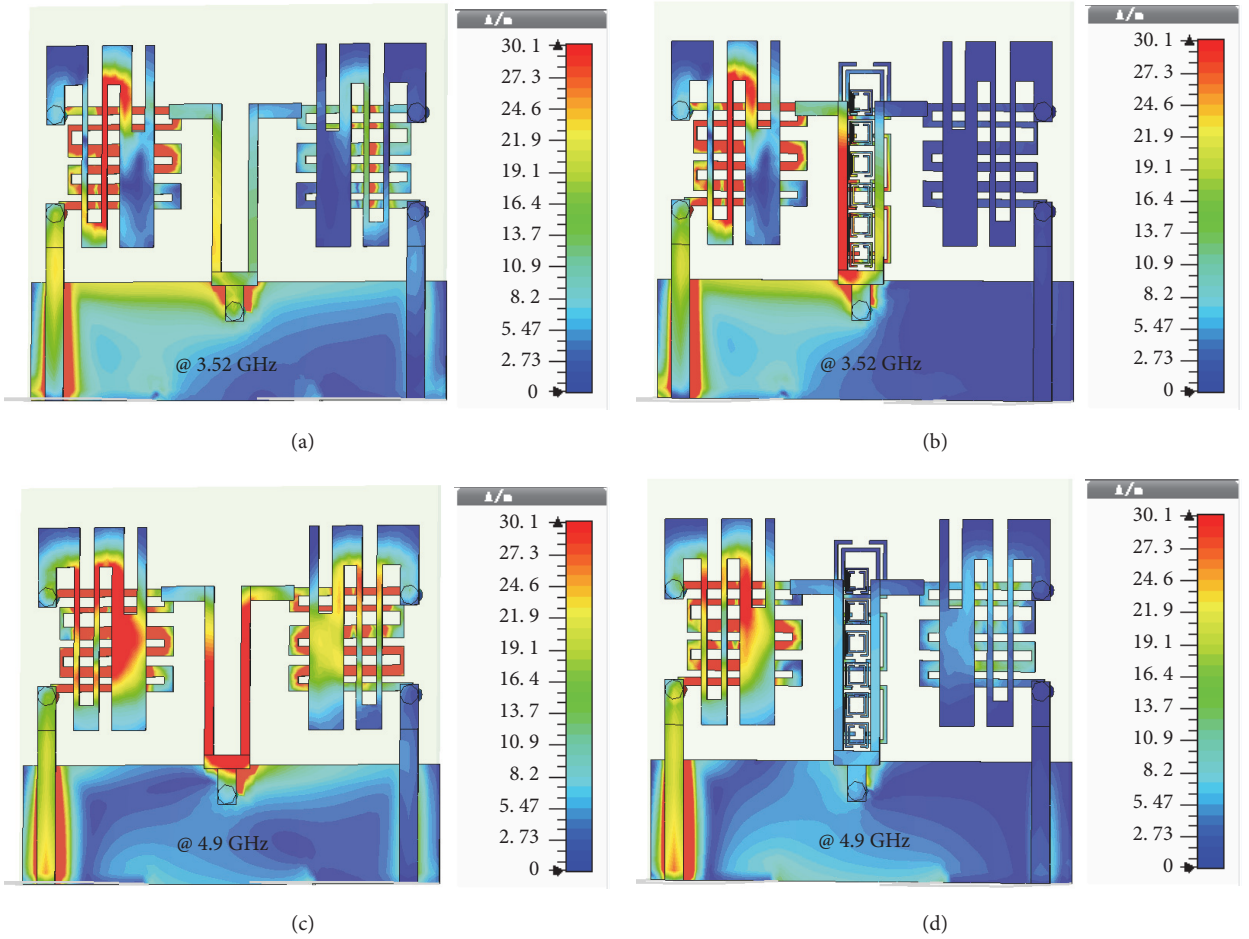

Figure 9: Surface current. (a) Original antenna and (b) improved antenna at 3.52 GHz; (c) original antenna and (d) improved antenna at 4.9 GHz.

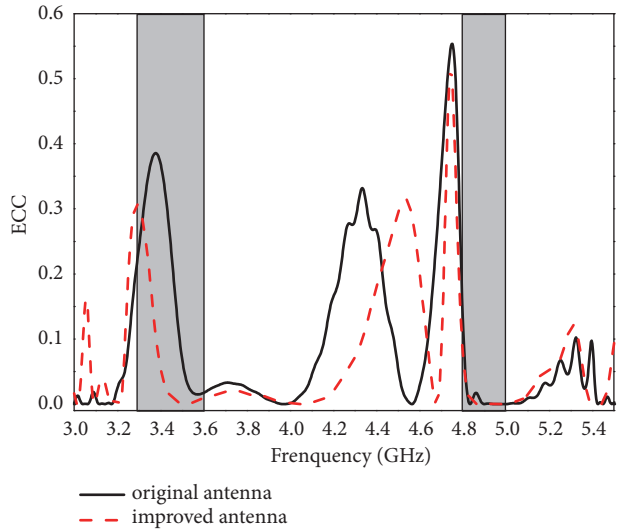

Figure 10: Envelop correlation coefficient.

Table 2: Comparison of proposed antenna and previous equivalent antennas.

	Geometrical dimensions (mm^3)	The relationship between wavelength and size	Type of substrate	Decoupling method	Whether include 5G
[4]	$95 \times 60 \times 0.8$	1.33λ	FR4	Use the parasitic elements	No
[7]	$136 \times 68 \times 1$	4.37λ	FR4	Use the short neutral line	Yes
[11]	$54 \times 30 \times 1.6$	2.18λ	FR4	Use a defected ground structure	No
Proposed antenna	$23 \times 19 \times 0.406$	0.68λ	Rogers 4003C	Use SRRs to prevent electromagnetic wave propagation	Yes

has a more compact size. And it can cover 5G frequency bands very well.

4. Conclusions

A compact 5G MIMO antenna with SRRs has been proposed in this paper. Two-element microstrip MIMO antenna with two different sizes of SRRs is studied. Improvement in the antenna mutual coupling has been achieved using this method. The studied indicate that the mutual coupling in the MIMO antenna loaded by SRRs is suppressed effectively, and the improved MIMO antenna has a better performance. The simulated and measured results show a well agreement. It verifies the good performance of the MIMO antenna. The isolation between the antenna elements is better than -25 dB over all required frequency bands. This simple, compact, low-cost design makes it suitable for applications such as mobile phone terminals for the fifth generation of mobile communications.

Data Availability

The dimension parameters of proposed structure data used to support the findings of this study are included in the article. The dimension parameters of the proposed structure are presented in Figure 1 and Table 1.

Conflicts of Interest

The authors declare that they have no conflicts of interest.

Acknowledgments

This work was supported by the National Natural Science Foundation of China (no. 41704176, 41574131), the National Key Research and Development Program of China (no. 2017YFF0105704), and the Fundamental Research Funds for the Central Universities from China.

References

[1] I. B. Magdău et al., "Five disruptive technology directions for 5G," *Applied Physics Letters*, vol. 12, no. 7, pp. 87–94, 2015.

[2] G. J. Foschini and M. J. Gans, "On limits of wireless communications in a fading environment when using multiple antennas," *Wireless Personal Communications*, vol. 6, no. 3, pp. 311–335, 1998.

[3] B. N. Getu and J. B. Andersen, "The MIMO cube - A compact MIMO antenna," *IEEE Transactions on Wireless Communications*, vol. 4, no. 3, pp. 1136–1141, 2005.

[4] Z. Li, Z. Du, M. Takahashi, K. Saito, and K. Ito, "Reducing mutual coupling of MIMO antennas with parasitic elements for mobile terminals," *IEEE Transactions on Antennas and Propagation*, vol. 60, no. 2, pp. 473–481, 2012.

[5] X. Yang, Y. Liu, Y.-X. Xu, and S.-X. Gong, "Isolation enhancement in patch antenna array with fractal UC-EBG structure and cross slot," *IEEE Antennas and Wireless Propagation Letters*, vol. 16, no. 99, pp. 2175–2178, 2017.

[6] V. Ionescu, M. Hnatiuc, and A. Topală, "Optimal design of mushroom-like EBG structures for antenna mutual coupling reduction in 2.4 GHz ISM band," in *Proceedings of the 5th IEEE International Conference on E-Health and Bioengineering, EHB 2015*, Iasi, Romania, November 2015.

[7] X. Shi, M. Zhang, S. Xu, D. Liu, H. Wen, and J. Wang, "Dual-band 8-element MIMO antenna with short neutral line for 5G mobile handset," in *Proceedings of the 2017 11th European Conference on Antennas and Propagation (EUCAP)*, pp. 3140–3142, Paris, France, March 2017.

[8] S. Zhang and G. F. Pedersen, "Mutual coupling reduction for UWB MIMO antennas with a wideband neutralization line," *IEEE Antennas and Wireless Propagation Letters*, vol. 15, pp. 166–169, 2016.

[9] A. Habashi, J. Nourinia, and C. Ghobadi, "A rectangular defected ground structure (DGS) for reduction of mutual coupling between closely-spaced microstrip antennas," in *Proceedings of the 20th Iranian Conference on Electrical Engineering (ICEE '12)*, pp. 1347–1350, IEEE, Tehran, Iran, May 2012.

[10] M. I. Ahmed, A. Sebak, E. A. Abdallah, and H. Elhennawy, "Mutual coupling reduction using defected ground structure (DGS) for array applications," in *Proceedings of the 15th International Symposium on Antenna Technology and Applied Electromagnetics (ANTEM '12)*, pp. 1–5, IEEE, Toulouse, France, June 2012.

[11] A. A. Ibrahim, M. A. Abdalla, A. B. Abdel-Rahman, and H. F. A. Hamed, "Compact MIMO antenna with optimized mutual coupling reduction using DGS," *International Journal of Microwave and Wireless Technologies*, vol. 6, no. 2, pp. 173–180, 2014.

[12] M. Farahani, J. Pourahmadazar, M. Akbari, M. Nedil, A. R. Sebak, and T. A. Denidni, "Mutual coupling reduction in millimeter-wave MIMO antenna array using a metamaterial polarization-rotator wall," *IEEE Antennas and Wireless Propagation Letters*, vol. 16, pp. 2324–2327, 2017.

[13] Q. Zhang, Y. Jin, J. Feng, X. Lv, and L. Si, "Mutual coupling reduction of microstrip antenna array using metamaterial absorber," in *Proceedings of the 2015 IEEE MTT-S International Microwave Workshop Series on Advanced Materials and Processes for RF and THz Applications (IMWS-AMP)*, pp. 1–3, Suzhou, China, July 2015.

[14] I. Gil and R. Fernandez-Garcia, "Study of metamaterial resonators for decoupling of a MIMO-PIFA system," in *Proceedings of the 2016 International Symposium on Electromagnetic Compatibility, EMC EUROPE*, pp. 552–556, Wroclaw, Poland, September 2016.

[15] S. Blanch, J. Romeu, and I. Corbella, "Exact representation of antenna system diversity performance from input parameter description," *Frequenz*, vol. 39, no. 9, pp. 705–707, 2003.

Hindawi
International Journal of Antennas and Propagation
Volume 2019, Article ID 7508705, 11 pages
https://doi.org/10.1155/2019/7508705

Research Article

Design of a Novel Triple Band Monopole Antenna for WLAN/WiMAX MIMO Applications in the Laptop Computer

Jayshri Kulkarni,[1] **Raju Seenivasan**,[1] **V. Abhaikumar**,[1] **and Deepak Ram Prasath Subburaj**[2]

[1]*ECE Department, Thiagarajar College of Engineering, Madurai 625015, India*
[2]*Thiagarajar Telekom Solutions Ltd., Madurai 625015, India*

Correspondence should be addressed to Jayshri Kulkarni; jayah2113@gmail.com

Received 14 January 2019; Accepted 28 April 2019; Published 2 June 2019

Guest Editor: Sreedevi Menon

This paper presents a triple band monopole antenna design with an overall size of 21 × 8 mm^2 for WLAN/WiMAX Multiple Input and Multiple Output (MIMO) applications in the laptop computer. It comprises of three monopole radiating elements, along with two rectangular open-ended tuning stubs. This structure excites 2.4/5.2/5.8 GHz WLAN and 2.3/3.3/5.5 GHz WiMAX bands. The prototype testing of proposed antenna array formed by using the same antenna design shows that, it has measured -10dB impedance bandwidth of 11.86% (2.22-2.50 GHz) in a lower band (f_l), 5% (3.25-3.42 GHz) in medium band (f_m) and 16.84% (5.00-5.92 GHz) in upper band (f_u). The measured gain and radiation efficiency are well above 3.65 dBi and 75%, respectively, throughout the operating bands. Also, the measured isolation between two antennas is better than -20dB and envelope correlation coefficient (ECC) is less than 0.004 across the three bands of interest. This confirms the applicability of the proposed antenna array for MIMO applications in the laptop computer.

1. Introduction

The MIMO technology has aroused interest in WLAN and WiMAX operating systems because of its possible applications, security, high-speed data transmission, and efficient utilization of spectrum. Practically, minimum two antennas occupying smaller area with high isolation are needed in order to get the high-speed signal transmission and reception in the laptop computer. Literature [1–10] reports many promising MIMO antenna array with multiband operations for the laptop computer.

Kin. Lu. Wong et al. have proposed high isolation MIMO antenna array for the laptop computer in [1, 2] and for the tablet computer in [3]. The proposed antennas occupy a large volume of 45 × 14 × 0.8mm^3 [1], 55 × 9 × 0.8mm^3[2] and 45 × 10 × 0.8mm^3[3]. The MIMO antenna composed of a loop structure and a parasitic element is proposed in [4] and has a size of 38 × 7 × 0.8mm^3 along with an additional ground plane of size 38 × 6mm^2 which is connected to the system ground. Also, the impedance bandwidth is measured at -6dB, which is generally not acceptable for wireless application in the laptop computer. The dual band antennas operating at 2.4/5.2/5.8 GHz are reported in [5–7]. The MIMO antenna array in [5] uses a decoupling structure as an isolating element between two antennas for the laptop computer and also occupies a large volume of 54 × 9 × 0.8mm^3. It is also placed at the center of the system ground, which is generally reserved for embedding the digital camera lens. The uniplanar printed antenna in [6] uses protruded ground embedded with a T shaped slot, in order to reduce mutual coupling and has the dimension of 40 × 9 × 0.8mm^3. The meandered isolation technique used in [7] reduces the mutual coupling lower than -20dB and has large dimensions of 45 × 12 × 0.4mm^3. Two identical antennas presented in [8] have a size of 5 × 42 × 0.8mm^3 and use a decoupling inductor, to reduce the mutual coupling in the 2.4GHz band. The use of inductor makes the hardware complex and also increases the power consumption of the antenna. The standalone monopole antenna used for MIMO array without any isolation element operates at 2.4/3.5/5.5 GHz and having dimensions of 12 × 18 × 0.8mm^3 is reported in [9]. The planar inverted-F antenna along

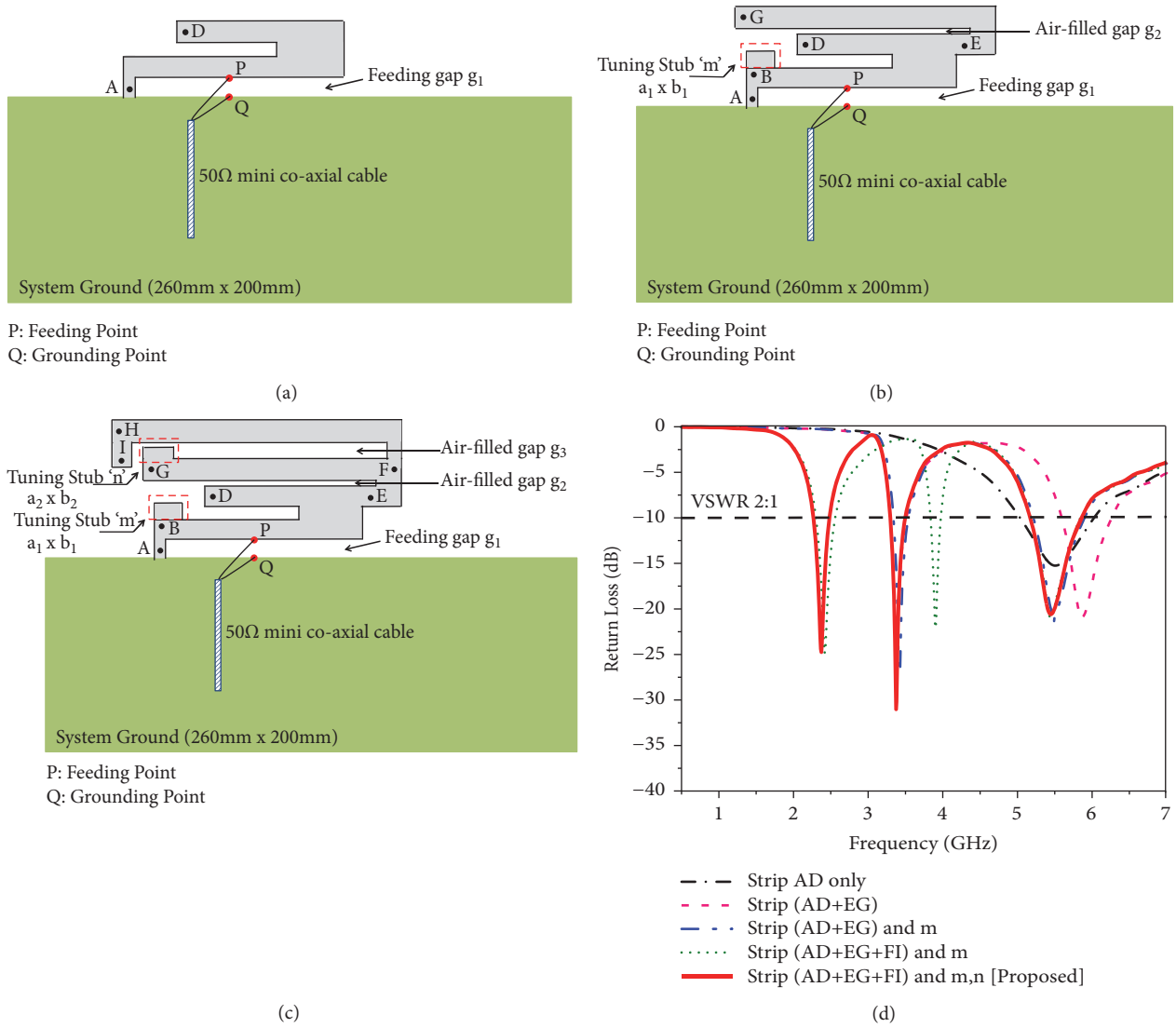

Figure 1: Design and working process of the proposed monopole antenna.

with EBG shape etched on the ground plane for MIMO application in laptop devices is proposed in [10], but has a large dimension of $33.5 \times 22 \times 5.4\text{mm}^3$.

From the above literature, it is understood that the deployment of miniaturized multiple antennas with low coupling coefficient and high RF performance, covering entire wireless bands for MIMO applications in the laptop computer, are posing challenges for researchers and antenna designers.

This paper proposes a triple band monopole antenna design with an overall size of $21 \times 8 \times 0.05$ mm^3 to operate in desired 2.4/5.2/5.8 GHz WLAN and 2.3/3.3/5.5 GHz WiMAX bands for MIMO applications in the laptop computer.

2. Antenna Design

The proposed antenna comprises three monopole radiating elements, namely, strip AD (inverted C), strip EG (inverted J), and strip FI (inverted U), and two rectangular open ended tuning stubs, namely, "m" (a_1xb_1) and "n" (a_2xb_2), as shown in Figure 1. In order to get the resonance at about 5.5GHz of f_u (5.2/5.8 GHz WLAN and 5.5 GHz WiMAX bands), the strip AD is designed in such a way that, its total length is approximately equal to half wavelength long at a resonant mode of 5.5GHz. The strip AD is connected to the system ground at point "A" and introduces feeding gap g_1 as shown in Figure 1(a). With the use of this strip, the proposed antenna successfully generates the desired f_u band as shown in Figure 1(d).

The strip EG is designed to obtain the resonance mode at 3.35 GHz of f_m (3.3-3.4 GHz) band in such a way that its total length is approximately equal to quarter wavelength long at a resonant mode of 3.35 GHz. The strip EG is placed above the strip AD and is connected at point "E". This introduces air-filled gap g_2 as shown in Figure 1(b). With the introduction of this strip, the proposed antenna successfully generates f_m band but shifts the f_u band towards higher frequency due to

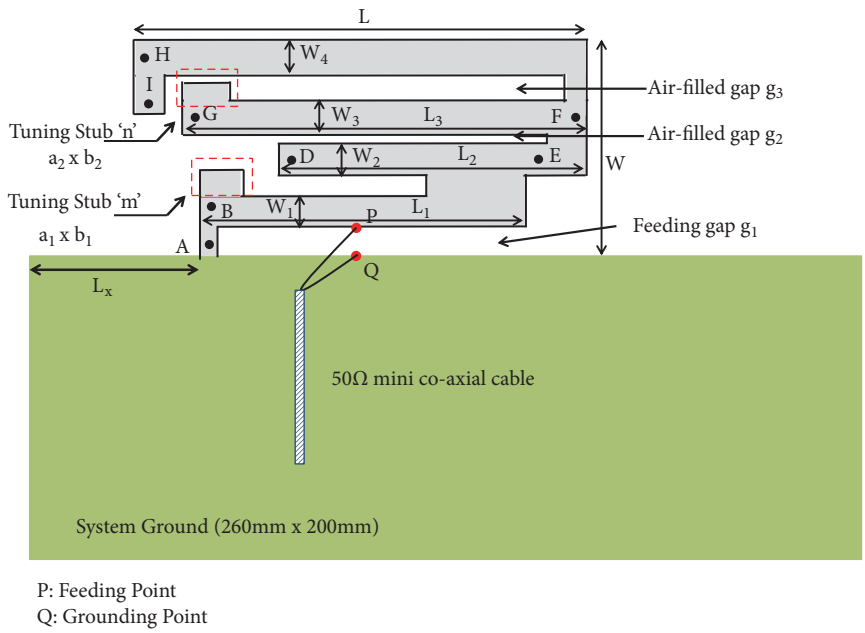

P: Feeding Point
Q: Grounding Point

Figure 2: Complete structure of the proposed antenna.

impedance mismatch as shown in Figure 1(d). In order to tune the f_u for obtaining the required band, a rectangular open ended tuning stub "m" of length (a_1) and height (b_1) is added at point "B" to strip AD as shown in Figure 1(b).

For achieving resonant mode at about 2.4GHz to cover f_l (2.3GHz WiMAX and 2.4GHz WLAN bands), the total length of strip FI is chosen to be quarter wavelength long at the resonant mode of 2.4 GHz. The strip FI is bent at point "H" to form inverted U shape and because of this bending, the required quarter wavelength length of strip FI reduces to 25.5mm only (about 0.2λ).

The strip FI is placed above the strip EG and coupled at point "F" which introduces an air-filled gap g_3 as shown in Figure 1(c). This generates the required f_l band of the proposed antenna, but shifts the f_m band towards the higher frequency, due to more capacitive reactance produced by an air-filled gap g_3 as shown in Figure 1(d). In order to mitigate this increase in capacitive reactance, second rectangular open ended tuning stub "n" of length (a_2) and height (b_2) is added to strip EG as shown in Figure 1(c). This stub tunes the f_m band and also matches the input impedance of the antenna to the impedance of coaxial feed. Here, the desired bandwidth of f_l and f_u bands remain unaffected.

3. Proposed Antenna Geometry

The complete structure of the proposed monopole WLAN/WiMAX antenna for the laptop computer is shown in Figure 2. The copper thickness of monopole radiating elements and tuning stubs used in the proposed antenna is chosen to be 0.05mm. The proposed antenna is placed at a distance of L_x from the left corner on the top edge of the system ground of size 260 × 200mm^2 (supports 13″ laptop display screen) which is made up of 91% brass of thickness 0.2mm. The antenna structure has a length of 21 mm and shows the height of only 8 mm above the system ground. The 8 mm height of the proposed antenna is promising for practical wireless applications in the laptop computer. The proposed monopole antenna is fed by using a 50Ω low loss mini coaxial cable whose central conductor and outer grounding sheath are connected at point P (the feeding point) on the lower edge of strip AD and at point Q (the grounding point) on the upper edge of the system ground. This feeding position makes the effective dielectric constant of all radiating elements equal to 1 and hence, contributes in attaining the desired bands of the proposed antenna [11].

4. Parametric Study of Proposed Antenna

The parametric study of the proposed antenna is carried out to find the optimum value of "m" (a_1xb_1), "n" (a_2xb_2), and L_x, respectively, in the desired f_l, f_m, and f_u bands. The rest of the optimized dimensions of the proposed antenna are as shown in Figure 2.

4.1. Effects of Rectangular Tuning Stub "m" (a_1xb_1) on the Proposed Antenna. The effects of a rectangular open end tuning stub "m" of length (a_1) and height (b_1) on return loss and the input impedance of the proposed antenna over f_u band are studied in Figure 3. From Figure 3(a), it is noted that as the value of a_1 increases from 0 mm to 1.5mm and b_1 increases from 0 mm to 0.9mm, the f_u band shifts towards lower frequency as it attenuates the capacitive reactance produced by air-filled gap g_2. With the aid of Figure 3(b), it is also seen that there is a smooth variation of the input impedance from 68Ω towards 50Ω and reactance is also becoming equal to zero at a resonant mode of 5.5 GHz. For the value of a_1=1.5mm and b_1=0.9mm, the input impedance of the antenna is equal to 50Ω and

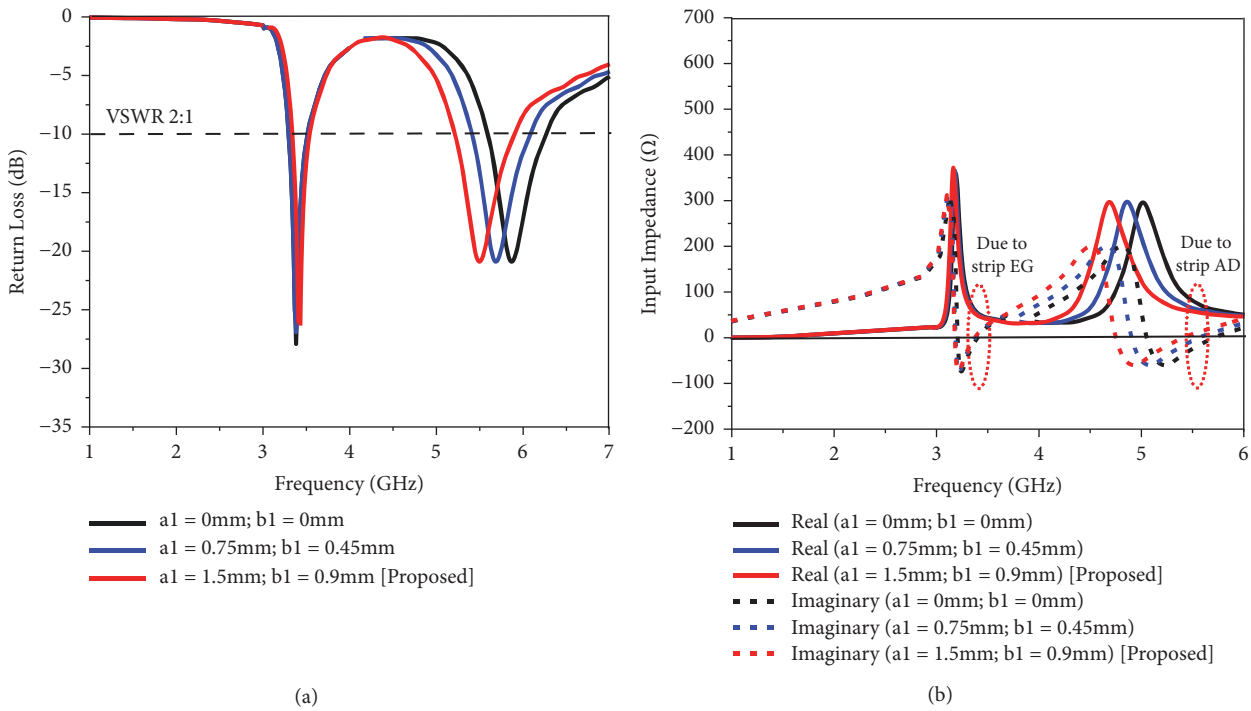

Figure 3: Simulated return loss and input impedance (Ω) of the proposed antenna as a function of tuning stub m (a_1xb_1).

reactance is equal to zero at the desired resonant mode of 5.5 GHz as shown in Figure 3(b). This condition leads to impedance matching and successful generation of f_u band with the desired bandwidth. Hence, the optimized size of "m" is 1.5x0.9mm^2.

4.2. Effects of Rectangular Tuning Stub "n" (a_2xb_2) on the Proposed Antenna. The effects of rectangular tuning stub "n" of length (a_2) and height (b_2) on the return loss and input impedance of the proposed antenna across f_m band are studied in Figure 4. As the value of a_2 is increased from 0 mm to 1.8mm and b_2 increased from 0 mm to 0.9mm, the f_m band shifts from the resonant mode of 3.85GHz towards a resonant mode of 3.35 GHz of f_m band, as shown in Figure 4(a). Also, as seen in Figure 4(b), for a_2=1.8mm and b_2=0.9mm, the input resistance is equal to 50Ω and capacitive reactance is equal to zero at the desired resonance of 3.35GHz. This leads to impedance matching between the antenna and coaxial feed and generation of the desired f_m band. From Figure 4, it is also seen that f_l and f_u bands remain unaffected. Therefore, the optimized size of "n" is 1.8x0.9mm^2

4.3. Effects of Varying L_x on the Proposed Antenna. The effects of varying L_x from 0 mm to 70 mm (in the step increments of 35 mm) for mounting the proposed antenna on the system ground over f_l, f_m, and f_u bands are analyzed in Figure 5. It is clearly seen that, at L_x=0mm, the resonant mode 2.4 of f_l shifts towards higher frequency with reduced bandwidth because of degradation in impedance matching, while the resonant mode 3.35GHz of f_m and 5.5 GHz of f_u bands have negligible effect. At L_x=35mm, all the desired bands of the proposed antenna are obtained with the required bandwidth and VSWR less than 2. Hence, from the above study, the optimum value of L_x =35mm is selected for mounting the proposed antenna on the system ground.

From the above parametric studies, the selected values for a_1xb_1, a_2xb_2, and L_x are 1.5x0.9mm^2, 1.8x0.9mm^2, and 35 mm, respectively. The other optimized values of the proposed antenna are given in Table 1.

The simulated return loss of the proposed antenna is as shown in Figure 6.

5. Two Antenna MIMO System Using Proposed WLAN/WiMAX Monopole Antenna

Possible antenna arrays formed by using proposed WLAN/WiMAX monopole antenna are studied in this section and shown in Figure 7. In first antenna array (case I) two antennas, namely, Antenna 1 and Antenna 2, are mounted on the top edge of the same system ground, at a distance of 155 mm from each other. Antenna 1 is the proposed antenna as shown in Figure 2 and Antenna 2 is an exact replica of Antenna 1. The simulated S parameters S_{11}, S_{21}, and S_{22} of case I are shown in Figure 8. In this case, the same effect on bandwidth is observed for both S_{11} and S_{22} but the return loss of f_l and f_u is higher at S_{11} whereas the return loss of f_m is higher at S_{22}. The resonant mode 2.4 GHz of f_l shifts at the frequency of 2.37GHz due to the larger inductive reactance produced by coaxial feeds at Antenna 1 and Antenna 2 and current path length of (0.2λ) towards strip FI. Hence, the 2.4GHz (2.4-2.48GHz) band is not covered. The bandwidth of f_m band remain unaffected and is the same as that of Antenna 1

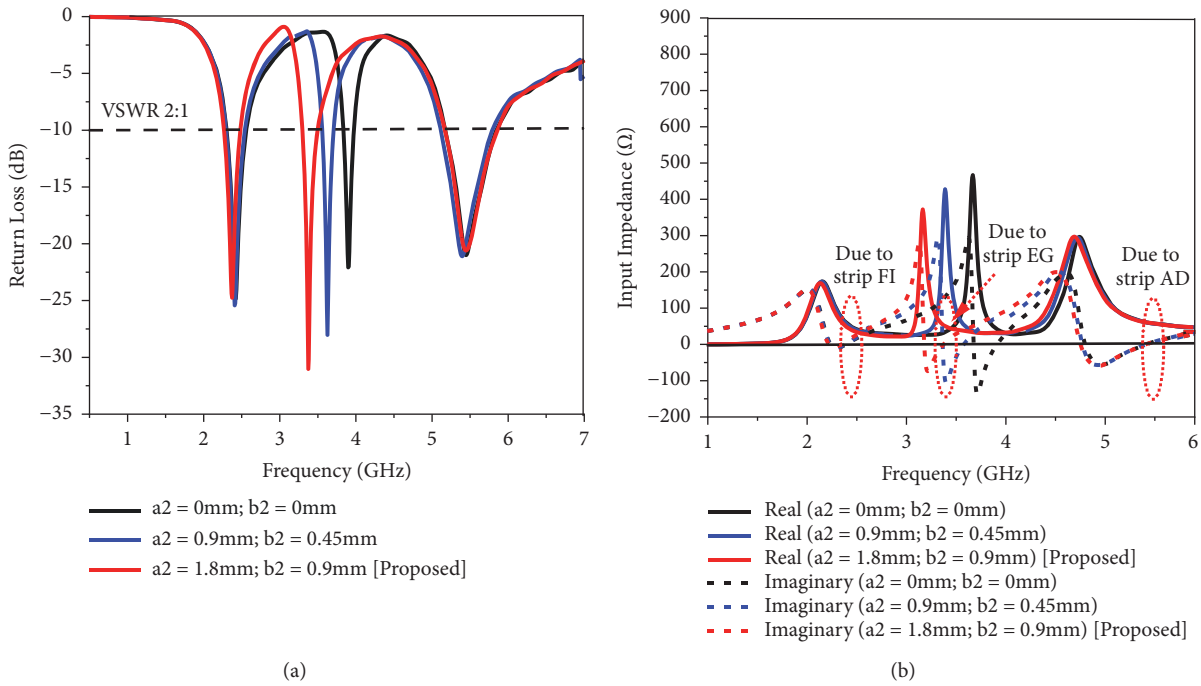

(a) (b)

Figure 4: Simulated return loss and input impedance (Ω) of the proposed antenna as a function of tuning stub n ($a_2 \times b_2$).

Table 1: Optimized values of the proposed antenna.

Parameter	Value (mm)	Parameter	Value (mm)	Parameter	Value (mm)
L	21	g_2	0.2	W_3	1.8
L_1	15	g_3	1.0	W_4	1.0
L_2	15	W	8		
L_3	19	W_1	1.1		
g_1	1.0	W_2	1.2		

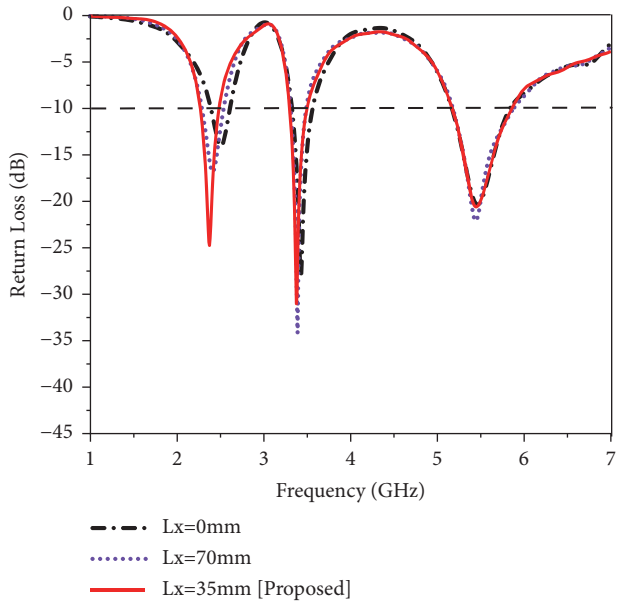

Figure 5: Simulated return loss of proposed antenna as a function of L_x for mounting the proposed antenna on the system ground.

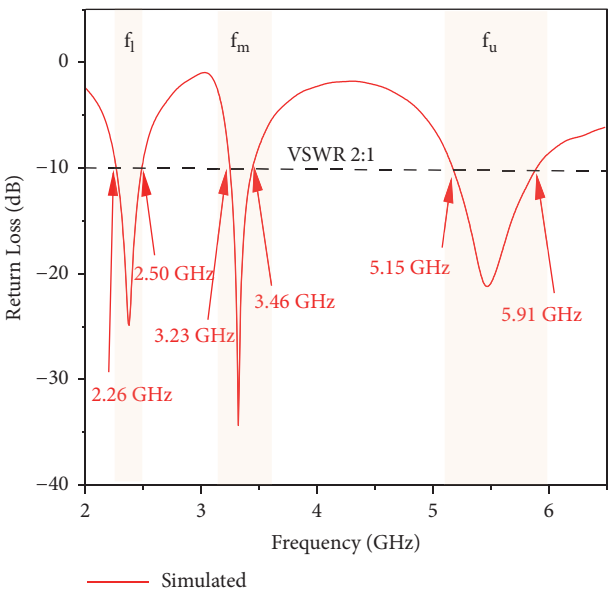

Figure 6: Simulated return loss of proposed antenna mounted on the system ground (supporting 13″ laptop display screen).

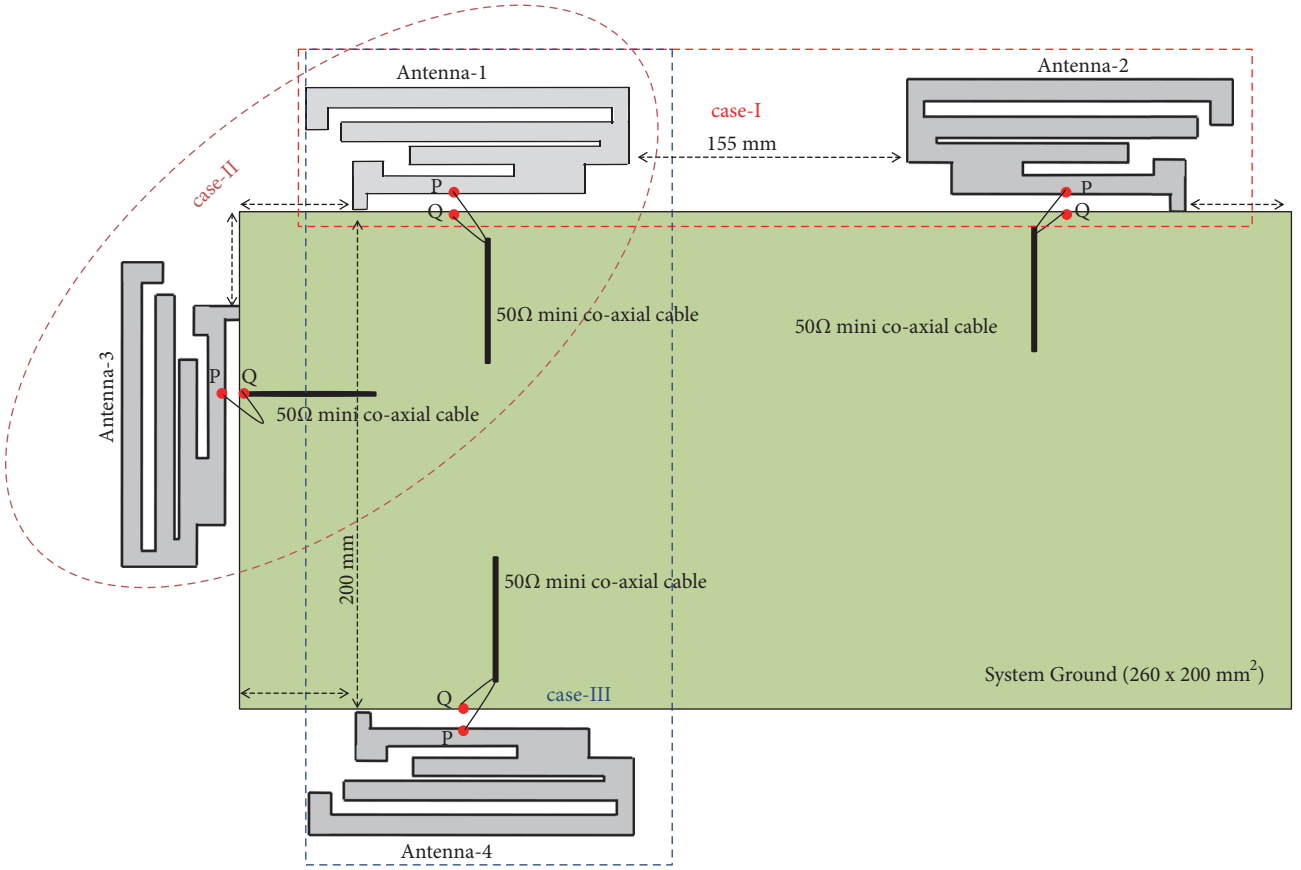

FIGURE 7: Possible Antenna Array cases for MIMO Applications mounted on the system ground.

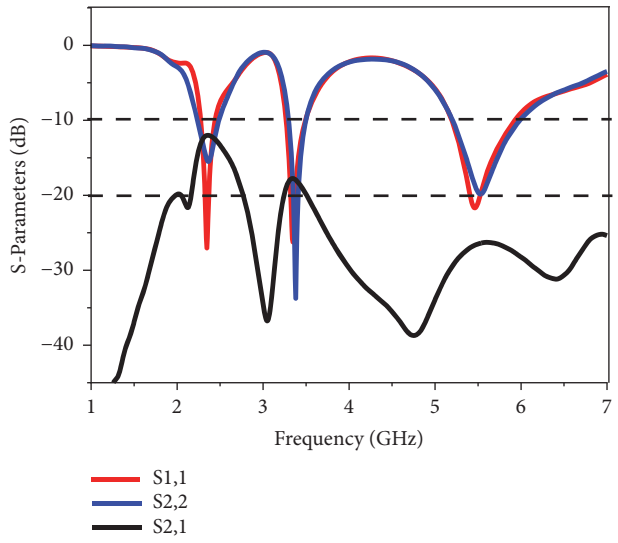

FIGURE 8: Simulated S parameters for MIMO antenna array of (case I).

(see Figure 6) because of perfect impedance matching between antennas and coaxial feeds. The resonant mode 5.5 GHz of f_u shifts towards a higher frequency of 5.9GHz and thereby, affect the 5.2GHz WLAN band. Also, as required the S_{21} is not better than -20dB for f_l and f_m bands. Hence, this case is not considered.

The second possible antenna array (case II) as shown in Figure 7, is further studied. In this case, Antenna 1 and Antenna 3 are placed adjacent to each other at a distance of 35 mm from the top left corner of the system ground. Antenna 3 is an exact replica of Antenna 1 and is rotated anticlockwise by 90° before placing it on the vertical left

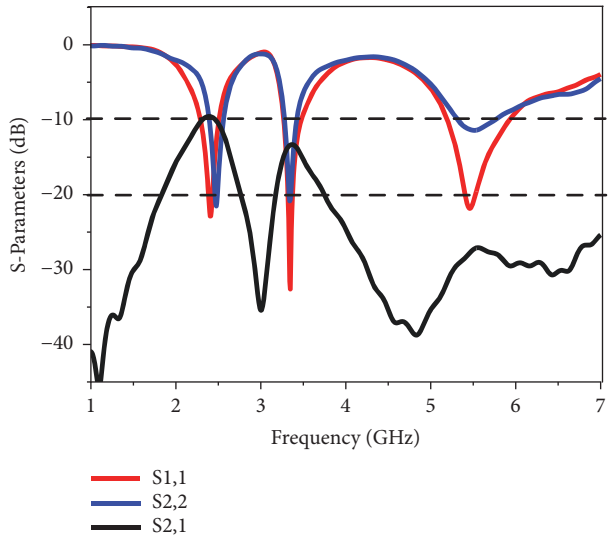

Figure 9: Simulated S parameters for the antenna array of case II.

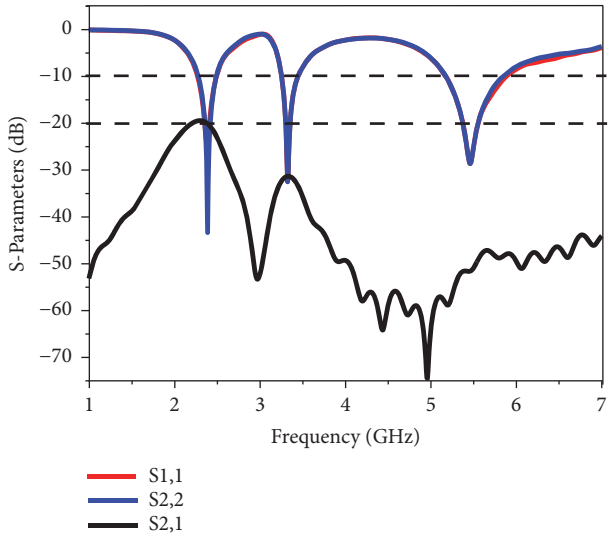

Figure 10: Simulated S parameters for the proposed MIMO antenna array of case III.

edge of the system ground. The simulated parameters are shown in Figure 9. It is seen that, there is a great mismatch between S_{11} and S_{22}. From S_{22} of Antenna 3, it is seen that the impedance bandwidth of f_l and f_u bands get reduced and does not conform the required bandwidth. Even though, the f_m band remains unaffected in both S_{11} and S_{22}, S_{21} is approximately -13dB which is not practically acceptable for high RF performance of MIMO system. Therefore, this array (case II) is not attractive for forming MIMO system in the laptop computer.

Another possible array (case III) was formed, by using Antenna 1 and Antenna 4 as analyzed in Figure 7. In this case, Antenna 4 is same as that of Antenna 1 and is rotated 180° along the x-axis. It is then placed at the bottom edge of the system ground at a distance of 200 mm from Antenna 1. Figure 10 shows the simulated S parameters of case III. Here, it is observed that the bandwidth of both S_{11} and S_{22} is same as that of Figure 6 along with good return loss across f_l, f_m and f_u bands. Also, isolation between antennas or S_{21} is achieved as -20dB, -30 dB, and -47dB across f_l, f_m, and f_u bands, respectively, because the system ground itself is acting as an isolating element between Antenna 1 and Antenna 4. The obtained isolation values are practically good for the optimal performance of the MIMO system. Hence, from the simulated results observed in Figure 10, case III was a good candidate for MIMO and was immediately taken for fabrication, the results of which are discussed further in Section 6.

6. Results and Discussion

To validate the simulated results of case III, the prototype of the proposed antenna array is fabricated as shown in Figure 11 and was tested using ROHDE and SCHWARZ (9

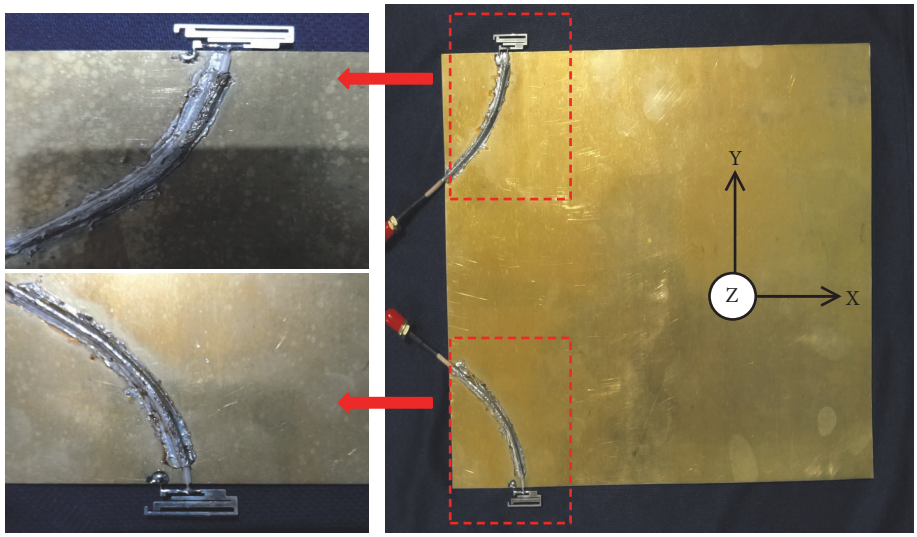

Figure 11: Fabricated photo of proposed MIMO antenna for laptop computers.

KHz-16GHz) network analyzer. The radiation performance, including radiation patterns, gain, and radiation efficiency of proposed case III, was tested in an anechoic chamber of size $8 \times 4 \times 4\text{m}^3$.

All the parameters were measured under the condition that, while measuring Antenna 1, the Antenna 4 was terminated with 50Ω load and vice versa.

6.1. Return Loss. Figure 12 shows the comparison of simulated and measured S parameters of the proposed MIMO antenna array and presents only S_{11} and S_{21} due to the analogy with S_{22} and S_{12}, respectively. The simulated -10dB impedance bandwidth of Antenna 1 and Antenna 4 is 10.08% (2.26-2.50GHz), 6.87% (3.23-3.46GHz), and 13.74% (5.15-5.91GHz), whereas the measured values are 11.86% (2.22-2.50GHz), 5.09% (3.25-3.42), and 16.84% (5.00-5.92GHz) in f_l, f_m, and f_u, respectively. The simulated and measured isolation or S_{21} between Antenna 1 and Antenna 4 are better than -20dB accross all the three desired bands as shown in Figure 12.

6.2. Measured Radiation Pattern. The normalized radiation patterns of proposed case III are shown in Figure 13. Here, the E-plane (copolarization) and H-plane (cross-polarization) in the x-y plane of the proposed MIMO antenna array are shown at the measured resonant mode of 2.42, 3.37, and 5.5 GHz of f_l, f_m, and f_u, respectively. The E-plane pattern in both antennas, namely, Antenna 1 and Antenna 4, at all resonant modes is nearly omnidirectional, whereas H-plane contributes dipole pattern forming bidirectional radiation without having any nulls. This confirms the applicability of antenna array for MIMO applications in the laptop computer.

6.3. Simulated and Measured Gain and Radiation Efficiency. Figure 14 shows simulated and measured gain and efficiency of the proposed antenna array (case III). Figure 14 presents efficiency of only Antenna 1 due to the analogy with Antenna 4. The values of simulated and measured gain and efficiency

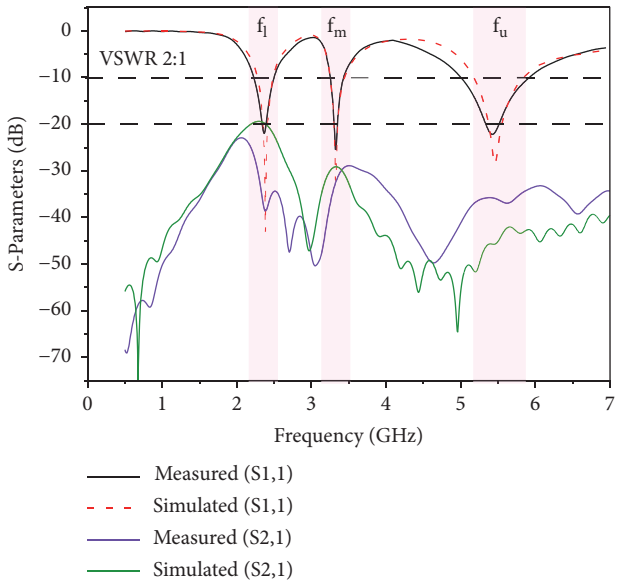

Figure 12: Simulated and Measured S parameters of proposed MIMO antenna.

are as shown in Table 2. A small deviation in simulated and measured values of gain and efficiency is observed which may be due to fabrication tolerances.

6.4. Envelope Correlation Coefficient (ECC). In a MIMO system, envelope correlation coefficient (ECC) is a very important parameter to evaluate channel capacity and cross-correlation performances between two antennas. It can be calculated using the following formula [4]:

$$\text{ECC} = \frac{\left|S_{11}^{*}S_{12} + S_{21}^{*}S_{22}\right|^2}{\left(1 - \left|S_{11}\right|^2 - \left|S_{21}\right|^2\right)\left(1 - \left|S_{22}\right|^2 - \left|S_{12}\right|^2\right)} \quad (1)$$

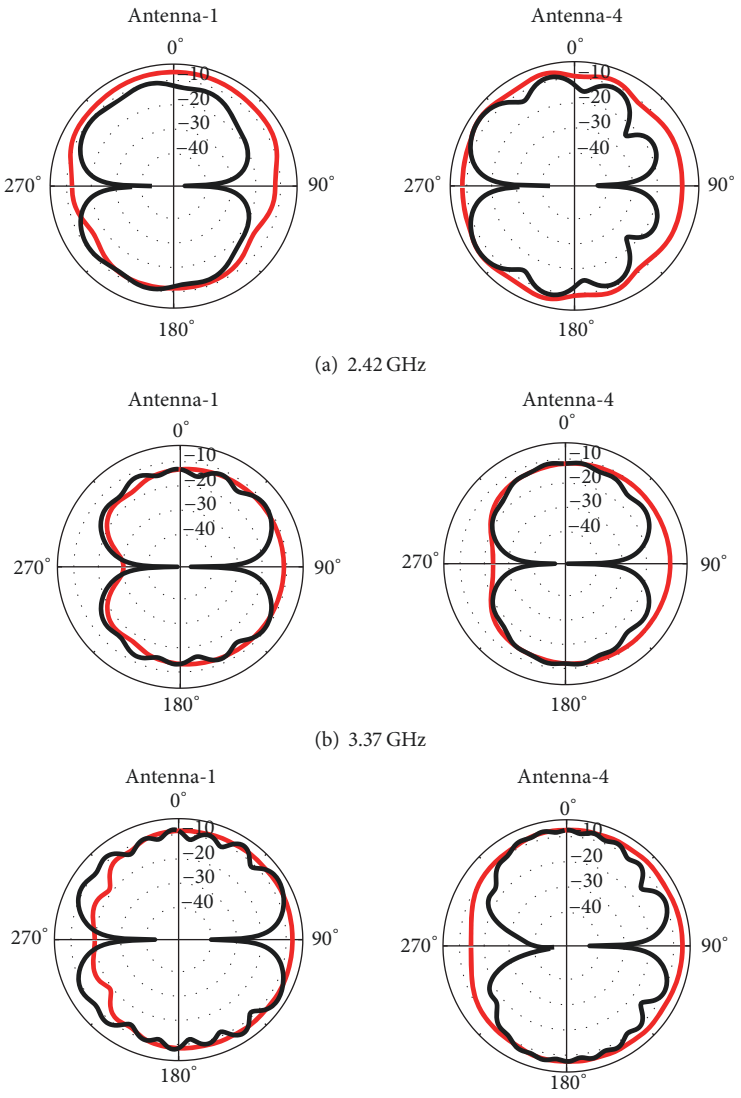

(a) 2.42 GHz

(b) 3.37 GHz

(c) 5.5 GHz

Figure 13: Measured radiation pattern of the proposed MIMO antenna.

Table 2: Comparison of simulated and measured values of gain and efficiency of the proposed antenna array (case III).

Covered bands (GHz)	Gain (dBi)		Efficiency (%)	
	Simulated	Measured	Simulated	Measured
f_l	4.61-5.25	4.42-4.90	82.24-87.86	78.5-83.9
f_m	5.82-5.95	5.52-5.70	78.69-86.88	75.43-81.0
f_u	3.92-5.14	3.64-4.87	79.59-87.58	76.15-81.5

where $*$ indicates the complex conjugate. Figure 15 shows the simulated and measured ECC using S parameters. The implemented MIMO antenna shows the optimal performance as both the simulated and measured ECC values are less than 0.004 across all the desired bands, that too without using any additional isolation techniques between the two antennas.

7. Conclusions

The triple band WLAN/WiMAX monopole antenna design for MIMO applications in the laptop computer is verified successfully. The proposed antenna has a very small size of 21 $\times$ 8mm^2, simple structure, easy to fabricate, and operates in 2.4/5.2/5.8 GHz WLAN and 2.3/3.3/5.5 GHz WiMAX bands. Additionally, owing to RF performance, small size, and simple structure of the proposed antenna, an antenna array formed by using the same antenna for MIMO system shows that, it has excellent gain and efficiency well above 3.65 dBi and 75%, respectively, isolation between two antennas is better than -20dB and ECC is below 0.004 over the three bands of interest. Hence, the proposed antenna and the

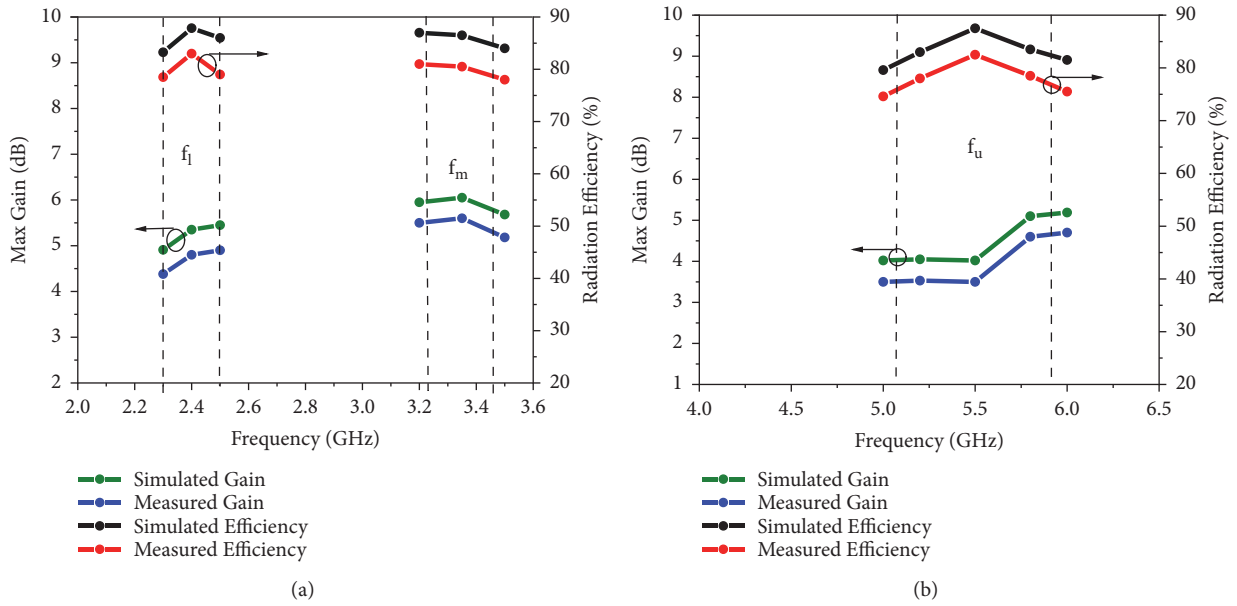

Figure 14: Simulated and measured gain and efficiency of proposed MIMO antenna.

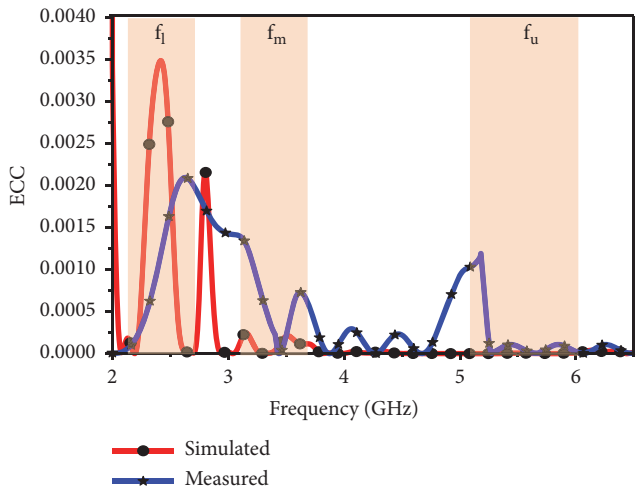

Figure 15: Simulated and measured ECC for proposed MIMO antenna.

antenna array formed are promising and good candidate for MIMO applications in the laptop computer.

Data Availability

The data used to support the findings of this study are included within the article.

Conflicts of Interest

The authors declare that there are no conflicts of interest regarding the publication of this paper.

Acknowledgments

The authors would like to thank the support rendered by the Technical Education Quality Improvement Program (TEQIP) and TIFAC-CORE in Wireless Technology, Thiagarajar College of Engineering, Madurai.

References

[1] K.-L. Wong, P. W. Lin, and T.-J Wu, "On the isolation of two LTE700/2300/2500 antennas in the laptop computer," *Microwave and Optical Technology Letters*, vol. 55, no. 6, pp. 1370–1375, 2013.

[2] K.-L. Wong, H.-J. Jiang, and Y.-C. Kao, "High-isolation 2.4/5.2/5.8 GHz WLAN MIMO antenna array for laptop computer application," *Microwave and Optical Technology Letters*, vol. 55, no. 2, pp. 382–387, 2013.

[3] K.-L. Wong, H.-J. Jiang, and T.-W. Weng, "Small-size planar LTE/WWAN antenna and antenna array formed by the same for tablet computer application," *Microwave and Optical Technology Letters*, vol. 55, no. 8, pp. 1928–1934, 2013.

[4] H.-L. Su, B.-W. Huang, H.-R. Liang et al., "Uniplanar multiband MIMO antennas for laptop computer applications," in *Proceedings of the 2017 IEEE International Conference on Antenna Innovations & Modern Technologies for Ground, Aircraft and Satellite Applications (iAIM)*, pp. 1–4, Bangalore, India, November 2017.

[5] Y. Liu, Y. Wang, and Z. Du, "A broadband dual-antenna system operating at the WLAN/WiMax bands for laptop computers," *IEEE Antennas and Wireless Propagation Letters*, vol. 14, pp. 1060–1063, 2015.

[6] L. Guo, Y. Wang, Z. Du, Y. Gao, and D. Shi, "A Compact uniplanar printed dual-antenna operating at the 2.4/5.2/5.8 GHz WLAN bands for laptop computers," *IEEE Antennas and Wireless Propagation Letters*, vol. 13, pp. 229–232, 2014.

[7] S.-C. Chen, J.-Y. Sze, and K.-J. Chuang, "Isolation enhancement of small-size WLAN MIMO antenna array for laptop computer

application," *Journal of Electromagnetic Waves and Applications*, vol. 31, no. 3, pp. 323–334, 2017.

[8] S.-W. Su, C.-T. Lee, and S.-C. Chen, "Very-low-profile, triband, two-antenna system for wlan notebook computers," *IEEE Antennas and Wireless Propagation Letters*, vol. 17, no. 9, pp. 1626–1629, 2018.

[9] N. Ojaroudi, N. Ghadimi, M. Mehranpour, Y. Ojaroudi, and S. Ojaroudi, "A new design of triple-band WLAN/WiMAX monopole antenna for multiple-input/multiple-output applications," *Microwave and Optical Technology Letters*, vol. 56, no. 11, pp. 2667–2671, 2014.

[10] A. M. Soliman, D. M. Elsheakh, E. A. Abdallah, and H. El-Hennawy, "Design of planar inverted-F antenna over uniplanar EBG structure for laptop mimo applications," *Microwave and Optical Technology Letters*, vol. 57, no. 2, pp. 277–285, 2015.

[11] G. Kumar and K. P. Ray, *Broadband Microstrip Antenna*, Artech House, Inc, 2003.